

INTERPRETAÇÕES QUALITATIVA E QUANTITATIVA DE DADOS  
MAGNÉTICOS

Felipe Ferreira de Melo

Tese apresentada ao Programa de Pós-graduação em Geofísica do Observatório Nacional, como parte dos requisitos necessários à obtenção do título de Doutor em Geofísica.

Orientador(a): Dra. Valéria Cristina Ferreira  
Barbosa

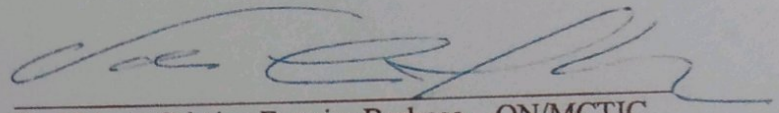
Rio de Janeiro  
Fevereiro de 2020

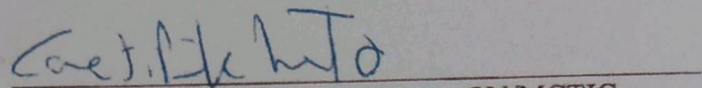
"INTERPRETAÇÕES QUALITATIVA E QUANTITATIVA DE DADOS  
MAGNÉTICOS"

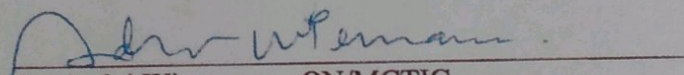
FELIPE FERREIRA DE MELO

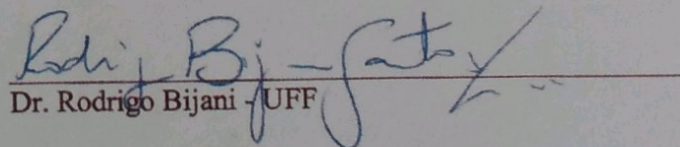
TESE SUBMETIDA AO CORPO DOCENTE DO PROGRAMA DE PÓS-  
GRADUAÇÃO EM GEOFÍSICA DO OBSERVATÓRIO NACIONAL COMO PARTE  
DOS REQUISITOS NECESSÁRIOS PARA A OBTENÇÃO DO GRAU DE  
DOUTOR EM GEOFÍSICA.

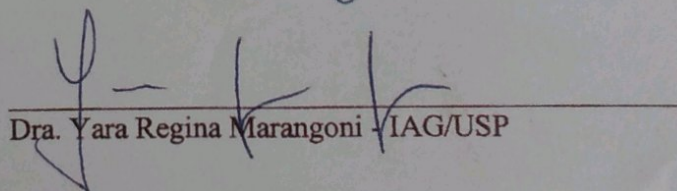
Aprovada por:

  
Dr. Valeria Cristina Ferreira Barbosa – ON/MCTIC  
(Orientadora)

  
Dr. Cosme Ferreira da Ponte Neto – ON/MCTIC

  
Dr. André Wiermann – ON/MCTIC

  
Dr. Rodrigo Bijani – UFF

  
Dra. Yara Regina Marangoni – IAG/USP

RIO DE JANEIRO – BRASIL

24 DE JANEIRO DE 2020

Ferreira de Melo, Felipe

Interpretações qualitativa e quantitativa de dados magnéticos/Felipe Ferreira de Melo. – Rio de Janeiro: ON, 2020.

??, 97 p. 29, 7cm.

Orientador(a): Valéria Cristina Ferreira Barbosa

Tese (doutorado) – ON/Programa de Pós-graduação em Geofísica, 2020.

Referências Bibliográficas: p. 76 – 88.

1. Interpretação de dados magnéticos. 2. Deconvolução de Euler. 3. Amplitude do vetor magnético anômalo. 4. Camada equivalente. I. , . II. Observatório Nacional, Programa de Pós-graduação em Geofísica. III. Título.

*"Oh, oh, oh, oh, oh, sometimes I  
get a good feeling, yeah I get a  
feeling that I never never never  
never had before, no no I get a  
good feeling, yeah"*

*Good Feeling - Flo Rida*

# Agradecimentos

Antes e ao longo desse doutorado inúmeras pessoas e instituições com quem me relacionei contribuíram para o meu desenvolvimento profissional e pessoal, por isso, sinceramente gostaria de agradecer à todos. Especialmente, gostaria de agradecer:

À minha orientadora Valéria Cristina Ferreira Barbosa por todas as possibilidades que me permitiram experienciar e desenvolver a vida de pesquisador em todas as suas etapas.

À minha companheira e parceira Vivian Pires que me apoiou e incentivou de incontáveis maneiras.

À Yolanda G. Teja e Shayane P. Gonzalez pela colaboração no desenvolvimento de trabalhos que contribuíram para o meu conhecimento.

À Rodrigo Canário pela motivação contínua em deconvolução de Euler.

Aos colegas do Observatório Nacional, alunos e funcionários, e ao grupo PINGA.

Ao Observatório Nacional pela estrutura e suporte financeiro.

À CAPES, FAPERJ (grant E-26/200.532/2018) e SEG/Lucien LaCoste pelas bolsas de estudos.

Aos membros da banca por suas contribuições e discussões.

À Companhia de Pesquisa de Recursos Minerais (CPRM) pela permissão para utilizar os dados reais apresentados nessa tese.

E aos meus pais, Vera e Clovis, e à minha irmã Fabiana.

Resumo da Tese apresentada ao Programa de Pós-Graduação em Geofísica do Observatório Nacional como parte dos requisitos necessários para a obtenção do título de Doutor em Geofísica.

## INTERPRETAÇÕES QUALITATIVA E QUANTITATIVA DE DADOS MAGNÉTICOS

Felipe Ferreira de Melo

Fevereiro/2020

Apresentamos uma nova abordagem metodológica para realizar a interpretação qualitativa e duas melhorias metodológicas para realizar interpretações quantitativas de dados magnéticos. Na primeira parte desta tese, propomos o uso da amplitude do vetor da anomalia magnética para interpretar qualitativamente dados magnéticos em baixas latitudes magnéticas, em grandes áreas. Os dados de amplitude são fracamente dependentes da direção da magnetização, não requerem conhecimento prévio da direção da magnetização da fonte e produzem máximos sobre as fontes causadoras. Assim, os dados de amplitude permitem a definição das posições horizontais, das projeções horizontais das fontes e aproximadamente de suas extensões, principalmente em baixas latitudes magnéticas, em que o campo magnético aumenta a complexidade das anomalias, além do caso de anomalias com magnetização remanente. Calculamos os dados de amplitude a partir da anomalia de campo total por meio da técnica da camada equivalente e mostramos o desempenho desses dados na interpretação qualitativa com testes sintéticos. Na aplicação a dados reais no Cráton da Amazônia, norte do Brasil, os dados de amplitude localizam anomalias destacadas na anomalia de campo total, que têm correlação com afloramentos identificados no mapa geológico. Além disso, os dados de amplitude sugerem a presença de múltiplos corpos geológicos em subsuperfície seguindo um alinhamento das unidades geológicas aflorantes. Para as interpretações quantitativas, propomos duas melhorias metodológicas na deconvolução de Euler. Assim, na segunda parte da tese, lidamos com o espalhamento de soluções na deconvolução de Euler, selecionando estimativas confiáveis da deconvolução de Euler através das derivadas verticais da anomalia de campo total. A derivada vertical é utilizada por causa de sua habilidade em localizar fontes já que o sinal decai rapidamente com o afastamento da fonte. Para cada janela móvel de dados, calculamos o desvio padrão da derivada vertical

da anomalia de campo total e definimos as estimativas confiáveis de localização da fonte como aquelas estimativas obtidas pelas janelas móveis com os maiores desvios padrão. O índice estrutural correto é definido com o maior agrupamento das estimativas confiáveis e a média dessas estimativas define a posição da fonte. Nossa metodologia foi testada em cenários de múltiplas fontes e anomalias interferentes, definindo com sucesso o índice estrutural correto e as profundidades das fontes. A aplicação na anomalia magnética de Anitápolis, sul do Brasil, permitiu inferir a presença de um plug intrusivo e sua profundidade até o topo. Finalmente, na terceira parte desta tese, propomos a definição do índice estrutural correto na deconvolução de Euler através de estimativas do nível de base. Mostramos matematicamente que assumindo o índice estrutural correto sobre a fonte, em uma região definida por patamares de estimativas horizontais ou verticais constantes, o desvio padrão das estimativas do nível de base é mínimo. Portanto, propusemos um novo critério para determinar o índice estrutural correto por meio do desvio padrão mínimo das estimativas de nível de base. Testes em dados sintéticos mostram que a metodologia de estimativas do nível dos base em plots de patamar supera as estimativas de profundidade na definição do índice estrutural correto em cenários com anomalias fortemente interferentes. Aplicamos a metodologia em dados magnéticos de parte da província alcalina de Goiás, centro do Brasil, e os resultados sugerem que três plugs intrusivos dão origem à anomalia de Diorama e fontes tipo dipolo produzem as anomalias de Arenópolis e Montes Claros de Goiás.

Abstract of the Thesis presented to the National Observatory's Graduate Program in Geophysics as a partial fulfillment of the requirements for the degree of Doctor in Geophysics.

## QUALITATIVE AND QUANTITATIVE INTERPRETATIONS OF MAGNETIC DATA

Felipe Ferreira de Melo

February/2020

We present a new methodological approach to accomplish a qualitative interpretation and two methodological improvements to accomplish quantitative interpretations of magnetic data. In the first part of this thesis, we propose the use of the amplitude of the magnetic anomaly vector for interpreting qualitatively magnetic data at low magnetic latitudes, in large areas. The amplitude data is weakly dependent on the magnetization direction, require no prior knowledge of the source magnetization direction and produce maxima over the causative sources. Thus, the amplitude data allow the definition of the horizontal positions, the horizontal projections of the sources and roughly their extensions, especially at low magnetic latitudes, where the magnetic field increases the complexity of the anomalies, and for anomalies with strong remanent magnetization. We compute the amplitude data from the total-field anomaly via the equivalent source technique and show the performance of these data in qualitative interpretation with synthetic tests. In the application to real data on the Amazonian Craton, northern Brazil, the amplitude data located anomalies highlighted on the total-field anomaly, which have correlation to mapped outcrops on the geologic map. Moreover, the amplitude data suggest the presence of multiple buried geologic bodies following a trend of the known outcropping geologic units. For quantitative interpretations we propose two methodological improvements on Euler deconvolution. Thereby, in the second part of the thesis we deal with the spray of solutions on Euler deconvolution selecting reliable Euler deconvolution estimates throughout the vertical derivatives of the total-field anomaly. The vertical derivative is selected because they of its ability to locate sources due to its higher signal decay with distance. For each moving-data window, we compute the standard deviation of the vertical derivative of the total-field anomaly and define the reliable source-location estimates as those estimates obtained by the data windows with the largest standard deviations. The correct structural index is defined

with the tightest cluster of the reliable estimates and the mean of these estimates define the source position. Our methodology was tested in scenarios of multiple sources and interfering anomalies, successfully defining the correct structural index and the depths of the sources. Application to the Anitápolis magnetic anomaly, southern Brazil, allows inferring the presence of a plug intrusion and its depth to the top. Finally, in the third part of this thesis we propose the definition of the correct structural index in Euler deconvolution via base-level estimates. We mathematically show that assuming the correct structural index over the source, on a region defined by plateaus of constant horizontal or vertical estimates, the standard deviation of base-level estimates are minimum. Therefore, we have proposed a new criterion for determining the correct structural index by means of the minimum standard deviation of base-level estimates. Tests on synthetic data show that the methodology of base-level estimates on plateau plots overcomes depth estimates in defining the correct structural index in scenarios with strongly interfering anomalies. We applied the methodology on magnetic data from part of Goiás Alkaline Province, central Brazil, and the results suggest that three plug intrusions give rise to the Diorama anomaly and dipole-like sources yield Arenópolis and Montes Claros de Goiás anomalies.

# Contents

<b>1</b>	<b>Introduction</b>	<b>1</b>
<b>2</b>	<b>Amplitude of the magnetic anomaly vector in the interpretation of total-field anomaly data at low magnetic latitudes</b>	<b>6</b>
2.1	Summary . . . . .	6
2.2	Introduction . . . . .	7
2.3	Methodology . . . . .	9
2.3.1	Total gradient . . . . .	9
2.3.2	Amplitude of the magnetic anomaly vector . . . . .	10
2.4	Synthetic tests . . . . .	12
2.4.1	Test 1 – Simulated field at high latitude and induced magnetization . . . . .	13
2.4.2	Test 2 – Simulated field at mid-latitude and remanent magnetization . . . . .	15
2.4.3	Test 3 – Simulated field at low latitude and remanent magnetization . . . . .	16
2.5	Application to real data set . . . . .	18
2.6	Final Considerations . . . . .	22
<b>3</b>	<b>Reliable Euler deconvolution estimates throughout the vertical derivatives of the total-field anomaly</b>	<b>24</b>
3.1	Summary . . . . .	24
3.2	Introduction . . . . .	25
3.3	Methodology . . . . .	26
3.4	Synthetic tests . . . . .	28
3.4.1	Test 1 - Distinct SIs and strong nonlinear magnetic base level . . . . .	28
3.4.2	Test 2 - Nearby sources with remanence . . . . .	31
3.4.3	Test 3 - Reliable estimates via other quantities? . . . . .	34
3.5	Application to real data set . . . . .	39
3.6	Final Considerations . . . . .	42

<b>4</b>	<b>Correct structural index in Euler deconvolution via base-level estimates</b>	<b>43</b>
4.1	Summary . . . . .	43
4.2	Introduction . . . . .	44
4.3	Methodology . . . . .	46
4.4	Synthetic tests . . . . .	49
4.4.1	Test 1 - Null background . . . . .	50
4.4.2	Test 2 - Constant background . . . . .	52
4.4.3	Test 3 - Nonlinear background . . . . .	56
4.4.4	Test 4 - Strongly interfering anomalies with constant and non-linear background . . . . .	62
4.5	Application to real data set . . . . .	67
4.6	Final Considerations . . . . .	73
<b>5</b>	<b>Conclusions</b>	<b>74</b>
	<b>Bibliography</b>	<b>76</b>
	<b>Appendices</b>	<b>89</b>
<b>A:</b>	<b>Theory of Euler deconvolution</b>	<b>90</b>
A.1	Euler's theorem for homogeneous functions . . . . .	90
A.2	Euler's theorem applied to single-point sources . . . . .	91
A.3	Euler deconvolution . . . . .	92
A.4	Plot of the solutions . . . . .	94
A.5	Traditional definition of the correct SI . . . . .	96

# List of Figures

2.1	Simulated sources . . . . .	13
2.2	Test 1 - high latitude . . . . .	14
2.3	Test 2 - mid latitude . . . . .	16
2.4	Test 3 - low latitude . . . . .	18
2.5	Real data application . . . . .	20
2.6	Real data fitting . . . . .	21
2.7	Real data interpretation . . . . .	22
3.1	Test 1 - Simulated sources and the simulated total-field anomaly . . .	30
3.2	Test 1 - Euler deconvolution unfiltered estimates . . . . .	31
3.3	Test 1 - Euler deconvolution source-position estimates . . . . .	32
3.4	Test 1 - Euler deconvolution base-level estimates . . . . .	33
3.5	Test 2 - Euler deconvolution estimates . . . . .	34
3.6	Test 3 - Derivatives of the total-field anomaly . . . . .	35
3.7	Test 3 - Euler deconvolution source-position estimates - $\partial h/\partial x$ . . . . .	36
3.8	Test 3 - Euler deconvolution source-position estimates - $\partial h/\partial x$ . . . . .	37
3.9	Test 3 - Euler deconvolution estimates from total-field anomaly with a moving-data window of $5 \times 5$ . . . . .	38
3.10	Test 3 - Euler deconvolution estimates from total-field anomaly with a moving-data window of $3 \times 3$ . . . . .	39
3.11	Real data application - Euler deconvolution estimates . . . . .	41
4.1	Flow chart of the methodology to define the correct SI . . . . .	48
4.2	Test 1 - total-field anomaly . . . . .	50
4.3	Test 1 - $\hat{z}_o$ and $\hat{b}$ from Euler deconvolution . . . . .	51
4.4	Test 2 - Total-field anomaly . . . . .	52
4.5	Test 2 - $\hat{z}_o$ and $\hat{b}$ from Euler deconvolution . . . . .	54
4.6	Test 3 - Total-field anomaly . . . . .	57
4.7	Test 3 - $\hat{z}_o$ and $\hat{b}$ from Euler deconvolution . . . . .	59
4.8	Test 3 - $\hat{x}_o$ and $\hat{y}_o$ from Euler deconvolution . . . . .	60
4.9	Test 4 - Total-field anomaly . . . . .	62

4.10	Test 4 - $\hat{z}_o$ and $\hat{b}$ from Euler deconvolution . . . . .	63
4.11	Test 4 - $\hat{x}_o$ and $\hat{y}_o$ from Euler deconvolution . . . . .	65
4.12	Real data set application . . . . .	68
4.13	Real data set application - $\hat{x}_o$ and $\hat{y}_o$ . . . . .	70
4.14	Real data set application - $\hat{z}_o$ . . . . .	71
4.15	Real data set application - $\hat{b}$ . . . . .	72
A.1	Structural indices of magnetic single-point sources. . . . .	94
A.2	Classic plot of Euler estimates. . . . .	95
A.3	Plateau plot of Euler estimates. . . . .	97

# List of Tables

4.1	Test 1 - Standard deviations of $\hat{z}_o$ and $\hat{b}$ . . . . .	51
4.2	Test 2 - Standard deviation of $\hat{z}_o$ . . . . .	55
4.3	Test 2 - Standard deviation of $\hat{b}$ . . . . .	55
4.4	Test 3 - Standard deviation of $\hat{z}_o$ . . . . .	61
4.5	Test 3 - Standard deviation of $\hat{b}$ . . . . .	61
4.6	Test 4 - Standard deviation of $\hat{z}_o$ . . . . .	66
4.7	Test 4 - Standard deviation of $\hat{b}$ . . . . .	66
4.8	Real data set application - Standard deviation of $\hat{b}$ for the total-field anomaly . . . . .	71
4.9	Real data set application - Standard deviation of $\hat{b}$ for the total-field measurements . . . . .	72
A.1	Structural indices used in Euler deconvolution. . . . .	94

# Chapter 1

## Introduction

The magnetic method is the oldest and one of the most widely used geophysical exploration tool (Haldar, 2017), it has been used for exploration of iron ore deposits since the seventeenth century (Nabighian et al., 2005). During the World War II, the development of a fluxgate magnetometer for use in airborne submarine detection (Reford and Sumner, 1964) was a landmark in exploration geophysics. Since then, the magnetometers are employed in drill holes, mines, submarines, ships, ground surveys, observatories, aircraft, drones, balloons, space shuttles and satellites (Hinze et al., 2013). As a consequence, the magnetic method has a wide range of applications including from shallow subsurface exploration to crustal studies (Hinze et al., 2013). Some applications of the magnetic method in shallow subsurface explorations include geological studies in petroleum exploration (Busby et al., 1991; Curto et al., 2012; Donovan et al., 1984), in mineral exploration (Gunn and Dentith, 1997; Louro et al., 2014), geological mapping (Lourenço et al., 2014; Teskey et al., 1993) and identification of unexploded ordnance (Gamey, 2008; Salem et al., 2001). However, the magnetic method solely will not provide the complete and correct description of the subsurface (Hinze et al., 2013). Therefore, it is normally employed jointly with other geophysical methods, for example, the gravimetric (Marangoni et al., 2016; Tontini et al., 2016), the radiometric (Airo and Loukola-Ruskeeniemi, 2004; Gonçalves and Sampaio, 2013), the magnetotellurics (Gallardo et al., 2012) and the seismic reflection (Adriano et al., 2018; Filina, 2019) methods.

The purpose of the magnetic interpretation is to improve our understanding of the geology in subsurface (LaFehr and Nabighian, 2012). We can divide the magnetic interpretation into two phases: qualitative and quantitative. Initially, the interpretation phase is mainly qualitative and its objective is identifying and isolating the anomalies (Hinze et al., 2013), as well as their correlations with mapped rocks or geologic structures (Nabighian et al., 2005). In the second phase, the quantitative interpretation uses techniques such as, for example, the automated depth-estimation methods, to fast estimation of the depth to the top or to the center

of the source, and the inversion methods, to estimate the geometries of the geologic bodies or the physical-property distributions in the subsurface that can satisfy the observed data (Barbosa and Silva, 2011; Hinze et al., 2013). Both qualitative and quantitative interpretations are jointly used to elaborate geological conclusions from the estimated (or interpreted) models (Nabighian et al., 2005).

The qualitative magnetic interpretation identifies the magnetic anomaly patterns and, if available, correlates these patterns with the geological information. For reconnaissance and regional geological mapping surveys, the qualitative interpretation may be sufficient to allow the identification of the anomaly sources and the extrapolation of these geological informations into unknown areas (Hinze et al., 2013). The first qualitative interpretation is usually performed in the total-field anomaly, however the effects of the magnetization vectors of both the inducing field and the remanent magnetic field generate anomalies that demand some transformation to be understood, specially at low latitudes or when remanence is strong. Therefore, the early stages of magnetic data interpretation generally involve the application of mathematical filters to enhance or isolate anomalies of interest (Nabighian et al., 2005). Some techniques to aid in the qualitative interpretation are the following. The upward (or downward) continuation (Henderson and Zietz, 1949b) simulates the acquisition of the magnetic data at a height above (or below) the real acquisition of the data, attenuating (or enhancing) high frequency anomalies. The reduction to the pole (Baranov, 1957; Gunn, 1975) transforms magnetic anomalies observed at any latitude into the anomalies that would be produced at the pole (i.e., vertical magnetization). The first (Hood, 1965) and the second (Henderson and Zietz, 1949a) vertical derivatives enhance high frequencies and the horizontal derivatives (Glicken, 1955; Whitham, 1960) define the borders of the sources. The combination of the derivatives generated new interpretation methods, such as the 3D analytical signal (Roest et al., 1992), which is nowadays called total gradient (Nabighian et al., 2005), the tilt angle (Miller and Singh, 1994), the theta map (Wijns et al., 2005) and the monogenic signal (Hidalgo-Gato and Barbosa, 2015). Comprehensive reviews and comparisons of these and other methods, also known as edge detectors, can be found in Pilkington and Keating (2009), Li and Pilkington (2016) and Pilkington and Tschirhart (2017).

The quantitative magnetic interpretation extracts quantitative information from magnetica data produced by geological sources in subsurface, which were measured on (or above) the Earth's surface. Some of these information are the geometry of the geologic sources, the depths to the tops (or to the bottoms) of the geologic sources and the magnetization contrast distribution in the subsurface. However, due to inherent ambiguity of potential field methods, simultaneous determination of all these information is impossible without complementary geological or geophysical

information (Hinze et al., 2013). For example, via inversion techniques, Parker et al. (1987), Li and Oldenburg (1996), Portniaguine and Zhdanov (2002) and Barbosa and Silva (2006) estimated a physical-property distribution, given a fixed geometry. On the other hand, assuming a known physical-property contrast Zeyen and Pous (1991), Nunes et al. (2008) and Hidalgo-Gato and Barbosa (2019) estimated the source geometry. Some automated depth-estimation methods are the following. The Werner deconvolution (Hartman et al., 1971; Ku and Sharp, 1983; Werner, 1953) assumes that a thin sheet (thin dike or a contact) produces the observed total-field anomaly and estimates the dip, susceptibility and depth of the source. The Naudy method (Naudy, 1971) estimates the depth and the type of the sources with a moving-data window on a profile that cross correlates the observed profile of the total-field anomaly with theoretical anomalies. The Euler deconvolution (Thompson, 1982) is based on Euler homogeneous equation and was proposed to work on profile data, on a moving-data window scheme. The Euler deconvolution estimates the depth and type of the causative source, and was expanded to work on gridded data by Reid et al. (1990) becoming the most popular method for fast interpretation of potential field data. Comparisons of these and other automated depth-estimation methods on profile data can be found in Li (2003). The advantage of depth-estimation methods is that they are not affected by magnetization effects. The disadvantage of the depth-estimation methods is the assumption of sources with simple geometry. The inversion techniques are usually used to define the entirely source, but as pointed before, they need a prior information about the source and they are computationally cost. Usually, to provide an initial and fast quantitative description of the subsurface, the automated depth-estimation methods are used. Recently, the results from the automated depth-estimation methods can be used as input to retrieve detailed characterization of the source using inversion methods (Fregoso et al., 2015; Oliveira Jr et al., 2015; Paoletti et al., 2013).

In the first part of this thesis, we propose a new approach to perform a qualitative interpretation of magnetic data with focus on remanent magnetization, over large areas at low magnetic latitudes. In the second part of this thesis, we propose two new methodologies to perform quantitative interpretation of magnetic data with focus on Euler deconvolution, an automated depth-estimation method. All the development on this thesis was performed in python language and it follows the open source code. The codes are available in the repositories indicated in the methodology section of each chapter.

In Chapter 2 we present a new approach to perform magnetic interpretation over large areas at low magnetic latitudes. At these latitudes, the interpretation of the total-field anomalies and the definition of the sources' boundaries are not straightforward due to the magnetization direction of the incident field. The difficult in

the interpretation increases in scenarios where the sources have remanent magnetization. Therefore, we propose the use of the amplitude of the magnetic anomaly vector in the interpretation of the total-field anomaly at low magnetic latitudes, in large areas. The amplitude data are weakly dependent on the magnetization direction, hence the knowledge of the magnetization direction of the sources is not required to perform the transformation. These data are computed from the total-field anomaly using the equivalent layer principle and generate maxima over the sources, thus allowing to define the horizontal position and roughly the extension of the sources. We performed the interpretation of a large area of the Amazonian Craton, northern Brazil, with the amplitude data and correlated the results with a geologic map. The amplitude data highlight the position of the sources identified in the total-field anomaly and mapped as outcrops in the geologic map. These results may indicate new geologic bodies with clear alignment with the outcrops.

The second part of the thesis is focused on Euler deconvolution and is divided in two chapters. Chapter 3 describes a methodology to deal with the spray of solutions on Euler deconvolution estimates. The spray of solutions is an inherent problem in Euler deconvolution because the technique solves a system of equations on a moving-data window scheme and for each position of this window four parameters are estimated. Thus, it is necessary to select the reliable solutions priorly to perform a quantitative interpretation. In this chapter, we propose to select reliable Euler deconvolution estimates throughout the vertical derivatives of the total-field anomaly. The vertical derivatives of the total-field anomaly are good source locators because its decay rate with the distance is one order higher than the decay rate of the total-field anomaly. Here, for each position of the moving-data window we compute the standard deviation of the vertical derivatives of the total-field anomaly and we define the reliable source-location estimates as those estimates that are obtained with the largest standard deviations. Assuming tentative structural indices, the cluster of reliable solutions over the source will define the nature of the source (geometry of the source) and the mean of these estimates will define the position of the sources. We applied the methodology of the Chapter 3 to the Anitápolis anomaly, southern Brazil, and with the results we infer that a plug generated this anomaly and computed its depth to the top at 0.67 km. In Chapter 3 we also computed base-level estimates and plot the reliable estimates using our methodology. As we are selecting the solutions based on the standard deviation of the total-field anomaly inside a moving-data window, the source-position and the base-level estimates are plotted in the same positions and, thus, they cluster with the same structural index. This is an advance in the understanding of the base-level estimates because it shows that these estimates can also be used to define the correct structural index.

In Chapter 4 we plot the Euler estimates in plateau plots, i.e., for each struc-

tural index, each estimate is plotted against the central position of the moving-data window. In this kind of plot there is no need to select reliable estimates, all the estimates are plotted and analyzed. This visualization allows the understanding of the base-level estimates, defining the correct structural index in Euler deconvolution via base-level estimates. We show that assuming the correct structural index the base level estimates define plateaus of constant solutions over the source. Moreover, we show that the base-level estimates are non-linear and follow the pattern of the total-field anomaly, even when no background anomaly is present in the data. For isolated anomalies the depth or base-level estimates define the correct structural index, however for interfering anomalies only the base-level estimates define the correct structural index, on this methodology. We perform an interpretation of a large area in the Goiás Alkaline Province, central Brazil, and our results suggest that three plug intrusions give rise to the Diorama anomaly and dipole-like sources yielding Arenópolis and Montes Claros de Goiás anomalies.

## Chapter 2

# Amplitude of the magnetic anomaly vector in the interpretation of total-field anomaly data at low magnetic latitudes

This chapter has been submitted for publication in the journal *Journal of Applied Geophysics*.

### 2.1 Summary

We propose the use of the amplitude of the magnetic vector (amplitude data) for qualitative interpreting large areas at low magnetic latitudes. The amplitude data are weakly dependent on the magnetization direction vector. Hence, the amplitude data require no prior knowledge of the source magnetization direction. The amplitude data produce maxima over the causative sources, allowing the definition of the horizontal projections of the sources. This characteristic is attractive for interpretation at low magnetic latitudes because at these regions the interpretation of the total-field anomaly is not straightforward. We compute the amplitude data using the equivalent-layer technique to transform the total-field anomaly data into the three orthogonal components of the magnetic anomaly vector. We analyze the results of tests in synthetic data simulating a main geomagnetic field at high, mid and low latitudes, with sources ranging from compact to elongated forms, including a dipping source. These sources, that give rise to the simulated anomalies, have both induced and strong remanent magnetizations. By comparing the amplitude data

with the total gradient, we show that the amplitude data delineate the boundaries of the sources in a better way. We apply both the amplitude data and the total gradient to a real total-field anomaly over a large area of the Amazonian Craton, northern Brazil, located at low magnetic latitudes. The amplitude data show a better performance in delineating geologic bodies being consistent with the outcropping intrusions in the geologic map. Moreover, the amplitude data revealed new geologic bodies that were not present in the geologic map. The clear alignment of these new bodies with the outcropping intrusions suggested the continuity of these intrusions in depth. This result is a step forward in understanding this area, which has a poor geological knowledge. Hence, the amplitude data can provide an apparent-geologic map especially in areas at low latitudes with remanent magnetized bodies.

## 2.2 Introduction

The qualitative interpretation of total-field anomaly at low latitudes is a hard task due to the effects of the magnetization vectors either of the main geomagnetic field or the source. As a result, the total-field anomalies are rarely centered over the sources. However, even with these difficulties, the magnetic data are among the most important geophysical data used as an auxiliary tool in geologic mapping. To perform a fast qualitative interpretation of magnetic data aiming at yielding an apparent-geologic mapping, two approaches are usually adopted: linear inversion and linear transformation.

The linear inversion estimates a magnetization distribution (apparent-magnetization mapping) by solving a constrained linear inverse problem in which a regularizing function is minimized subject to fit the magnetic data. For example, Silva and Hohmann (1984) and Medeiros and Silva (1996) used the zeroth- and first-orders Tikhonov regularizations, respectively. Silva et al. (2010) combined minimization of first-order entropy with maximization of zeroth-order entropy of the estimated magnetization distribution. Barbosa and Silva (2011) presented a review of the entropic regularization in comparison with the first-order Tikhonov regularization to assist a geologist in obtaining a geologic map from magnetic data inversion. The biggest bottleneck for the linear inversion of magnetic data to produce an apparent-magnetization mapping is that it is computationally expensive.

Conversely, the second approach to yield an apparent-geologic mapping based on the linear transformations of the magnetic data is much less computationally expensive than the linear inversions. Linear magnetic transformations such as the reduction to the pole (RTP) and the total gradient (also known as the 3D analytic signal amplitude - 3D ASA) are widely used in the total-field anomaly to locate the sources. The RTP transforms the total-field anomaly into one that would have been

measured if the magnetization of the sources and ambient field were assumed to be vertical (Nabighian et al., 2005). In practice, to perform the RTP transformation the interpreter usually assumes that the sources have induced magnetization only. However, the magnetic induction may not be true, which yields wrong reduced-to-the-pole anomalies (Nabighian et al., 2005; Swain, 2000). Moreover, at low latitudes, especially within  $\pm 15^\circ$ , the RTP is unstable generating artifacts in the direction of the main field declination (Silva, 1986). Therefore, a successful RTP needs to overcome the unknown magnetization direction of the sources and the instability at low magnetic latitudes. In this way, improvements of the RTP were proposed in both space and Fourier domains to overcome these difficulties (Hansen and Pawlowski, 1989; Li et al., 2014; Li and Oldenburg, 2001; Mendonça and Silva, 1993; Silva, 1986; Swain, 2000).

The total gradient is defined as the square root of the sum of the squares of the partial derivatives of the total-field anomaly with respect to the  $x$ -,  $y$ - and  $z$ -directions. MacLeod et al. (1993), from a practical point of view, applied the total gradient (called 3D-ASA in Roest et al. (1992)) to locate the sources at low magnetic latitudes. Since then, the total gradient is being used as a standard interpretation technique at low magnetic latitudes, especially in Brazil. However, Li (2006) demonstrated that the definition of the sources with the total gradient is dependent on: i) the geometry of the source; ii) the magnetization direction of the source; and iii) the magnetization direction of the inducing field, among others. Therefore, at low latitudes and in areas with remanent magnetization the total gradient of the magnetic data as a tool in geologic mapping may not be suitable.

The amplitude of the magnetic anomaly vector (amplitude data) is defined as the square root of the sum of the squares of the three orthogonal components of the magnetic vector. Stavrev and Gerovska (2000) shown that the amplitude of the magnetic anomaly vector is weakly dependent of the magnetization direction. Gerovska and Stavrev (2006) analyzed the amplitude data and other transforms at low latitudes with synthetic and real isolated anomalies. Pilkington and Beiki (2013) compared the amplitude data with the total gradient and the normalized source strength, among others, for cases of remanent magnetization. One intrinsic advantage of the amplitude data over the two former transforms is that the amplitude data have the same scale of the total-field anomaly (nanotesla - nT), which makes the interpretation more tangible, while both the total gradient and the normalized source strength have units of derivative (nanotesla per meter - nT/m). Li et al. (2010) took advantage of the weak dependence of the amplitude of the magnetic anomaly vector on the magnetization direction to invert the amplitude data in the presence of remanent magnetization. Other authors also adopted the amplitude of the magnetic anomaly vector as the input for inversion in cases of remanence

magnetization and self-demagnetization (Krahenbuhl and Li, 2017; Li et al., 2012; Liu et al., 2013, 2015, 2017; Zuo et al., 2019). For a small area, Leão-Santos et al. (2015) applied the methodology of Li et al. (2010) to mineral deposits at low latitudes. Although Leão-Santos et al. (2015) focus on the inversion of the amplitude data; they carried out, in a small-scale mineral exploration, a geologic interpretation by correlating the estimated susceptibility distribution with the known geology and mineralized zones from drilling.

In this work, we propose the use of the amplitude of the magnetic anomaly vector to produce a qualitative interpretation in large-scale areas at low magnetic latitudes. This qualitative interpretation might be, for example, an initial attempt to produce an apparent-geologic map in large-scale prospecting during the early phase of exploration program when neither the conventional geologic mapping has been accomplished nor the exploration drilling has been planned. A second possibility of this qualitative interpretation might be, for example, an improvement (or updating) of an old geologic map, which were produced in a regional mapping scale. To calculate the amplitude of the magnetic anomaly vector, we compute the three orthogonal components of the magnetic vector from the total-field anomaly data using the equivalent-layer technique. The results obtained with the amplitude of the magnetic anomaly vector using synthetic and real data were compared with the results using the total gradient. The synthetic tests show the good performance of the amplitude data in generating maxima over the sources and thus defining the horizontal projections of the simulated sources. These results remain in anomalies generated by sources with strong remanent magnetization, located at high, mid and low-latitudes. Application to a real data set over a large area of the Amazonian Craton, north of Brazil, shows a striking correlation between the amplitude data and the mapped geology. The most striking feature of our results is that they disclose, possible, buried intrusions which were not mapped by the geologists. These new buried intrusions seem reliable because they exhibit the continuity of the outcropping intrusions.

## 2.3 Methodology

### 2.3.1 Total gradient

Let us adopt a right-handed Cartesian coordinate system with the  $x$ -axis pointing northing,  $y$ -axis pointing easting and  $z$ -axis pointing downward. The total gradient, at the  $i$ th observation point  $(x_i, y_i, z_i)$ ,  $i = 1, \dots, N$ , of the total-field anomaly is defined as:

$$TG_i \equiv TG(x_i, y_i, z_i) = \sqrt{\left(\frac{\partial T_i}{\partial x}\right)^2 + \left(\frac{\partial T_i}{\partial y}\right)^2 + \left(\frac{\partial T_i}{\partial z}\right)^2}, \quad (2.1)$$

where  $T_i$  is the total-field anomaly and  $\partial/\partial x$ ,  $\partial/\partial y$  and  $\partial/\partial z$  are the partial derivatives with respect to the coordinates of the observations in the  $x$ -,  $y$ - and  $z$ -directions and evaluated at the  $i$ th observation point  $(x_i, y_i, z_i)$ . We computed the total gradient with the formulation of Uieda et al. (2013), where the horizontal derivatives are computed in the spatial domain using finite differences and the vertical derivative is computed in the wavenumber domain.

### 2.3.2 Amplitude of the magnetic anomaly vector

The amplitude of the magnetic anomaly vector, at the  $i$ th observation point  $(x_i, y_i, z_i)$ ,  $i = 1, \dots, N$  is given by:

$$B_i \equiv B(x_i, y_i, z_i) = \sqrt{B_{xi}^2 + B_{yi}^2 + B_{zi}^2}, \quad (2.2)$$

where  $B_{xi}$ ,  $B_{yi}$  and  $B_{zi}$  are the three components of the magnetic anomaly vector in the  $x$ -,  $y$ - and  $z$ -directions (Blakely, 1996) at the  $i$ th observation point  $(x_i, y_i, z_i)$ . Although intuitive, the computation of the amplitude of the anomaly vector via Fourier domain is not advisable in some scenarios because the computation in uneven (or rugged) surfaces leads to wrong amplitude and shape results (Li and Li, 2014) and, in addition, at low latitudes it produces artifacts (Leão-Santos et al., 2015). Therefore, we computed the amplitude data from the total-field anomaly via the equivalent-layer technique (Dampney, 1969).

The equivalent-layer technique approximates a discrete set of potential-field observations produced by a 3D physical-property distribution by a 2D physical-property distribution, which is continuous and infinite, defined on a layer. In practice, a finite set of equivalent sources disposed in a layer with finite horizontal dimensions and placed between two to six times the data spacing below the observation surface approximates this 2D physical-property distribution (Dampney, 1969; Oliveira Jr et al., 2013). In our case, the discrete set of potential-field observations are a set of  $N$  observations of the total-field anomaly at the Cartesian coordinates  $x_i$ ,  $y_i$  and  $z_i$ , where  $i = 1, \dots, N$ , which are arranged represented by in the  $N$ -dimensional vector  $\mathbf{d}$ . The equivalent sources, setting up the equivalent layer, are a set of  $M$  dipoles distributed in a regular grid at a constant depth  $z_o$  (with  $z_o > z_i$ ) and with horizontal coordinates  $x_l$  and  $y_l$ , where  $l = 1, \dots, M$ . The unknown physical-property distribution within the equivalent layer is given by the magnetic-moment intensities of the  $M$  dipoles which are arranged in the  $M$ -dimensional vector  $\mathbf{p}$ . So, the total-field anomaly predicted by the equivalent layer

described in matrix notation is:

$$d(p) = Gp, \quad (2.3)$$

where  $\mathbf{d}_p$  is an  $N$ -dimensional vector whose  $i$ th element  $d_i(p)$  is the predicted total-field anomaly data predicted at the  $i$ th observation point and  $\mathbf{G}$  is the  $N \times M$  matrix of Green's functions. The  $il$ th element of the matrix  $\mathbf{G}$  is the total-field anomaly at the  $i$ th observation point produced by the  $l$ th equivalent source:

$$g_{il} = c_m \frac{\mu_0}{4\pi} \hat{\mathbf{F}}^T H_{il} \hat{\mathbf{h}}, \quad (2.4)$$

where  $c_m$  is a scaling factor to transform from Tesla to nanotesla,  $\mu_0$  is the permeability of vacuum or the magnetic constant,  $\hat{\mathbf{F}}$  and  $\hat{\mathbf{h}}$  are three-dimensional unit vectors with the direction cosines of the geomagnetic field and the magnetization vector assigned to the equivalent sources, respectively. The  $3 \times 3$  matrix  $\mathbf{H}_{il}$  is given by the second derivatives of the inverse distance function  $\left( r^{-1} = [(x_i - x_l)^2 + (y_i - y_l)^2 + (z_i - z_o)^2]^{-1/2} \right)$  with respect to the coordinates of the observations in the  $x$ -,  $y$ - and  $z$ -directions and evaluated at the  $i$ th observation point  $(x_i, y_i, z_i)$  and at the  $l$ th equivalent source  $(x_l, y_l, z_o)$ . In this process, we assume the knowledge of the magnetization direction of the main field and use these values for the magnetization direction of the sources.

The inverse problem of estimating the unknown magnetic-moment intensities, the parameter vector  $\mathbf{p}$  (in equation 2.3), from observed total-field data ( $\mathbf{d}^o$ ) is an ill-posed problem because its solution is non-unique and unstable. A stable estimate of  $\mathbf{p}$  can be obtained by using a parameter-space approach with the zeroth-order Tikhonov regularization (Tikhonov and Arsenin, 1977), i.e.:

$$\hat{\mathbf{p}} = (G^T G + \lambda I)^{-1} G^T \mathbf{d}^o, \quad (2.5)$$

where the superscript  $T$  stands for transpose,  $\lambda$  is a regularizing parameter,  $\mathbf{I}$  is an identity matrix of order  $M$  and  $\mathbf{d}^o$  is an  $N$ -dimensional vector whose  $i$ th element is the observed total-field anomaly at the  $i$ th observation point. We define the optimum  $\lambda$  using the L-curve criterion (Hansen, 1992). After estimating the magnetic-moment distribution  $\hat{\mathbf{p}}$  (equation 2.5), within the equivalent layer from the total-field anomaly, we apply a linear transformation to obtain the three orthogonal components of the magnetic anomaly vector and then compute the amplitude of the magnetic anomaly vector with equation 2.2. This transformation is given by:

$$B_\alpha = T^\alpha \hat{\mathbf{p}}, \quad (2.6)$$

where  $\mathbf{B}_\alpha$ ,  $\alpha = x, y$  and  $z$ , is an  $N$ -dimensional vector containing the transformed field (the three orthogonal components of the magnetic anomaly vector) and  $\mathbf{T}^\alpha$  is

an  $N \times M$  transformation matrix, i.e., an  $N \times M$  matrix of Green's functions whose elements are given by:

$$t_{il}^\alpha = c_m \frac{\mu_0}{4\pi} H_{il}^\alpha \hat{h}, \quad (2.7)$$

where  $H_{il}^\alpha$  is the  $\alpha$ th row of the matrix  $\mathbf{H}_{il}$  (the second derivatives of the inverse distance function).

The classic equivalent-layer technique, used in this work, has its performance limitations caused by the amount of data in solving the large linear system in equation 2.5. However, to perform the computation in larger datasets there are improvements of the equivalent-layer technique available (Davis and Li, 2011; Leao and Silva, 1989; Li and Oldenburg, 2010; Oliveira Jr et al., 2013; Siqueira et al., 2017).

All the software developed and used in this chapter is open source and was made available in 2019. The algorithm was developed in Python language and it is compatible with Python 2.7. The package with instructions is available at <https://github.com/ffigura/amplitude-vector-interpretation>.

## 2.4 Synthetic tests

We tested the performance of the amplitude of the magnetic anomaly vector in the interpretation of magnetic data in three distinct scenarios. In the first test, the simulated field has vertical incidence, while in the second and third tests we simulated fields at mid- and low-latitudes, respectively. The surveys were simulated on the plane  $z = -0.15$  km at a grid of  $100 \times 110$  observation points in the north- and east-directions, with regular spacing of 0.2 km. Figure 2.1 shows the prisms modeled as magnetic sources (Uieda et al., 2013) and labelled P1-P4. The source P1 is an inclined prism, dipping to the east, with top at 0.1 km, base at 2.1 km, width of 0.1 km, extension of 4 km and magnetization intensity of 7 A/m. The source P2 has an "L" shape, top at 0.2 km, base at 1.1 km and magnetization intensity of 3 A/m. Three prisms generate the source P3, all with the same magnetization intensity of 1.5 A/m. The two small-upper prisms have 1 km of extension, top at 0.2 km and base at 1 km, and the prism from below has extension of 4 km, top at 1 km and base at 5 km. Finally, the source P4 has extension of 2 km, top at 0.2 km, base at 5 km and magnetization intensity of 1.5 A/m. In all synthetic tests, the total-field anomalies were corrupted with pseudorandom Gaussian noise with zero mean and standard deviation of 1 nT. For the computation of the amplitude data we placed the equivalent sources at a depth  $z_o = 0.5$  km (two and a half times the grid spacing).

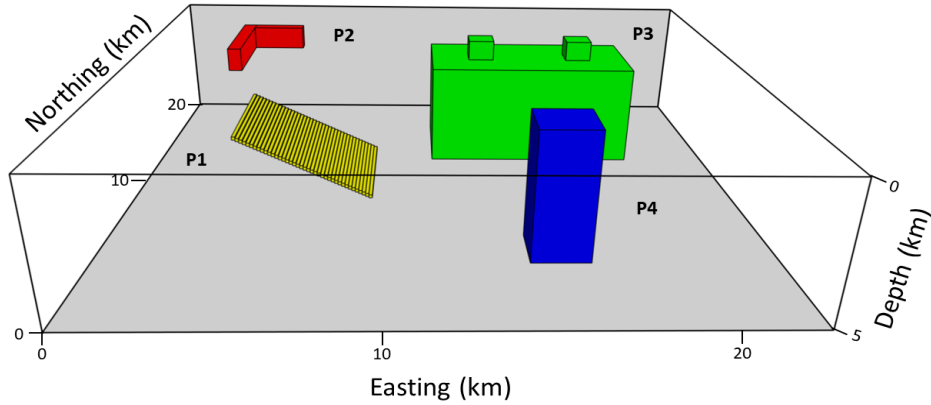


Figure 2.1: Simulated and labelled sources for the synthetic tests: P1 is a source simulating a dipping thin layer, P2 is an L-shaped source, P3 is a source generated by the superposition of three prisms and P4 is a vertical prism simulating a vertical intrusion.

#### 2.4.1 Test 1 – Simulated field at high latitude and induced magnetization

Figure 2.2a shows the total-field anomaly generated by a simulated geomagnetic field with vertical incidence, in this test all sources (P1-P4) are magnetized by induction only. The black polygons outline the horizontal projections of the simulated sources. Figure 2.2b and 2.2c shows the total gradient and the amplitude of the magnetic anomaly vector, respectively.

In the total gradient map (Figure 2.2b), the westernmost border of the source P1 is outlined; however, its easternmost border is not correctly enhanced. This happens because the source P1 is dipping to the east. The total gradient (Figure 2.2b) correctly outlines the sources P2 and P4; but fails in delimiting the source P3 completely. Notice that the total gradient enhances only the two shallow-seated prisms that set up the source P3; however, the deep-seated prism is neither detected nor delineated. Hence, the anomalies generated by the sources P1 and P3 have not been correctly defined because the total gradient is based on derivatives, so it enhances the short-wavelength components generated by the shallow-seated sources.

On the other hand, the amplitude of the magnetic anomaly vector generates maxima over the sources and provides an excellent definition of all sources' boundaries (P1-P4), as shown in Figure 2.2c. The amplitude data define the dipping source P1 and the source P3 with maxima over the shallowest part, decreasing toward the deepest part. This test demonstrates the potentiality of the amplitude of the magnetic anomaly vector (Figure 2.2c) in successfully defining the sources P1-P4 and

thus aiding in qualitative geophysical interpretation. In fact, this result resembles an anomaly generated by an induced field with vertical magnetization (Figure 2.2a) or a correctly reduced-to-the-pole anomaly.

In this test, we estimated the magnetic-moment distribution  $\hat{\mathbf{p}}$  (equation 2.5) within the equivalent layer from the total-field anomaly (Figure 2.2a) to compute the amplitude data (Figure 2.2c) by using equations 2.6, 2.7 and 2.2. Figure 2.2d shows the L-curve highlighting the optimum regularizing parameter  $\lambda = 1^{-15}$ , in red. Figure 2.2e shows the residuals of the fitting, i.e., the difference between the total-field anomaly (Figure 2.2a) and the predicted data (not shown). Notice that the residuals are small as compared with the range of amplitudes of the total-field anomaly (Figure 2.2a). Figure 2.2f shows histogram of the residuals, it has a bell shape with mean  $\mu = 0.01$  nT and standard deviation  $\sigma = 0.83$  nT, the red dashed line is a Gaussian distribution generated with these values. These results show the good fitting of the equivalent layer with the residuals exhibiting a Gaussian distribution. The good fitting of the equivalent layer allows us to use the estimated magnetic-moment distribution (not shown) to compute the three orthogonal components of the magnetic anomaly vector (equations 2.6 and 2.7) and, therefore, the amplitude data (equation 2.2).

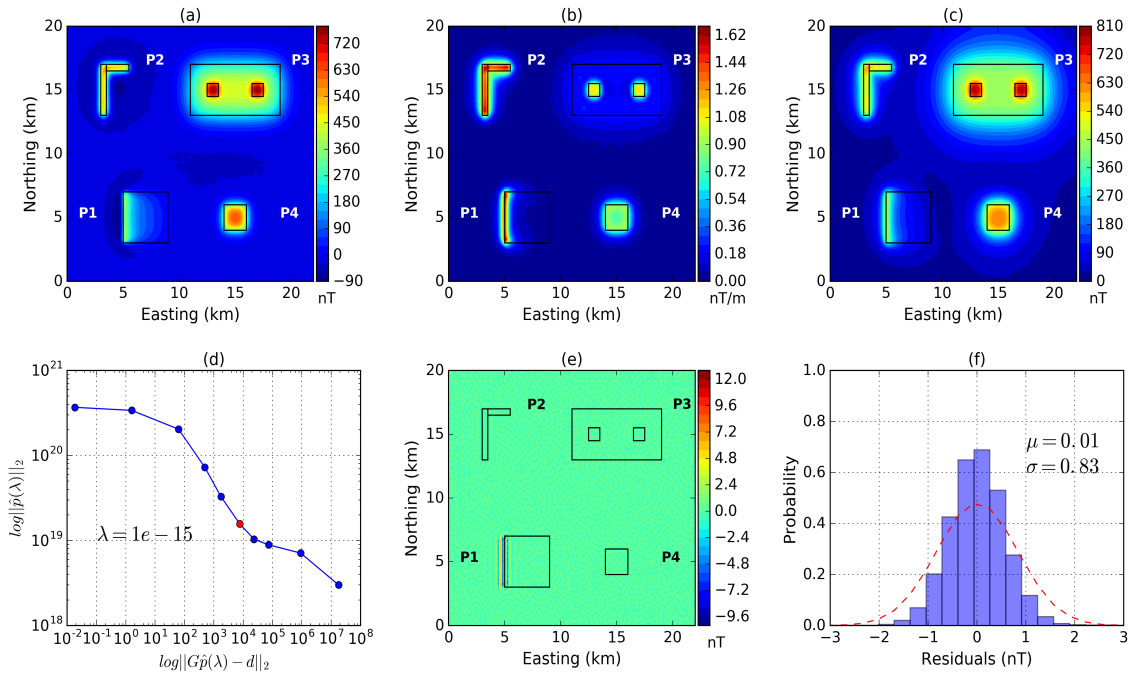


Figure 2.2: Test 1 – Test simulating an induced vertical magnetization. a) Total-field anomaly. b) Total gradient. c) Amplitude of the magnetic anomaly vector. d) L-curve highlighting the optimum regularizing parameter  $\lambda$  in red. e) Residuals. f) Histogram of the residuals with the mean  $\mu$  and the standard deviation  $\sigma$ , the dashed red line is the fitted Gaussian distribution. Black polygons outline the horizontal projections of the sources (labelled P1-P4).

## 2.4.2 Test 2 – Simulated field at mid-latitude and remanent magnetization

Figure 2.3a shows the total-field anomaly generated by a simulated geomagnetic field at mid-latitude with inclination and declination of  $45^\circ$ . In this test, the prisms P1-P3 have induced magnetization and the prism P4 has remanent magnetization with inclination and declination of  $60^\circ$ . Figure 2.3b and 2.3c shows the total gradient and the amplitude of the magnetic anomaly vector, respectively.

In the previous test, which simulates an induced vertical magnetization, most of the maxima amplitudes of the total gradient are centered over the sources as shown in Figure 2.2b. On the other hand, in this test, the maxima are over the southwest parts of the sources (Figure 2.3b) because the total gradient is dependent on the magnetization direction. Because of this characteristic, the source P4 cannot be directly interpreted from the total gradient map (Figure 2.3b); differently from the previous test (Figure 2.2b), where the horizontal projection of the source P4 can be easily delimited. In addition, the deepest edge of the source P1 in Figure 2.3b is less evident than in Figure 2.2b.

Figure 2.3c shows the amplitude data and, contrary to the total gradient, this output shows its weakly dependence on the magnetization direction. Over all the sources P1-P4 the maxima are well defined providing a good definition of most of boundaries of the sources as shown in Figure 2.3c. Moreover, the amplitude data (Figure 2.3c) are easier to interpret than the total-field anomaly (Figure 2.3a). It is comparable to the map of the total-field anomaly with vertical incidence (Figure 2.2a), which in turn is the goal of a reduction to the pole. However, the amplitude data are operationally simpler than the reduction to the pole of magnetic data because the latter requires the knowledge about the source magnetization direction whereas the amplitude data require only the knowledge about the magnetization direction of the geomagnetic field. This advantage allows the source P4, which is affected by remanent magnetization, to be enhanced in the amplitude data as shown in Figure 2.3c.

Figure 2.3d shows the L-curve highlighting the optimum regularizing parameter  $\lambda = 1^{-15}$ , in red. Figure 2.3e shows the residuals and Figure 2.3f shows the histogram of the residuals. The residuals have small values when compared with the total-field anomaly (Figure 2.3a) and this is reflected in the histogram with a bell shape with mean  $\mu = 0.06$  nT and standard deviation  $\sigma = 0.92$  nT, the red dashed line is a Gaussian distribution generated with these values.

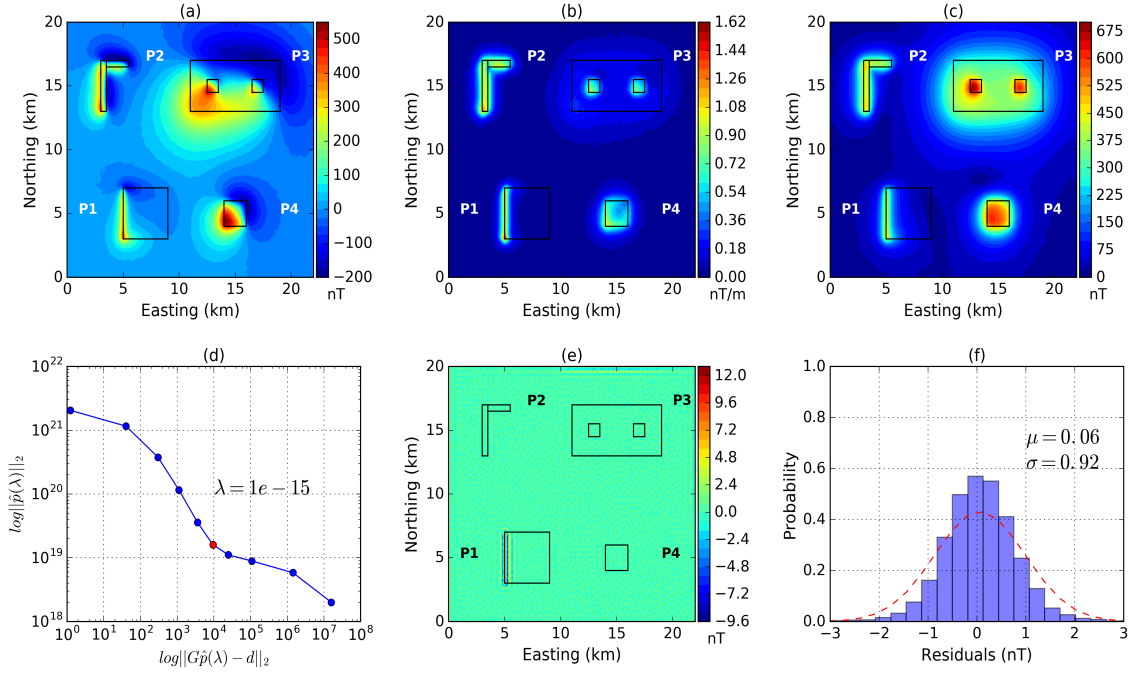


Figure 2.3: Test 2 – Test simulating the field at mid-latitude with sources affected by induction and remanent magnetizations. The source P4 has remanent magnetization and the sources P1-P3 are magnetized by induction only. a) Total-field anomaly. b) Total gradient. c) Amplitude of the magnetic anomaly vector. d) L-curve highlighting the optimum regularizing parameter  $\lambda$  in red. e) Residuals. f) Histogram of the residuals with the mean  $\mu$  and the standard deviation  $\sigma$ , the dashed red line is the fitted Gaussian distribution. Black polygons outline the horizontal projections of the sources (labelled P1-P4).

### 2.4.3 Test 3 – Simulated field at low latitude and remanent magnetization

Figure 2.4a shows the total-field anomaly generated by a simulated field at low latitude with inclination of  $-8^\circ$  and declination of  $-20^\circ$ . The sources P1 and P2 have induced magnetization and the sources P3 and P4 have strong remanent magnetizations. The source P3 has the same inclination and declination of  $45^\circ$  and the source P4 has the same inclination and declination of  $60^\circ$ . Notice that due to the remanence, the sources P3 and P4 give rise to magnetic anomalies with reverse polarizations in comparison with the anomalies produced by the sources P1 and P2 that are magnetized by induction only. Figure 2.4b and 2.4c shows the total gradient and the amplitude of the magnetic anomaly vector, respectively.

This third test simulates magnetic anomalies closer to a real-world scenario. We note that the total gradient (Figure 2.4b) enhances neither the shallowest edge of the source P1 nor its deepest edge. Rather, the total gradient (Figure 2.4b) enhances only the westernmost corners of the source P1. The source P2 cannot be correctly interpreted from the total gradient (Figure 2.4b), because there is a weak connection

between the maxima of the total gradient over the south and north edges. Similarly to the previous results (Figures 2.2b and 2.3b), the total gradient over the source P3 exhibits the maxima over its shallowest parts (Figure 2.4b). We note that the total gradient (Figure 2.4b) enhances the north and south boundaries of the source P4, but it does not suggest an isolated source with flat top.

Figure 2.4c shows that the amplitude of the magnetic anomaly vector produces a better location of all sources P1-P4 as compared with the total gradient (Figure 2.4b) even at low magnetic latitudes and in the presence of the strong remanent magnetizations (sources P3 and P4). Similarly to previous amplitude data results (Figures 2.2c and 2.3c), the horizontal projection of the shallowest edge of the source P1 is reasonable delimited by the amplitude data (Figure 2.4c), but its deepest edge is not defined. The source P2 is defined with higher amplitude in the east-west prism than in the south-north prism; however, is still notable that a continuous source gives rise to an isolated anomaly. These results over the sources P1 and P2, which are magnetized by induction, show that the amplitude data are sensitive to low magnetic inclinations; however, this sensitivity is slight, as shown by Stavrev and Gerovska (2000). Even at low magnetic latitudes and in the presence of the strong remanent magnetizations (sources P3 and P4), the amplitude data (Figure 2.4c) disclose the sources P3 and P4.

Figure 2.4d shows the L-curve highlighting the optimum regularizing parameter  $\lambda = 1^{-14}$ , in red. Figure 2.4e shows the residuals and Figure 2.4f shows the histogram of the residuals. In this test, the residuals also have small values when compared with the total-field anomaly (Figure 2.4a), long wavelengths artifacts generated in the direction of the magnetic declination are reflected in the computation of the amplitude data (Figure 2.4c), however these artifacts have small amplitudes and do not affect neither the computation of these data nor the qualitative interpretation. The histogram has a bell shape with mean  $\mu = 0.02$  nT and standard deviation  $\sigma = 1.85$  nT, the red dashed line is a Gaussian distribution generated with these values.

This test demonstrates the potentiality of the amplitude data (Figure 2.4c) in defining the maxima over the sources, which aid in defining their locations, even at low-magnetic latitudes and in the presence of sources with strong remanent magnetizations.

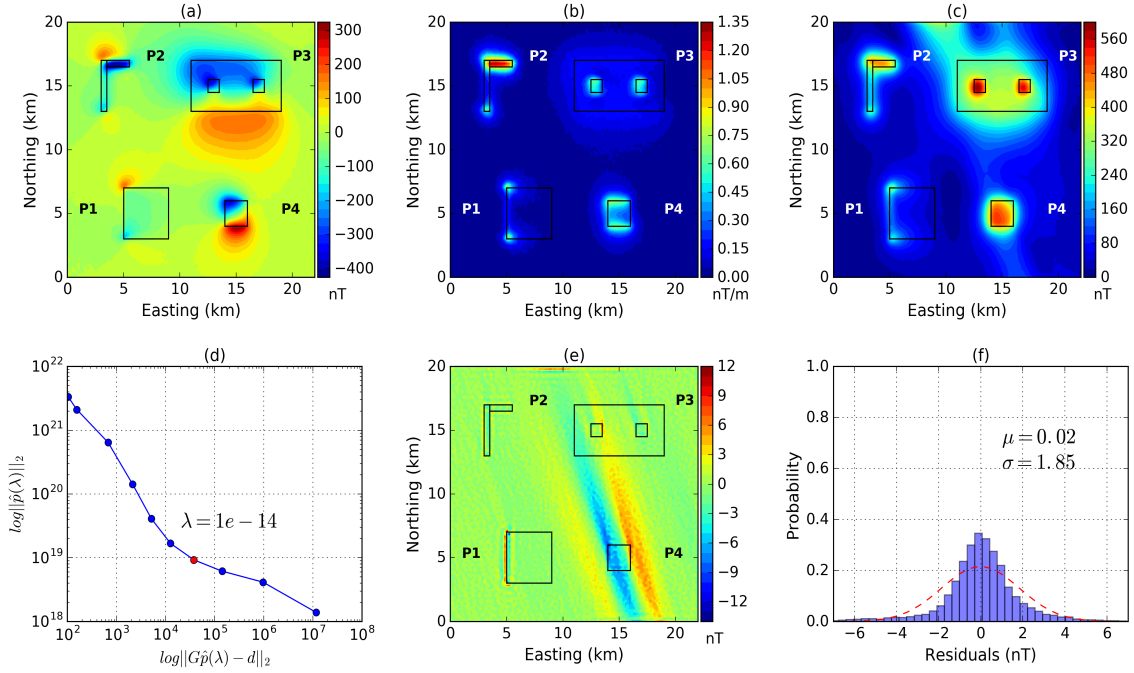


Figure 2.4: Test 3 – Test simulating a field at low latitude with sources affected by induction and remanent magnetizations. The sources P3 and P4 have remanent magnetizations and the sources P1 and P2 are magnetized by induction only. a) Total-field anomaly. b) Total gradient. c) Amplitude of the magnetic anomaly vector. d) L-curve highlighting the optimum regularizing parameter  $\lambda$  in red. e) Residuals. f) Histogram of the residuals with the mean  $\mu$  and the standard deviation  $\sigma$ , the dashed red line is the fitted Gaussian distribution. Black polygons outline the horizontal projections of the sources (labelled P1-P4).

## 2.5 Application to real data set

The Amazonian Craton, northern Brazil, is one of the main tectonic units of the South American Platform. (Almeida et al., 1981). Santos et al. (2000) divide the Amazonian Craton in seven tectonic provinces and our study area is located in two of these provinces: the Central Amazonian Province (CAP) and the Carajás Mineral Province (CMP). According to Klein et al. (2017), this region of the CAP comprises widespread volcano-plutonic associations, continental sedimentary covers, and small and sparse (unmapped) basement inliers. However, the geological knowledge about this area is poor because of the difficult access, devoid of detailed geologic mapping and geophysical information (Klein et al., 2017). The CMP is a highly mineralized metallogenic province known for its deposits of gold, copper, iron and manganese, among others (Grainger et al., 2008).

The real aeromagnetic data (Carajás survey) were acquired between 2013 and 2014 (CPRM, 2015). The flight lines in the north–south direction were acquired every 3 km, the tie lines were acquired every 12 km and the flight height was at 0.9 km. Figure 2.5 a shows the geologic map of the study area at the scale 1:1,000,000, modi-

fied from Vasquez et al. (2008). The main part of the study area is in the Iriri-Xingu Domain, in the CAP, surrounded by the Rio Maria Domain, in the CMP. The thick line in Figure 2.5a defines the border of the domains and the thin lines are the mapped faults. The main occurrences in the Iriri-Xingu Domain are labelled in Figure 2.5a as I1-I5, where I1 are effusions of andesite, I2 are effusions of rhyolite and I3-I5 are granite intrusions. The main occurrences in the Rio Maria Domain are labelled in Figure 2.5a as R1-R5, where R1 and R2 are granitoids, R3 is a greenstone belt, R4-R6 are sedimentary covers (sandstones and shales) and R7 is a magmatic intrusion. The inset shows the survey area in yellow, located in the north part of Brazil, the study area in blue and the black star points to Serra Pelada mine.

Figure 2.5b shows the total-field anomaly of the study area with a grid of  $147 \times 104$  points in the north and east directions, regularly spaced at 0.75 km. We highlight some anomalies with arrows and labelled as A1-A5. Figure 2.5c shows the total gradient using a normalized color scale with the cumulative distribution function. The total gradient emphasizes anomalies A1-A3, which are isolated and strong. However, the total gradient did not highlighted A4 as an isolated source; rather, it suggests multiple magnetic sources in a region where the total-field anomaly (Figure 2.5b) show a dipolar anomaly. Recall that the source P4 in test 3 was highlighted in the south and north borders by the total gradient (Figure 2.4b) resembling that two sources generated the anomaly, despite it be a single source (Figure 2.4a). As shown, the characteristics of the source and of the incident field have strong effects in the total gradient. Anomaly A5 is highlighted as a trend in the west-east direction.

For computing the amplitude data, we used the values of inclination of  $-8^\circ$  and declination of  $-20^\circ$  (Chulliat et al., 2014). Figure 2.5d shows that the amplitude data identify the maxima coincide with the anomalies A1-A5 (pinpointed by the arrows). In this map, the anomalies A1 and A4 are identifiable as single sources. Notice that in the total-field data of Figure 2.5b the anomaly A1 has opposite phase in relation to the expected phase for the area, suggesting a strong remanent magnetization. Recall that the source P4 in the test 3 simulated the shape of this anomaly, as shown in Figure 2.4a. In the amplitude map (Figure 2.5d), the anomalies A2, A3 and A5 have their shapes similar to the amplitude data of the source P3 in the synthetic tests (Figures 2.2c-2.4c). In Figure 2.5d, over the anomalies A2, A3 and A5, the amplitude data show at least three maxima surrounded by lower values that are not zero, but with amplitudes close to half of their maxima. Based on our synthetic tests, this characteristic of the amplitude data suggests that the magnetized sources that give rise to the anomalies A2, A3 and A5 may be a complex geologic unit composed of wide and deep-seated bodies overlaid by small and shallow-seated bodies.

As pointed before, the amplitude data of Figure 2.5 were generated via the

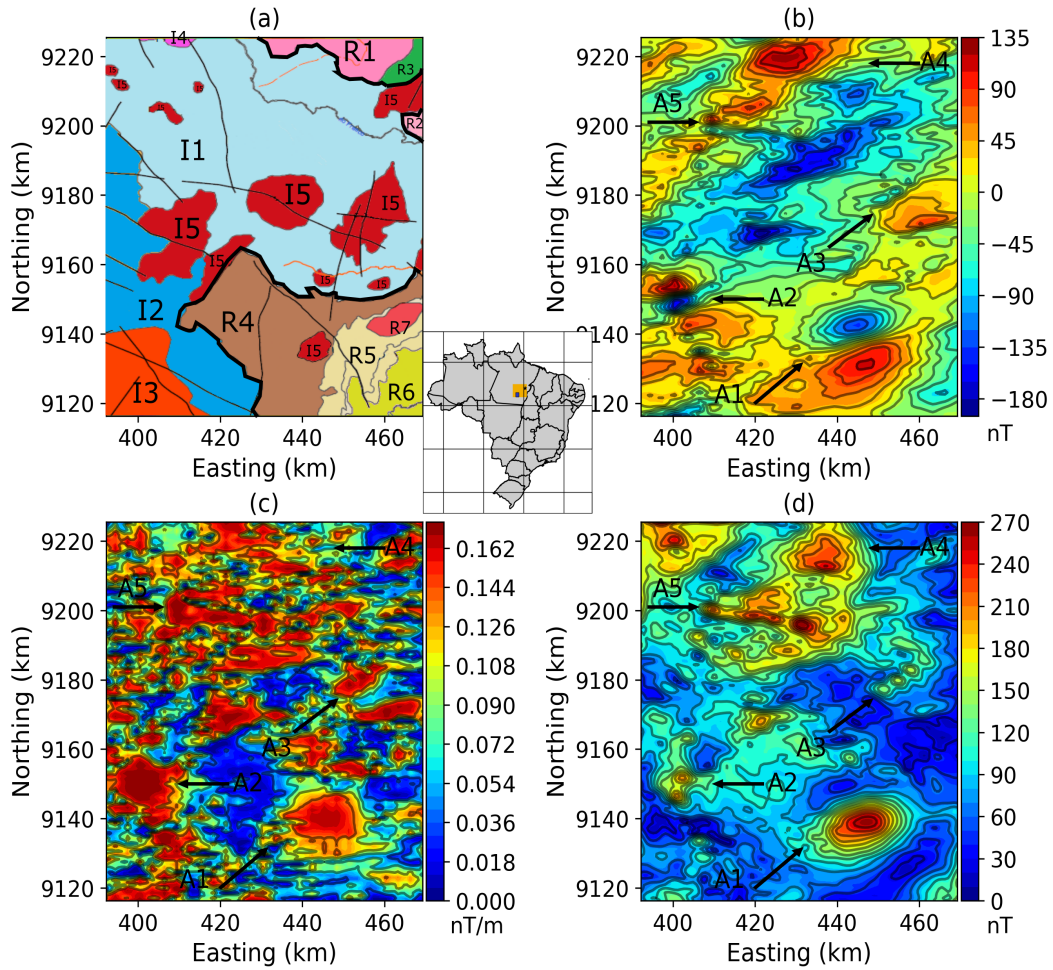


Figure 2.5: Real data application. a) Geologic map, modified from Vasquez et al. (2008), the labels correspond to the domains Rio Maria (R) and Iriri-Xingu (I). The inset shows the survey in yellow and the study area in blue, the star locates the Serra Pelada mine. b) Observed total-field anomaly. c) Total gradient. d) Amplitude of the magnetic anomaly vector. The arrows point to notable anomalies labelled A1-A5.

equivalent-layer technique (equations 2.5-2.7 and 2.2) by placing the layer at 3.75 km deep (five times the grid spacing) and setting the regularizing parameter  $\lambda$  equal to  $1^{-19}$ . Figure 2.6a shows the L-curve plotted on a log-log scale in which the value of  $\lambda$  (red dot) closest to the corner of the L-curve is selected as the optimum regularizing parameter in equation 2.5. Figure 2.6b shows the predicted total-field anomaly by using the equivalent-layer technique (equation 2.3) and Figure 2.6c shows the residuals between the predicted (Figure 2.6b) and the observed (Figure 2.5b) total-field anomalies. Notice that only random high frequency artifacts are present in the residuals. Figure 2.6d shows the histogram of the residuals with  $\mu = -0.01$  nT and  $\sigma = 1.98$  nT, the red dashed line shows the fit of these data with a Gaussian distribution. In this real data application, the data residuals (Figure 2.6c and 2.6d) are close to 0 nT; then, the data fitting is acceptable, the estimated

magnetic-moment distribution ( $\hat{p}$  in equation 2.5 with  $\lambda = 1^{-19}$ ) can be accepted, and the amplitude data (Figure 2.5d) can be obtained using equations 2.4, 2.7 and 2.2.

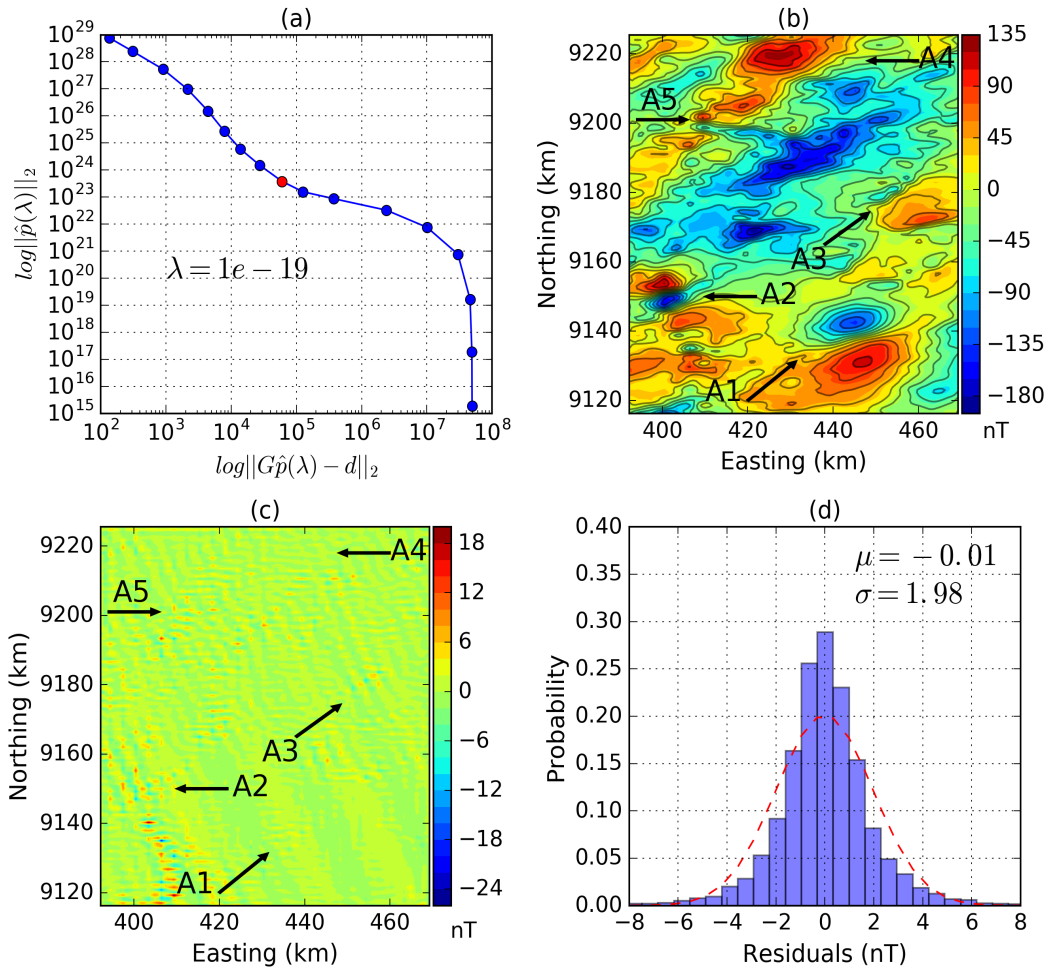


Figure 2.6: Real data application. (a) L-curve plotted on a log–log scale where the optimum regularizing parameter  $\lambda$  is highlighted in red dot. (b) Predicted total-field anomaly from the equivalent layer. (c) Residuals. (d) Histogram of the residuals with the mean  $\mu$  and the standard deviation  $\sigma$ , the dashed red line is the fitted Gaussian distribution.

Figure 2.7 shows the amplitude of the magnetic anomaly vector (Figure 2.5d) overlaid by a simplification of the geologic map where the intrusions are in transparent red polygons (Figure 2.5a). Notice in Figure 2.7 that the anomaly A1 correlates with an outcropping intrusion I5. The anomalies A2 and A4 do not agree with any outcropping geologic units in the geologic map. The anomaly A2 may suggest the continuity in depth of a mapped intrusion I5 possibly masked by the overlying effusions of rhyolite (I2 in Figure 2.5a) and the anomaly A4 may suggest a buried structure overlaid by effusions of andesite (I1 in Figure 2.5a). The anomaly A3 correlates with an outcropping intrusion I5 in the geologic map. Finally, the northwest–southeast-trending anomalies A5 suggest the continuity of intrusions I5

in depth.

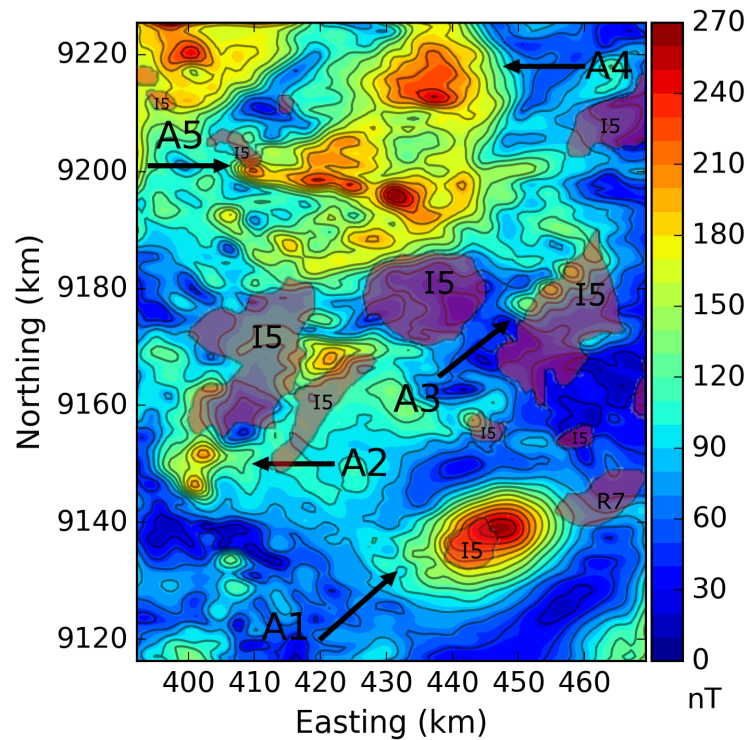


Figure 2.7: Amplitude of the magnetic anomaly vector (Figure 2.5d) overlaid by the outcropping intrusions (transparent red polygons) shown in the geologic map (Figure 2.5a). The arrows point to notable anomalies labelled A1-A5.

## 2.6 Final Considerations

We have illustrated the potential of the amplitude of the magnetic anomaly vector as an alternative method to locate the sources and to delimitate the boundaries, even at low-magnetic latitudes and in the presence of sources with strong remanent magnetizations. The amplitude data have the advantage of being weakly sensitive to dipping sources, low magnetic inclinations and remanent magnetizations. One advantage in the computation of the amplitude data over other techniques, for example the RTP, is the required knowledge of the magnetization direction about the incident field only, and not of the sources. The computation of the amplitude data via the equivalent-layer procedure overcomes the computation via Fourier domain because the latter fails at low latitudes, requires a regular grid of observations and a flat observation surface. Another advantage of the amplitude data is related, intrinsically, to the physical nature of the amplitude data, which have the same unit of the total-field data, thus allowing a tangible interpretation. Synthetic tests showed that the amplitude of the magnetic anomaly vector have a superior performance in enhancing the location of the sources as compared with the total gradient that is

a standard procedure in magnetic interpretation, especially at low latitudes. The interpretations of the amplitude data in scenarios simulating mid and low latitudes are comparable to interpret magnetic anomalies produced by vertically magnetized sources. In these conditions, the interpretation using either the total-field anomaly or the total gradient fails. Application to a real aeromagnetic data close to the magnetic equator showed the potentiality of the interpretation with the amplitude data. The interpretation of the amplitude data confirmed some outcropping intrusions present in the geologic map. Moreover, the amplitude data revealed new geologic bodies that were not present in the geologic map. The positions and the orientations of these new geologic bodies suggested the continuity of outcropping intrusions in depth. This result is a step forward in understanding this study area, which has a poor geological knowledge. An attractive characteristic of the amplitude data as a tool in enhancing the magnetic data is their potentiality to be used at the early stages of an exploration program when the geologic knowledge is at the beginning. In this scenario, the amplitude data can be jointly used with other data aiding either in the geologic mapping or in the geophysical interpretation. In this way, the amplitude data could provide quickly and conveniently an apparent-geologic map in areas where the geology has only been mapped in reconnaissance fashion due to the characteristics of the areas, e.g., poor access (forests and mountains) or poor rock exposures. Finally, an important aspect of the amplitude of the magnetic anomaly vector is its positive correlation with the geology and therefore with gravity data. In future works, this aspect deserves to be explored.

# Chapter 3

## Reliable Euler deconvolution estimates throughout the vertical derivatives of the total-field anomaly

This chapter has been improved and published "Melo, F. F., Barbosa, V. C., 2020. Reliable Euler deconvolution estimates throughout the vertical derivatives of the total-field anomaly. *Computers & Geosciences* 138, 104436".

### 3.1 Summary

We propose a novel methodology to select reliable Euler deconvolution estimates throughout the vertical derivatives of the total-field anomaly grounded on the capability of this quantity to locate anomalies due to its higher signal decay with distance. In applying Euler deconvolution to a small moving-data window, we compute the standard deviation of the vertical derivatives of the total-field anomaly for each data window. Then, we define the reliable source-location estimates as those estimates that are obtained by using the data windows with the largest standard deviations of the vertical derivatives of the total-field anomaly. For all tentative values of the structural index (SI), the reliable estimates with tight clustering define the correct SI and the mean of these estimates define the source position. Our methodology successfully works in two complex scenarios. In the first one, multiple sources with distinct SI generate a total-field anomaly which in turn is corrupted by an additive nonlinear background that simulates a regional field. This regional field strongly interfere the anomalies produced by the sources, changing their amplitudes and shapes. In the second scenario, nearby sources give rise to strongly

interfering anomalies. In both scenarios, our methodology correctly defines the SIs, the horizontal positions and the depths of the causative sources. Application to real magnetic anomaly from southern Brazil allows inferring the presence of a plug intrusion.

## 3.2 Introduction

Euler deconvolution (Barbosa et al., 1999; Reid et al., 1990) is the most popular technique for fast interpretation of potential-field data. It works with potential-field measurements, their gradients, and a given integer number called the structural index (SI), which in turn depends on the nature (type) of the geologic source (Reid et al., 2014; Reid and Thurston, 2014). Mathematically, Euler deconvolution assumes a tentative SI, solves a system of equations in a moving-data window scheme and estimates the four parameters: base level, horizontal and vertical positions of a geologic source.

Traditionally, for each tentative SI, one map is generated where the estimates of the source horizontal and vertical coordinates obtained by Euler deconvolution are plotted. Specifically, the estimates of the source horizontal coordinates are plotted in the plan view ( $x - y$  plane) of the study area (Reid et al., 1990), and usually the source depth (vertical coordinates) estimates are plotted in different color or size. In this case, base-level estimates are computed but usually neglected. When the correct SI is used the estimates cluster over the source (Thompson, 1982). The cumbersome with this plot is the large amount of solutions (Barbosa and Silva, 2011). In order to deal with the spray of solutions and define the correct SI some authors developed some criteria, e.g., Thompson (1982) and Reid et al. (1990) accept solutions based on the depth uncertainty. Fairhead et al. (1994) computed the maximum of the horizontal gradient of the reduced-to-the-pole anomaly to accept solutions. Mikhailov et al. (2003) and Ugalde and Morris (2010) filtered solutions using clustering techniques based on artificial intelligence and fuzz  $c$ -means, respectively. FitzGerald et al. (2004) provided an overview on best practices to select the solutions and proposed new ones for the extended Euler technique (Mushayandevu et al., 2001; Nabighian and Hansen, 2001). The FitzGerald et al. (2004) overview totalizes 17 discrimination techniques aiming to select the more reliable Euler solutions considering different SIs. The large amount of discrimination techniques presented by FitzGerald et al. (2004) show the complexity of distinguishing reliable Euler solutions from spurious ones considering distinct geologic scenarios. Uieda et al. (2013, 2014) adapted the solution from Beiki and Pedersen (2010) ranking the solutions based on the estimated error computed from all parameters. Alternatively, Silva and Barbosa (2003), Melo et al. (2013) and Melo and Barbosa (2018)

plot all estimates separately against the central position of the moving-data window, resulting in four maps, one for each estimate. In this procedure, there is no need to select reliable estimates or deal with the spray of solutions because all solutions are plotted.

Some free codes are available to perform Euler deconvolution. For profile data and not open source, Durrheim and Cooper (1998) estimated the position and base level and Cooper (2006) obtained the dip and susceptibility from dikes with a modified version using the Hough transform. For gridded data, and not open source code, FitzGerald et al. (2004) implemented the extended Euler. For gridded data and open source codes, Gerovska and Araúzo-Bravo (2003) estimated the position and the SI based on the properties of the differential similarity transformation and Uieda et al. (2013, 2014) estimated the source position and the base level in the standard way. The extended Euler (Mushayandebvu et al., 2001; Nabighian and Hansen, 2001), implemented by FitzGerald et al. (2004), assumes a new system of equations with the Hilbert transform. In this new system, the base level is set to zero, as the result of the Hilbert transform of a constant.

In this work, we analyze Euler deconvolution solutions selecting the reliable estimates throughout the moving-data windows with the largest standard deviations of the vertical derivatives of the total-field anomaly. Synthetic tests with strongly interfering anomalies show the robustness of our methodology to: i) select reliable Euler estimates; ii) determine the SI correctly and; iii) locate the source positions. These synthetic tests are produced by i) isolated sources in the presence of a non-linear background simulating a regional field; and ii) multiple and closely separated sources. The field results from the aeromagnetic data, southern Brazil, suggest that a plug intrusion generates the Anitápolis anomaly.

### 3.3 Methodology

Let us adopt a right-handed Cartesian coordinate system with the  $x$ -axis pointing to north, the  $y$ -axis pointing to east, and with the  $z$ -axis pointing downward. Reid et al. (1990) defined the Euler deconvolution as:

$$(x - x_o) \frac{\partial h}{\partial x} + (y - y_o) \frac{\partial h}{\partial y} + (z - z_o) \frac{\partial h}{\partial z} = \eta(b - h), \quad (3.1)$$

where  $x_o$ ,  $y_o$  and  $z_o$  are source positions,  $x$ ,  $y$  and  $z$  are the observation position,  $h = h(x, y, z)$  is the total-field anomaly and  $\partial h/\partial x$ ,  $\partial h/\partial y$  and  $\partial h/\partial z$  are its gradients with respect to the variables  $x$ ,  $y$  and  $z$ , respectively. In equation 3.1,  $\eta$  is an integer number, named structural index (SI), which depends on the source type and  $b$  is a base level or data background. Details about the theory of Euler deconvolution are

available in the Appendix A.

By applying Euler deconvolution with a moving-data window scheme using a tentative value of SI, we obtain the estimated parameters  $\hat{x}_o^k$  and  $\hat{y}_o^k$  (horizontal source positions),  $\hat{z}_o^k$  (vertical source position) and  $\hat{b}^k$  (base level), for the  $k$ th position of the moving-data window. Hence, equation 3.1 can be written as:

$$\hat{x}_o^k \frac{\partial h_j}{\partial x} + \hat{y}_o^k \frac{\partial h_j}{\partial y} + \hat{z}_o^k \frac{\partial h_j}{\partial z} + \eta \hat{b}^k = x_j \frac{\partial h_j}{\partial x} + y_j \frac{\partial h_j}{\partial y} + z_j \frac{\partial h_j}{\partial z} + \eta h_j, \quad (3.2)$$

where the subscript  $j$  is related to the  $j$ th observation position  $(x_j, y_j, z_j)$  inside the  $k$ th moving-data window. The estimates  $\hat{x}_o^k$ ,  $\hat{y}_o^k$ ,  $\hat{z}_o^k$  and  $\hat{b}^k$  in each  $k$ th position of the moving-data window are the Euler solutions to be visualized, which depend on the assumed SI.

In matrix form, the solution of the system of equations described in equation 3.2, for each  $k$ th position of the moving-data window via the least-squares method is:

$$\mathbf{p}^k = (\mathbf{A}^{kT} \mathbf{A}^k)^{-1} \mathbf{A}^{kT} \mathbf{d}^k, \quad (3.3)$$

where  $\mathbf{p}^k$  is a vector with the four estimated parameters  $(\hat{x}_o^k, \hat{y}_o^k, \hat{z}_o^k$  and  $\hat{b}^k)$ ,  $\mathbf{A}^k$  is the  $M \times 4$  sensitivity matrix whose elements of the  $j$ th row are:  $a_{j1}^k = \partial h_j / \partial x$ ,  $a_{j2}^k = \partial h_j / \partial y$ ,  $a_{j3}^k = \partial h_j / \partial z$  and  $a_{j4}^k = \eta$ ,  $j = 1, \dots, M$  where  $M$  is the number of observations in a moving-data window. The  $j$ th element of the  $M$ -dimensional data vector  $\mathbf{d}^k$  is  $d_j^k = x_j(\partial h_j / \partial x) + y_j(\partial h_j / \partial y) + z_j(\partial h_j / \partial z) + \eta h_j$ . In equation 3.3, the superscript  $T$  stands for transposed.

To perform the Euler deconvolution the derivatives of the gridded potential-field data are computed in Fourier domain (Blakely, 1996). However, measured gradient data can be used if available (Schmidt et al., 2004). In cases of low signal to ratio, the filtering of random noise can be achieved prior to run the Euler deconvolution (Florio et al., 2014). The data window is moved over the whole data grid and, at each position of data window, the four Euler estimates  $(\hat{x}_o^k, \hat{y}_o^k, \hat{z}_o^k$  and  $\hat{b}^k$  in equation 3.3) are obtained. We follow the recommendations of Reid et al. (2014) regarding the size of the moving-data window related to the grid space and depth of investigation. These authors stated that the window size must be greater than twice the measured data grid interval and greater than half the desired depth of investigation.

In this work, we introduce a novel criterion to distinguish reliable solutions from spurious ones. We keep only a percentage of the moving-data windows ranked by the largest standard deviations of the vertical derivatives of the total-field anomaly (third column of the sensitivity matrix in equation 3.3). This is achieved, in the  $k$ th window, by computing the sample standard deviation (Gubbins, 2004) of the vertical derivatives of the total-field anomaly:

$$s^k = \sqrt{\frac{\sum_{j=1}^M (a_{j3}^k - \mu^k)^2}{M - 1}}, \quad (3.4)$$

where  $\mu^k$  is the mean of the vertical derivatives of the total-field anomaly in the  $k$ th window. Next, we select the moving-data windows with the largest standard deviation and plot the corresponding Euler solutions for each tentative SI on distinct plots. The percentage of moving-data windows selected is defined based on the dataset; this selection is accomplished by decreasing the amount of selected solutions until a cluster is defined over a source. The reliable selected estimates lie over the sources, thus reducing the spray of solutions. The best SI is the one that produces the tightest cluster of the source-position or the base-level estimates. Finally, the mean of depth estimates defines the optimum depth to the top or to the center of the source. Details about the plot of the solutions in Euler deconvolution are available in the Appendix A.

The physical basis to the choice of reliable Euler solutions related to the data windows with largest standard deviations of the vertical derivative of the total-field anomaly is its ability to locate interfering anomalies due to its higher signal decay with distance. In the interpretation of non-interfering anomalies via Euler deconvolution, the largest standard deviations of other quantities - such as the total-field anomaly or its horizontal derivatives - could also be employed to distinguish reliable Euler solutions from spurious ones. However, these quantities fail in interpreting interfering anomalies, whereas the vertical derivative of the total-field anomaly was more robust.

All the software developed and used in this chapter is open source and was made available in 2019. The algorithm was developed in Python language and it is compatible with both Python 2.7 and Python 3.7. The package with instructions is available at <https://github.com/ffigura/Euler-deconvolution-python>.

## 3.4 Synthetic tests

### 3.4.1 Test 1 - Distinct SIs and strong nonlinear magnetic base level

Figure 3.1a shows four prisms that represent the sources of the simulated total-field anomaly in Figure 3.1b. The prisms labelled P0-P3 in Figure 3.1a simulate geological sources with distinct SIs. The prism P0 which simulates a contact has  $SI = 0$ , top at 0.2 km and magnetization intensity of 0.3 A/m. The prism P1 simulates a thin dike which has  $SI = 1$ , top at 0.6 km, 0.4 km width and magnetization intensity of 2 A/m. The prism P2 which simulates a vertical intrusion has  $SI = 2$ , top

at 0.6 km, equal horizontal dimensions of 0.3 km and magnetization intensity of 10 A/m. Finally, the prism P3 simulates a spherical source which has  $SI = 3$ , radius of 0.2 km, center at 1.050 km and magnetization intensity of 25 A/m. The sources have induced magnetization with inclination of  $60^\circ$  and declination of  $-20^\circ$ . We simulated a survey on a regular grid of 120 x 140 observation points in the  $x$ - and  $y$ - directions equally spaced at each 0.2 km and the survey height is simulated at  $z = -0.1$  km. Figure 3.1b shows the simulated total-field anomaly (Uieda et al., 2013) corrupted with pseudorandom Gaussian noise with zero mean and standard deviation of 0.1% of the maxima absolute amplitude of the data. Figure 3.1c shows a simulated nonlinear background generated by the polynomial:

$$b(x_j, y_j) = \frac{(x_j + 10)(y_j + 10)}{5}, \quad (3.5)$$

where the subscript  $j$  is related to the  $i$ th observation point  $(x_j, y_j)$ . As pointed in Melo and Barbosa (2018), this anomaly can simulate a regional field, a strongly interfering anomaly, or a poor definition of the IGRF. Notice that this base level has values of amplitudes higher than the anomalies in Figure 3.1b, thus generating strongly interfering anomalies after its addition to the original data (Figure 3.1a). Figure 3.1d shows the noise corrupted magnetic anomaly generated by the addition of the total-field anomaly in Figure 3.1b with the nonlinear base level in Figure 3.1c. Notice in Figure 3.1d that the superposition effect due to the addition of the simulated nonlinear base level (Figure 3.1c) yields a strong interference in the original anomaly shown in Figure 3.1b. Therefore, the generated data (Figure 3.1d) no longer have the same shape of the original anomalies (Figure 3.1b). In fact, at some locations the amplitude of the magnetic data yielded by the nonlinear base level is greater than twice the original anomaly (Figure 3.1b) generating strongly interfering anomalies (Figure 3.1d). The black polygons in Figure 3.1b-d outlines the horizontal projections of the simulated sources shown in perspective view in Figure 3.1a.

We run Euler deconvolution using the magnetic data shown in Figure 3.1d. We use a moving-data window of  $9 \times 9$  points solving equation 3.3, for each position of the moving-data window and we kept the best 1182 estimates (8% of the solutions). Here, we only select the Euler deconvolution estimates produced by the moving-data windows with the largest standard deviations of the vertical derivatives of the magnetic data (Figure 3.1d). By applying the Euler deconvolution to the interfering synthetic magnetic data shown in Figure 3.1d, we will estimate the depths to the tops of sources P0-P2 and the depth to center of the source P3 (Reid and Thurston, 2014).

Figure 3.2 shows the source-position and base-level estimates, respectively, for all moving-data windows. Notice that the spurious solutions do not allow the iden-

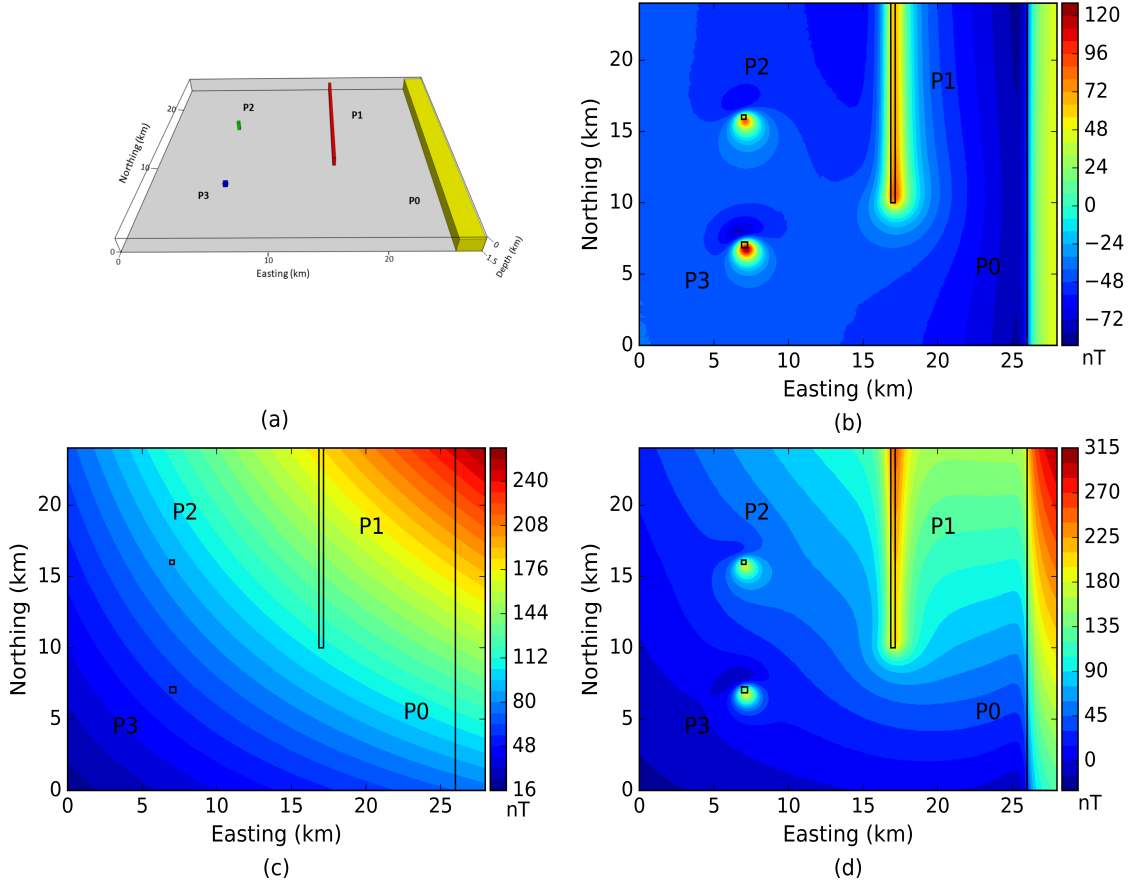


Figure 3.1: Synthetic test 1: Simulated sources and magnetic anomaly. (a) Simulated sources P0-P3 represent a contact ( $SI = 0$ ), a dike ( $SI = 1$ ), a vertical intrusion ( $SI = 2$ ) and a spherical source ( $SI = 3$ ), respectively. (b) Noise-corrupted total-field anomaly (the noise standard deviation is 0.12 nT) generated by the sources shown in panel a. (c) Nonlinear base level simulating a regional field. (d) Noise-corrupted magnetic anomaly obtained by adding the total-field anomaly shown in panel b to the nonlinear base level shown in c. The black polygons in panels b-d outline the horizontal projections of the simulated sources shown in panel a.

tification of the sources, outlined by red polygons.

Figure 3.3 shows the results of the proposed methodology where the horizontal position estimates (in circles) of the sources are displayed over the map of the magnetic anomaly (in grayscale) and the depth estimates are represented by different colors. Figure 3.3a-d shows the Euler estimates assuming the  $SI = 0, 1, 2$  and  $3$ , respectively. The tightest cluster of the estimates over the source P0 in Figure 3.3a defines the depth to the top of the contact at 0.223 km. Figure 3.3b shows tightest cluster of the source-position estimates assuming the  $SI = 1$ , the correct one for the source P1. In this cluster of estimates, the mean of the depth estimates is 0.627 km, which is very close to the depth to the top of the simulated thin dike P1. In Figure 3.3c the tightest cluster of the estimates is over the source P2 because we assume the  $SI = 2$ . The mean of the depth estimates in this cluster defines the

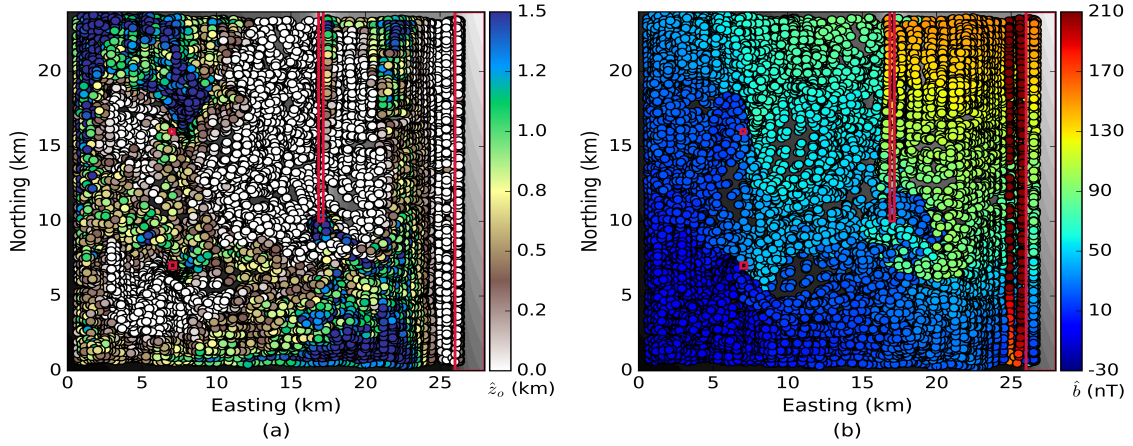


Figure 3.2: Euler deconvolution estimates for all moving-data windows, red polygons outline the sources. (a) Source-position estimates. (b) Base level-estimates.

depth to the top of the vertical intrusion at 0.627 km. In this test, the amplitude of the magnetic anomaly due to source P2 (vertical intrusion) is the smallest one; however, our methodology was able to retrieve the depth of the top of the source P2 correctly. Finally, Figure 3.3d shows the tightest cluster of the source-position estimates over the source P3 by assuming the  $SI = 3$ . The mean of depth estimates over this source retrieves the depth to the center of the spherical source at 1.057 km.

Figure 3.4 shows the results of the proposed methodology where the base-level estimates (shown in colored circles) are displayed over the map of the magnetic anomaly (Figure 3.1d), shown in grayscale. Figure 3.4a-d shows the estimates assuming the  $SI = 0, 1, 2$  and  $3$ , respectively. As shown in Melo and Barbosa (2018), the base-level estimates in Figure 3.4a have the amplitude amplified because the  $SI$  is zero. As in the source-position estimates shown in Figure 3.3, the tightest cluster of base level estimates defines the correct  $SI$ .

The definition of the correct  $SI$  in the results shown in Figure 3.3 and 3.4 is possible because of the tightest clustering of the source-position and base-level estimates. The nonlinear base level does not affect the proposed methodology because we select the reliable Euler deconvolution estimates throughout the moving-data windows with the largest standard deviations of the vertical derivatives of the data (Figure 3.1d). Thus, we selected only the moving-data windows where a factual source is present.

### 3.4.2 Test 2 - Nearby sources with remanence

Figure 3.5a shows a total-field anomaly generated by the sources P2 and P3 from the previous test (Figure 3.1); the black polygons outline the horizontal projections of the simulated sources. Here, the distance between these sources is 1.5 km and the

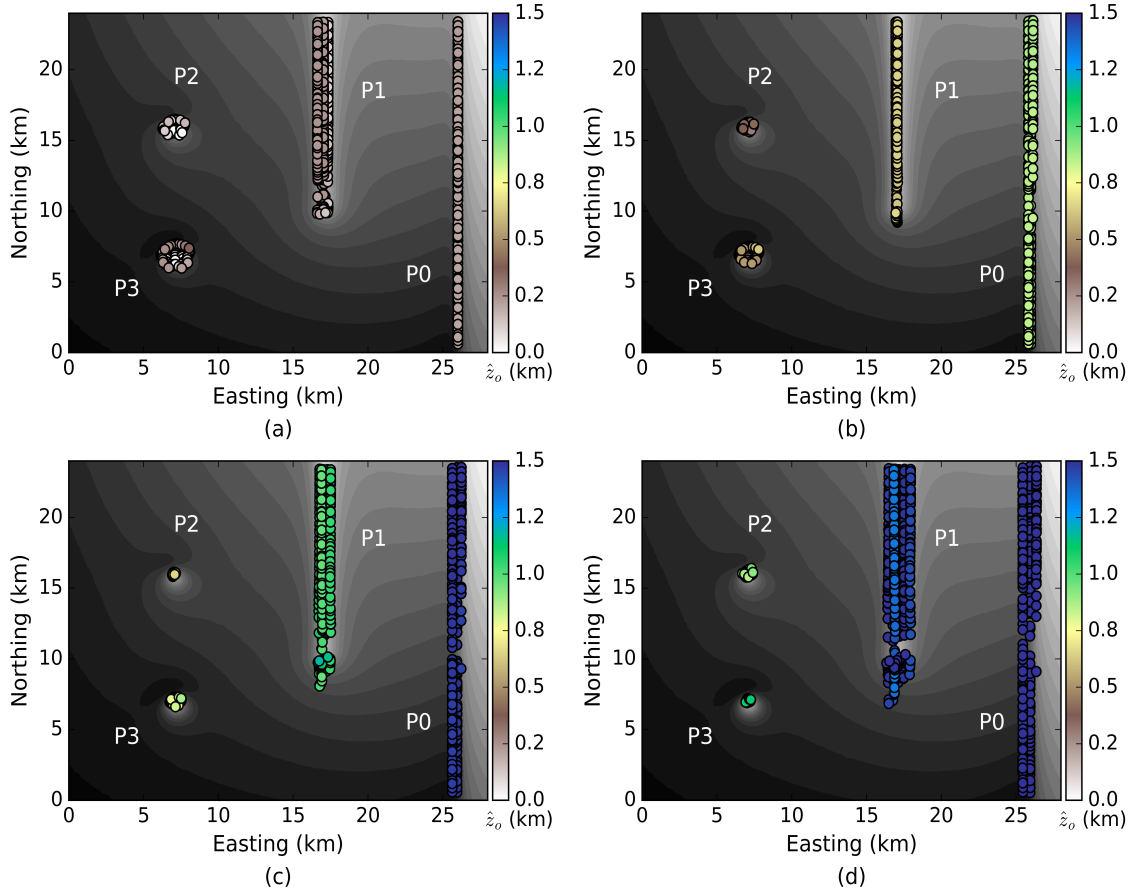


Figure 3.3: Euler deconvolution source-position estimates (colored circles) over the total-field anomaly (grayscale). Source-position estimates assuming (a)  $SI = 0$  (b)  $SI = 1$ , (c)  $SI = 2$  and (d)  $SI = 3$ . The selected Euler estimates are the ones that are obtained by using the data windows with the largest standard deviations of the vertical derivatives of the total-field anomaly.

source P2 has remanent magnetization with inclination  $i = -60^\circ$ , in the opposite direction of both the source P3 and the geomagnetic field ( $i = 60^\circ$  as shown in Figure 3.1b). We simulated a survey on a regular grid of  $60 \times 50$  observation points in the  $x$ - and  $y$ -directions with grid spacing of 0.2 km along both directions. The survey height is simulated at  $z = -0.1$  km. The simulated total-field anomaly was corrupted with pseudorandom Gaussian noise with zero mean and standard deviation of 0.1% of the maxima absolute amplitude of the data.

At first glance, it may not seem possible to define if one source between the peaks or more sources generated the anomaly in Figure 3.5a. Hansen and Suciú (2002) treated the case of a local field induced by two bodies. However, according to the authors all sources must have the same structural index, which is not the case in this test. Therefore, their method is not suitable in this scenario. In the following, we will show that our methodology succeeds. We run Euler deconvolution with a moving-data window of  $5 \times 5$  points and keep the best 51 estimates (2% of the

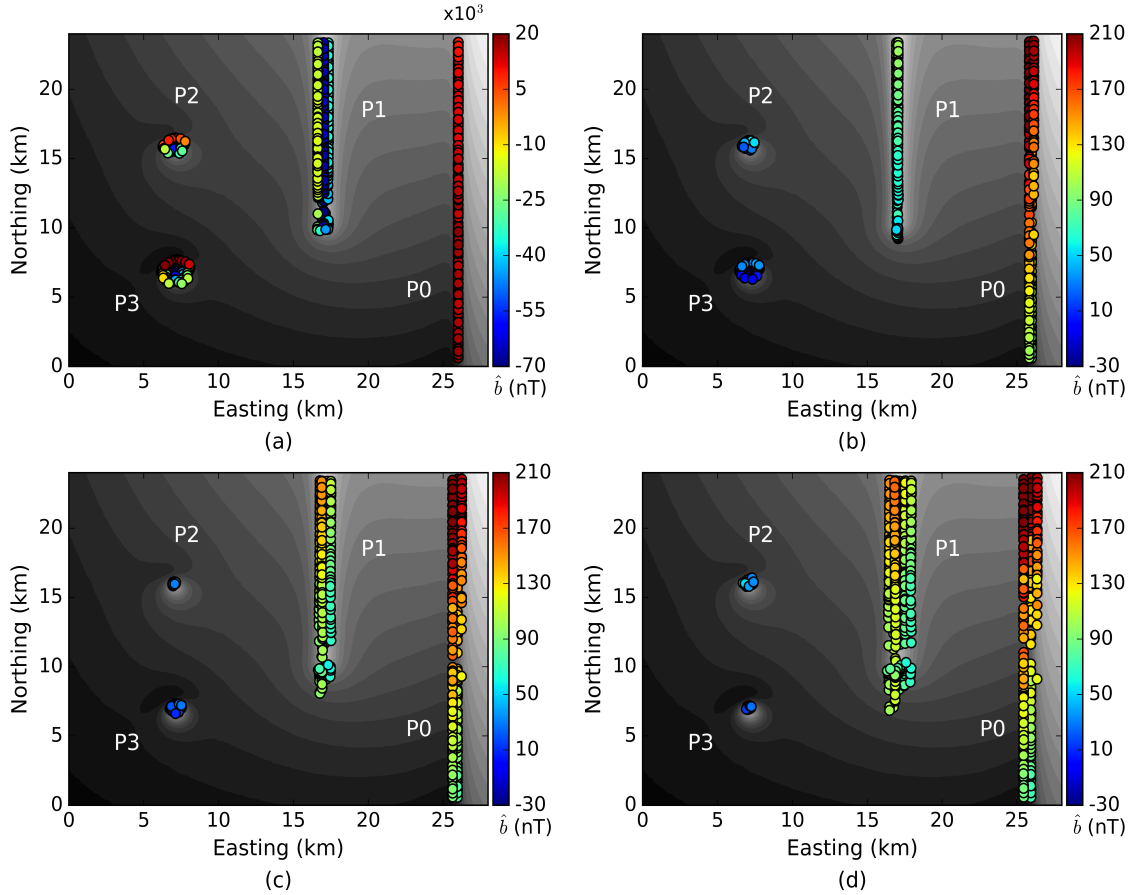


Figure 3.4: Euler deconvolution base level estimates (colored circles) over the total-field anomaly (grayscale). Base-level estimates assuming (a)  $SI = 0$  (b)  $SI = 1$ , (c)  $SI = 2$  and (d)  $SI = 3$ . The selected Euler estimates are the ones that are obtained by using the data windows with the largest standard deviations of the vertical derivatives of the total-field anomaly.

solutions). In this test, the size of the window is smaller than the one used in the previous test because the sources are closer.

Figure 3.5b-d shows the source-position and base-level estimates assuming the  $SI = 2$  and  $3$ , respectively. The estimates (shown in colored circles) are displayed over the map of the magnetic anomaly (Figure 3.5a), shown in grayscale. Comparing source-position estimates in Figure 3.5b (using  $SI = 2$ ) with the estimates in Figure 3.5d (using  $SI = 3$ ) and the base-level estimates in Figure 3.5c (using  $SI = 2$ ) with the estimates in Figure 3.5e (using  $SI = 3$ ), we confirm that the tightest cluster of Euler solutions for the source P2 occurs when we use the  $SI = 2$  (Figure 3.5b and 3.5d) and the tightest cluster of Euler solutions for the source P3 occurs when we use the  $SI = 3$  (Figure 3.5d and 3.5e). Both tight clusters of the estimates of the source positions and base levels are able to define the correct SIs. The mean of depth estimates of the cluster of the Euler solutions shown in Figure 3.5b correctly defines the depth to the top of the source P2 (prism) at 0.658 km. While the mean of depth

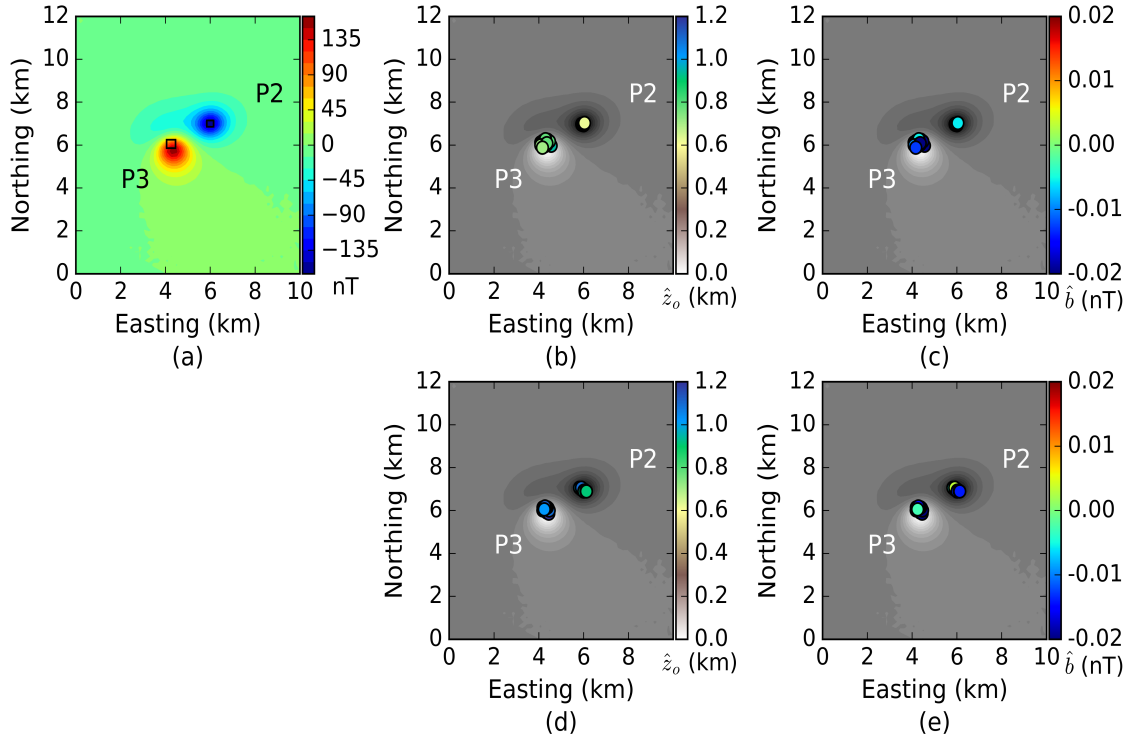


Figure 3.5: Total-field anomaly and Euler deconvolution estimates (colored circles). (a) Noise-corrupted total-field anomaly (grayscale) with the horizontal projection of the sources P2 and P3 outlined by the black polygons. Euler estimates assuming the SI = 2 (b) source-position and (c) base level. Euler estimates assuming SI = 3 (d) source position and (e) base level. The selected Euler estimates are the ones that are obtained by using the data windows with the largest standard deviations of the vertical derivatives of the total-field anomaly.

estimates of the tight cluster of the Euler solutions shown in Figure 3.5b correctly defines the depth to the center of the source P3 (spherical source) at 1.028 km. Hence, in this synthetic test simulating interfering magnetic anomalies, caused by geologic sources closely separated from each other by short distances and remanently magnetized, our methodology determines the SI and the depth estimates correctly.

### 3.4.3 Test 3 - Reliable estimates via other quantities?

We propose the use of the vertical derivatives of the total-field anomaly to define reliable solutions in Euler deconvolution and show its performance in the previous tests. However, one question that rises is why the horizontal derivatives of the total-field anomaly or total-field anomaly cannot be used to define the reliable solutions instead of the vertical derivatives?

First, let us analyze the performance of the horizontal derivatives in defining reliable solutions. In order to perform this analyze we will revisit the "Test 1 - Distinct SIs and strong nonlinear magnetic base level". Figure 3.6a-3.6c shows the

derivatives of the total-field anomaly (Figure 3.1d) in the  $x$ -,  $y$ - and  $z$ -directions, respectively. The black polygons outline the horizontal projections of the sources shown in Figure 3.1a. Figure 3.6a shows the derivative of the total-field anomaly along the  $x$ -direction, notice that the source P0 is not defined on this derivative, this happens because this source is elongated in the  $x$ -direction. Furthermore, this derivative defines only the edge of the source P1 and not all its extension. On the other hand, the sources P2 and P3 are defined. Figure 3.6b shows the derivative of the total-field anomaly along the  $y$ -direction, this derivative defines all the sources P0-P3. However, the definition of all sources is only possible because the sources P0 and P1 are elongated perpendicular to the direction of this derivative. Finally, Figure 3.6c shows the derivative of the total-field anomaly along the  $z$ -direction, this is the derivative used in this work, and it defines all the sources P0-P3.

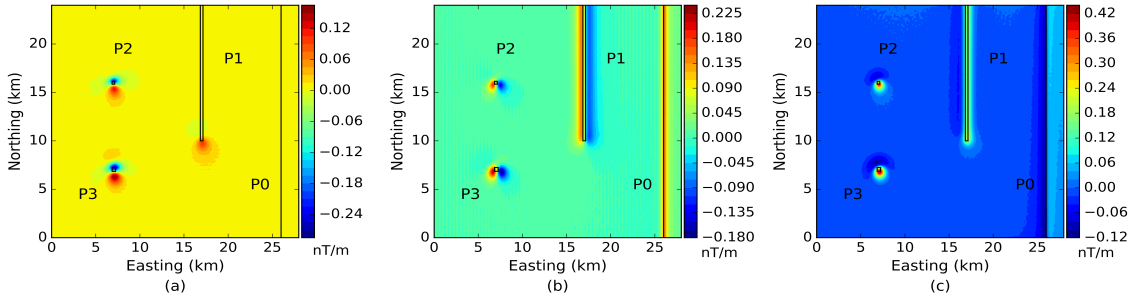


Figure 3.6: Derivatives of the total-field anomaly shown in Figure 3.1d. Derivatives in the (a)  $x$ -, (b)  $y$ - and (c)  $z$ -directions. The black polygons outline the horizontal projections of the sources shown in Figure 3.1a.

We run Euler deconvolution in the total-field anomaly (Figure 3.1d) with the same parameters of the first test, where the moving-data window has  $9 \times 9$  points and we kept the best 8% of the solutions. However, in this test, the best estimates were selected throughout the largest standard deviations of the derivatives in the  $x$ -direction. Figure 3.7a-3.7d shows the Euler deconvolution estimates assuming the  $SI = 0, 1, 2$  and  $3$ , respectively. As expected, because we have used the derivatives in the  $x$ -direction (Figure 3.6a), none of the estimates are defining the source P0, only spurious solutions appear close to this source. In addition, the estimates do not cluster over the source P1, in fact, is not possible to distinguish a tight cluster between the  $SI = 0$  (Figure 3.7a) and the  $SI = 1$  (Figure 3.7b). Notice that contrary to the source-position estimates by using the vertical derivatives (Figure 3.3) the estimates via the derivatives in the  $x$ -direction do not cluster over the sources P2 (Figure 3.7c) and P3 (Figure 3.7c). The spray of these estimates has a direct connection to the use of the derivatives in the  $x$ -direction (Figure 3.6a).

In order to define the correct  $SI$  for the sources P2 and P3 based on the derivatives along the  $x$ -direction (Figure 3.7) we need to keep less solutions. Therefore, we

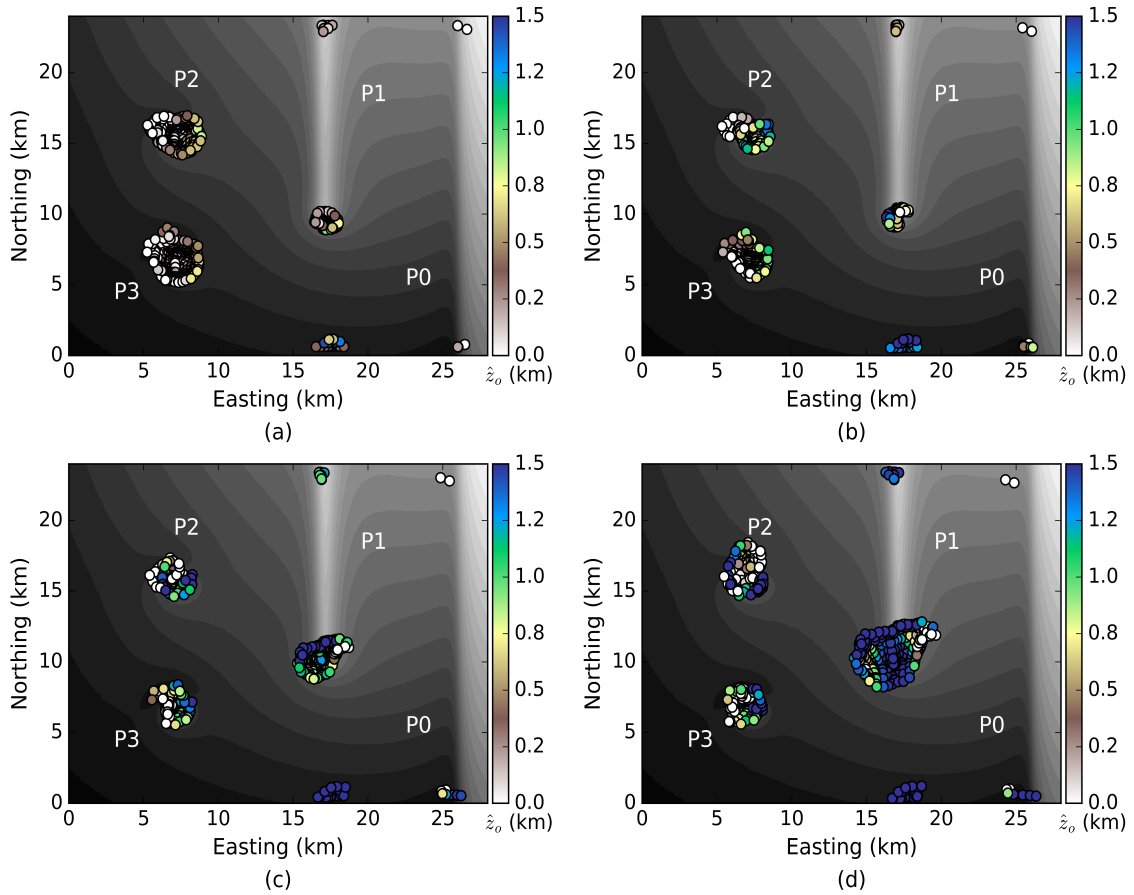


Figure 3.7: Euler deconvolution source-position estimates (colored circles) plotted over the total-field anomaly (grayscale). The selected Euler estimates are the ones that are obtained by using the data windows with the largest standard deviations of the  $x$ -derivatives of the total-field anomaly. Source-position estimates assuming (a)  $SI = 0$  (b)  $SI = 1$ , (c)  $SI = 2$  and (d)  $SI = 3$ . The best 8% of the solutions were kept.

run Euler deconvolution and keep the best 2% of the solutions. Figure 3.8a-3.8c shows the source-position estimates for the SI 1, 2 and 3, respectively. Keeping less solutions make the estimates vanish over the source P1 for all SIs. The solutions cluster over the correct source for the SI 2 (Figure 3.8b) and the SI 3 (Figure 3.8c). However, only a few solutions are shown and this might be not useful in scenarios with more sources, as in this example.

Similarly to the derivative of the total-field anomaly along the  $x$ -direction, the derivative along the  $y$ -direction fails in defining sources elongated in the  $y$ -direction (not shown). Therefore, we must conclude that the use of the horizontal derivatives of the total-field anomaly to select the reliable solution, instead the vertical derivative, fails.

Now, let us analyze the performance of the total-field anomaly in defining reliable solutions. In order to perform this analyze we will revisit the "Test 2 - Nearby

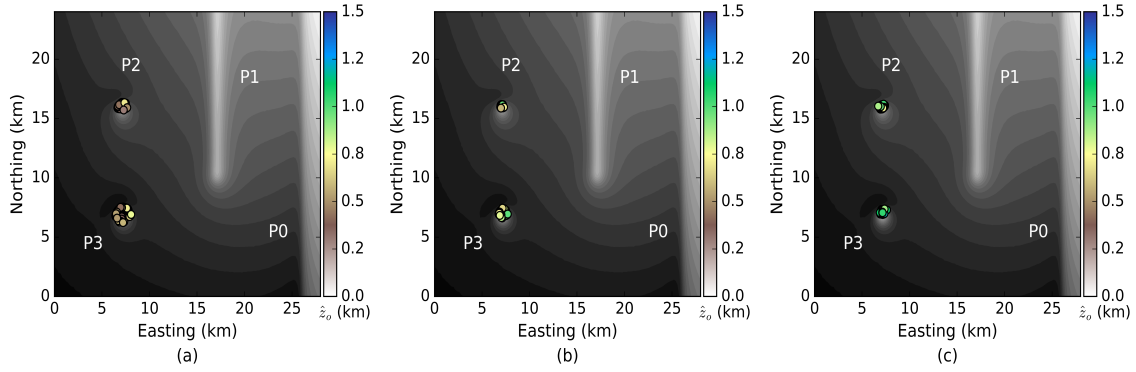


Figure 3.8: Euler deconvolution source-position estimates (colored circles) defined over the total-field anomaly (grayscale). The selected Euler estimates are the ones that are obtained by using the data windows with the largest standard deviations of the  $x$ -derivatives of the total-field anomaly. Source-position estimates assuming (a)  $SI = 1$ , (b)  $SI = 2$  and (c)  $SI = 3$ . The best 2% of the solutions were kept.

sources with remanence”. To this end, we performed two tests, in the first, we used a moving-data window of  $5 \times 5$  grid points (the same as in Test 2) and in the second test, we used a moving-data window of  $3 \times 3$  grid points.

Figure 3.9a and 3.9b shows the Euler deconvolution estimates of the total-field anomaly shown in Figure 3.5 based on the largest standard deviations of the total-field anomaly with  $SI = 2$  and  $3$ , respectively, accepting 2% of the solutions. Notice that all solutions are over the anomaly suggesting a single source; therefore we cannot distinguish the two sources (P2 and P3). So, in an attempt to define the correct  $SI$  we accepted fewer solutions. Figure 3.9c and 3.9d shows the Euler deconvolution estimates assuming the  $SI = 2$  and  $3$ , respectively, accepting 1.5% of the solutions. Notice that the solutions over the source P2 are clustered for both  $SI = 2$  (Figure 3.9c) and  $SI = 3$  (Figure 3.9d), so it is not possible to define the correct  $SI$  for this source. In addition, over the source P3 there is a spread of solutions in Figure 3.9c and 3.9d and is also not possible to define the correct  $SI$  for this source.

In the second test, we used a moving-data window of  $3 \times 3$  grid points in order to check if a small size window would define correctly the sources. Figure 3.10a and 3.10b shows the Euler deconvolution estimates from the total-field anomaly shown in Figure 3.5 based on the largest standard deviations of the total-field anomaly with  $SI = 2$  and  $3$ , respectively, accepting 1.5% of the solutions. Notice that the solutions over the sources are not clustered in any of these cases, so we cannot take conclusions about the correct  $SI$ . One might think that the acceptance of fewer solutions would better determine the correct  $SI$ . Under this perspective, Figure 3.10c and 3.10d shows the Euler deconvolution estimates based on the largest standard deviations of the total-field anomaly with  $SI = 2$  and  $3$ , respectively, accepting 1% of the solutions. In both results (Figure 3.10c and 3.10d), the solutions are clustered

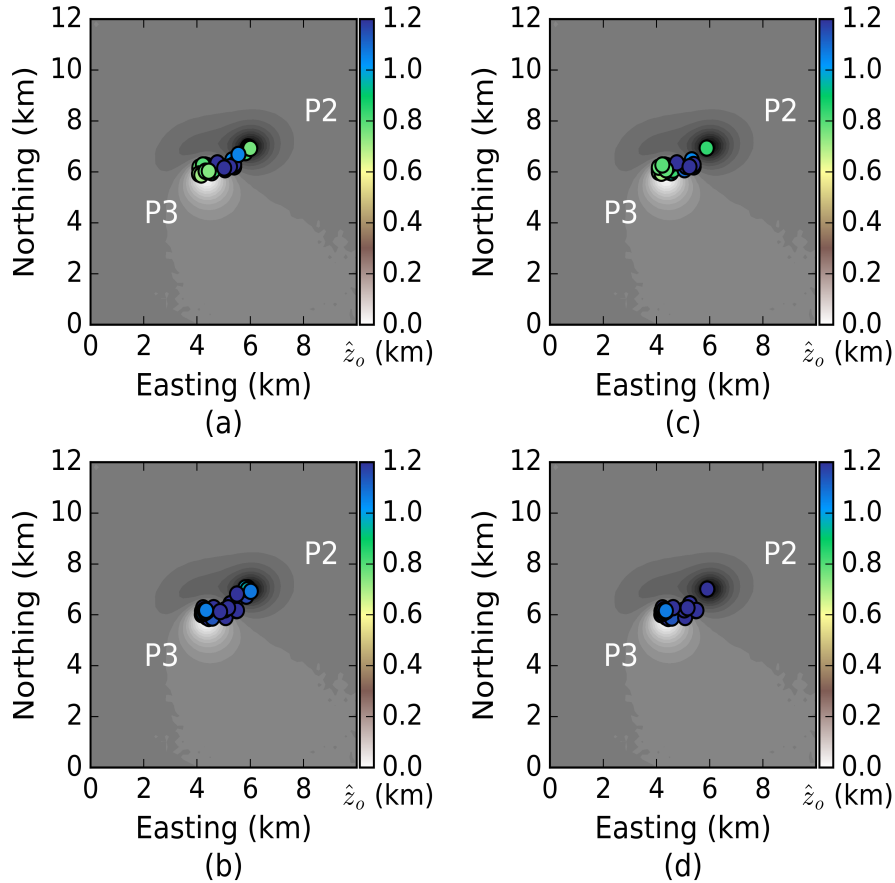


Figure 3.9: Euler deconvolution source-position estimates (colored circles) defined over the total-field anomaly (grayscale). The selected Euler estimates are the ones obtained by using the data windows of  $5 \times 5$  points with the largest standard deviations of the total-field anomaly. Source-position estimates accepting 2% of the solutions assuming (a)  $SI = 2$  and (b)  $SI = 3$ . Source-position estimates accepting 1.5% of the solutions assuming (c)  $SI = 2$  and (d)  $SI = 3$ .

over the source P2 so, we cannot determine the correct SI. The solutions over the source P3 are also clustered in both results (Figure 3.10c and 3.10d), so once more is not possible to take conclusions about the correct SI.

The decay with distance of the vertical derivative of the total-field anomaly is higher than the decay of the total-field anomaly. This fact combined with the moving-data window scheme makes the vertical derivative of the total-field anomaly a useful tool in distinguishing multiple geologic bodies giving rise to interfering anomalies. In interpreting magnetic data with interfering anomalies produced by multiple geologic bodies, the vertical derivative ability to distinguish multiple and closely separated bodies is greater than the ability of the total-field anomaly itself. This is the reason why the total-field anomaly does not work to select the reliable Euler deconvolution estimates on cases of interfering anomalies.

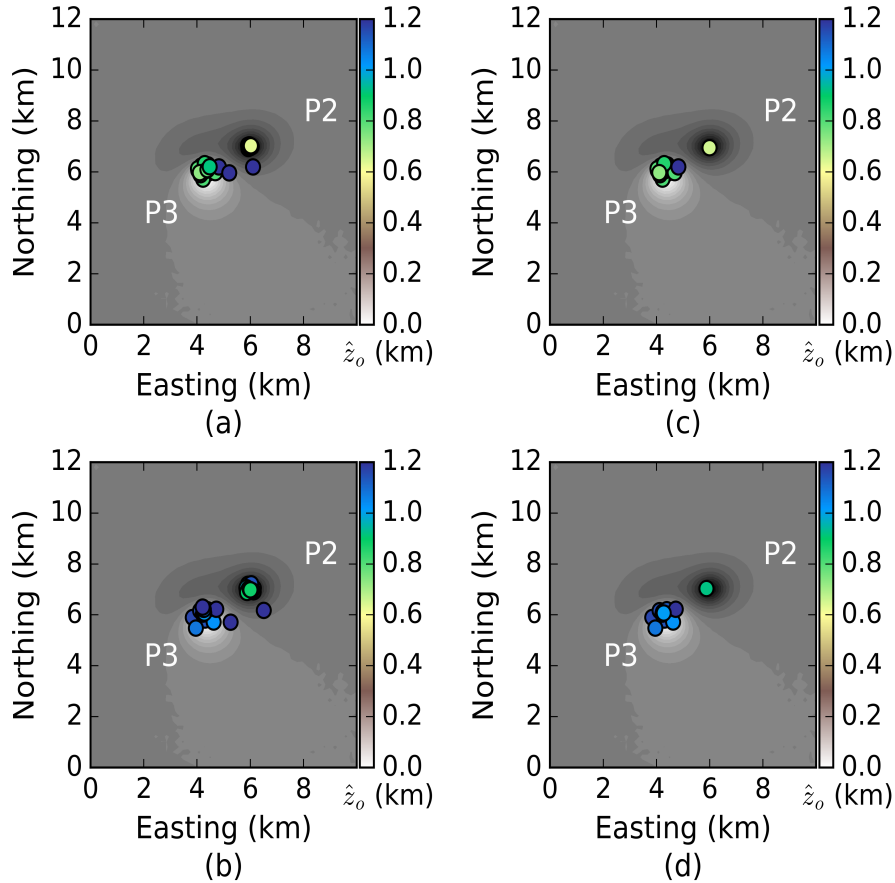


Figure 3.10: Euler deconvolution source-position estimates (colored circles) plotted over the total-field anomaly (grayscale). The selected Euler estimates are the ones obtained by using the data windows of  $3 \times 3$  points with the largest standard deviations of the total-field anomaly. Source-position estimates accepting 1.5% of the solutions assuming (a)  $SI = 2$  and (b)  $SI = 3$ . Source-position estimates accepting 1% of the solutions assuming (c)  $SI = 2$  and (d)  $SI = 3$ .

### 3.5 Application to real data set

The Santa Catarina state in southern Brazil is characterized by the occurrence of several alkaline and alkaline-carbonatitic bodies of Early to Late Cretaceous age. The Anitápolis alkaline-carbonatite complex (132 Ma) is a small intrusion in the Late Proterozoic Dom Feliciano mobile belt (Scheibe et al., 2005). The complex shows a concentric zonation consisting of phlogopite clinopyroxenites and apatite-biotite-magnetite clinopyroxenites surrounded by ijolites and nepheline syenites that intrude Late Proterozoic granitic-gneissic rocks. A dyke like carbonatitic core of about ten square meters crops out at the center of the complex in contact with phlogopite clinopyroxenites (Comin-Chiaramonti et al., 2005). The phosphate deposit of Anitápolis produces large amounts of phosphate fertilizers. Apatite is the only mineral worth exploiting economically, and it corresponds to reserves of 206.5 Mt, according to fresh rocks distribution from boreholes (Biondi, 2005). The study area

(blue dot in Figure 3.11a) has a near surface well-known geology; however, the shape and the depth of the magnetized source that gives rise to the Anitápolis anomaly are unknown.

The aeromagnetic data (yellow polygon in Figure 3.11a) were acquired between 2009 and 2011 (CPRM, 2011) over the southeastern and southern Brazil. The flight lines in the north–south direction were acquired every 0.5 km, the tie lines were acquired every 10 km and the flight height was approximately constant at  $z = -0.1$  km. The data set in the study area is gridded every 0.125 km in the  $x$ - and  $y$ -directions, and has 145 points northing and 121 points easting. Figure 3.11b shows the Anitápolis anomaly over the study area (blue dot in Figure 3.11a); this anomaly is approximately located at  $27^{\circ}48'$  south and  $49^{\circ}5'$  west (WGS84).

We run Euler deconvolution with a moving-data window size of  $7 \times 7$  grid points. Figure 3.11c and 3.11d shows source-position and base-level estimates assuming the  $SI = 2$  and Figure 3.11d and 3.11e show source-position and base-level estimates assuming the  $SI = 3$ , respectively. We kept the best 31 estimates (0.2% of the solutions) associate with the largest standard deviations of the vertical derivatives of the total-field anomaly. A single source is identifiable by the tightest cluster of the solutions assuming  $SI = 2$  (Figure 3.11c and 3.11d). The mean of depth estimates assuming the  $SI = 2$  is equal to 0.677 km. Recall, that the  $SI = 2$  defines a plug source, so these estimated values define the depth to the top of a plug intrusion.

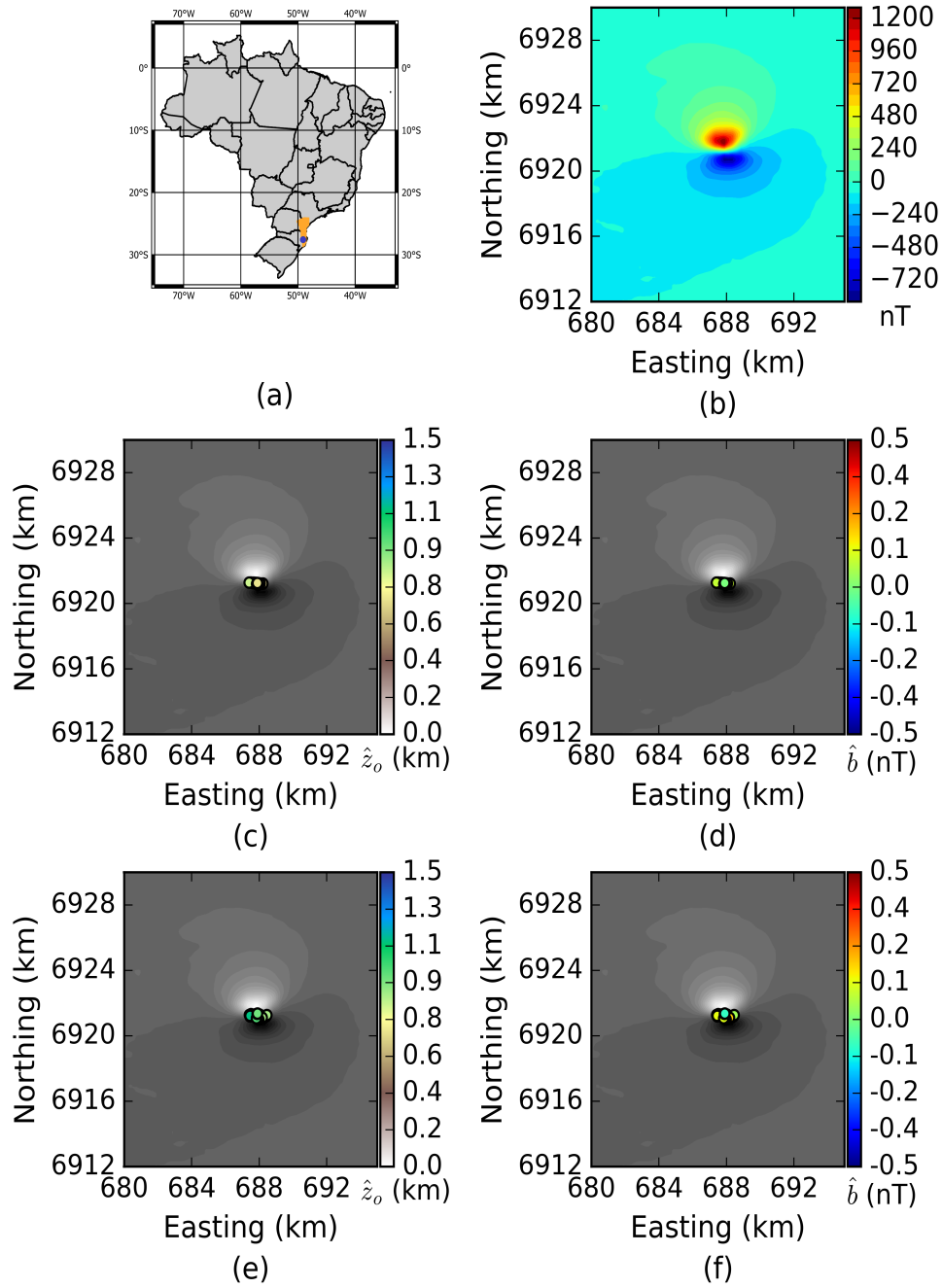


Figure 3.11: Real data application - Euler deconvolution estimates. (a) Aeromagnetic survey in yellow and the study area in blue dot. (b) Anitápolis total-field anomaly. Euler estimates assuming the  $SI = 2$  (c) source positions and (d) base levels. Euler estimates assuming the  $SI = 3$  (e) source positions and (f) base levels. The selected Euler estimates are the ones that are obtained by using the data windows with the largest standard deviations of the vertical derivatives of the total-field anomaly.

## 3.6 Final Considerations

We proposed a novel methodology to compute reliable Euler deconvolution estimates. The spray of solutions is reduced selecting the moving-data windows with the largest standard deviations of the vertical derivatives of the total-field anomaly. The tightest cluster of source-position or base-level estimates plotted on the selected moving-data windows with distinct SI defines the optimum SI. Finally, we defined the depth of the sources with the mean the selected depth estimates. The robustness of the methodology was proved on synthetic tests where the anomalies were subject to interfering anomalies. In these tests, our method was able to determine the correct SI and to estimate the correct depth of the sources. Application to aeromagnetic data from the southern Brazil leads us to infer that one vertical plug intrusion generates the Anitápolis anomaly. This work is a step further in the selection of reliable estimates in Euler deconvolution and in the understanding of the behavior of the base-level estimates and how they can be used in the determination of the structural index (shape of the magnetic source). Our methodology to define reliable Euler solutions can be used with other discrimination techniques in any of the modification of the Euler deconvolution such as the extended Euler deconvolution. The reliable Euler solutions can be combined in inversion methods to produce a detailed definition of the anomalous source of the Anitápolis anomaly.

# Chapter 4

## Correct structural index in Euler deconvolution via base-level estimates

This chapter has been published "Melo, F. F., Barbosa, V. C., 2018. Correct structural index in Euler deconvolution via base-level estimates. *Geophysics* 83 (6), J87-J98". This paper was nominated by the Geophysics editors to be highlighted in "Geophysics Bright Spots". "Nature of the geologic source for potential field data", *The Leading Edge*, 37, Issue 12, 2018.

### 4.1 Summary

In most applications, Euler deconvolution aims to define the nature (type) of the geologic source (i.e., the structural index, SI) and its depth position. However, Euler deconvolution also estimates the horizontal positions of the sources and the base level of the magnetic anomaly. To determine the correct SI, most authors take advantage of the clustering of depth estimates. We have analyzed the Euler's equation to show that random variables contaminating the magnetic observations and its gradients affect the base-level estimates if, and only if, the SI is not assumed correctly. Grounded on this theoretical analysis and assuming a set of tentative structural indices (SIs), we have proposed a new criterion for determining the correct SI by means of the minimum standard deviation of base-level estimates. We performed synthetic tests simulating multiples magnetic sources with different SIs. To produce mid and strongly interfering synthetic magnetic anomalies, we added constant and nonlinear backgrounds to the anomalies and approximated the simulated sources laterally. If the magnetic anomalies are weakly interfering, the minima standard deviations either of the depth or base-level estimates can be used to determine the

correct SI. However, if the magnetic anomalies are strongly interfering only the minimum standard deviation of the base-level estimates can determine the SI correctly. These tests also show that Euler deconvolution does not require that the magnetic data be corrected for the regional fields (e.g., IGRF – International Geomagnetic Reference Field). Tests on real data from part of Goiás Alkaline Province, Brazil, confirm the potential of the minimum standard deviation of base-level estimates in determining the SIs of the sources by applying Euler deconvolution either to total-field measurements or total-field anomaly (corrected for IGRF). Our result suggests three plug intrusions giving rise to Diorama anomaly and dipole-like sources yielding Arenópolis and Montes Claros de Goiás anomalies.

## 4.2 Introduction

Euler deconvolution is one of the most popular techniques in potential field methods. It is a semi-automatic interpretation technique proposed by Reid et al. (1990) that allows fast processing of large datasets. The technique is grounded on Euler equation for homogeneous functions (Hood, 1965; Thompson, 1982). Euler deconvolution relates potential-field measurements, their gradients and a given integer number called the structural index (SI), which in turn depends on the nature (type) of the geologic source (Henderson and Zietz, 1948; Reid and Thurston, 2014; Smellie, 1956; Stavrev and Reid, 2007; Uieda et al., 2014). Usually, Euler deconvolution assumes a tentative SI and estimates four parameters: base level, horizontal and vertical positions of an isolated and single-point geologic source.

One practical hindrance for Euler deconvolution is the need to assume a tentative SI. The SI can only be an integer number (Mas-Colell et al., 1995; Ravat, 1996; Reid et al., 2014; Reid and Thurston, 2014; Thurston, 2010); otherwise, the index changes under the variation of the source-observation vector (Ravat, 1996; Reid and Thurston, 2014). Assuming some tentative SI values, Thompson (1982) noticed the relation between the use of the correct SI and a tight clustering in depth estimates, and used this behavior to determine the correct SI. Others authors, like Reid et al. (1990), followed this approach to propose slight modifications of Thompson (1982) criterion for determining the SI. Following this approach other authors proposed other techniques (Mikhailov et al., 2003; Ugalde and Morris, 2010) to treat the spreading of depth solutions and define the correct SI. Silva et al. (2001) showed that the criterion for determining the SI as the tentative value producing the smallest solution scattering, that includes the depth estimates, is theoretically sound but can fail in practice because of data noise. On the other hand, Barbosa et al. (1999) showed that the minimum correlation between base-level estimates and profile magnetic data in modulus gives the correct SI and Melo et al. (2013) used this

approach in gridded magnetic data. Alternatively, some authors modified Euler deconvolution and develop new techniques solving for SI and depth simultaneously (Fedi et al., 2009; Hsu, 2002; Keating and Pilkington, 2004; Mushayandebvu et al., 2001; Nabighian and Hansen, 2001; Stavrev, 1997) or deal with non-ideal sources (Fedi et al., 2015; Florio and Fedi, 2014; Stavrev and Reid, 2007, 2010; Thurston, 2010).

According to Thompson (1982), it is hard to detect the anomalous field by itself so he introduced the concept of base level which is a constant background value of the field inside an evaluating data window. He stressed that the base level can be generated, for example, by interfering anomalies or regional field. By handling the Euler deconvolution mathematically, some authors assumed a constant and non-null base level (Barbosa et al., 1999; Hsu, 2002; Reid et al., 1990; Thompson, 1982), a null base level (Silva and Barbosa, 2003), linear base levels (Gerovska and Araúzo-Bravo, 2003; Stavrev, 1997) and nonlinear base levels (Dewangan et al., 2007; Pasteka, 2006). Although the base level is estimated by the Euler deconvolution, few authors have used this estimate in practice. Fairhead et al. (1994), for example, estimated and removed the base level the anomaly in order to estimate focused Euler solutions in a two-step approach. Reid and Thurston (2014) stated that is possible to determine the correct SI using the base-level estimates; however, these estimates were only used by Barbosa et al. (1999) and Melo et al. (2013) to this end in a straightforward way.

In this paper, we show that realizations of random variables contaminating the potential-field measurements affect the base-level estimates if, and only if, the SI is not assumed correctly. Hence, we propose a criterion to determine the SI based on the standard deviation of the estimates of base-level using different values of SI. The optimal SI is one that produces the smallest standard deviation of the base-level estimates. In our tests, we noticed that even for strongly interfering anomalies, the minimum standard deviation of base-level estimates gives the correct SI; however, it fails if the anomaly is not produced by a single-point source. We also confirmed that anomalies generate nonlinear base-level estimates even when the true simulated base level added to the data is constant or null. This happens not only because of the interfering anomalies but also because base-level estimates have a nonlinear pattern that mimics the potential-field anomalies even inside the current moving-data window. Here, we show that anomaly interference produced by the presence of nonlinear background and nearby anomalies makes the criterion for determining the correct SI based on the smallest scattering of depth estimates unfeasible. Conversely, we certify the good performance of our approach in determining the correct SI by assuming null, constant and nonlinear backgrounds that were added to the data. We applied our methodology to total-field measurements and total-field anomaly (corrected for

IGRF) from a portion of Goiás Alkaline Province located in central Brazil, and the numerical results are similar. Both applications determine the same SI and mean depths for the geologic sources in the study area. These results show that the prior remove of the IGRF is not mandatory in Euler deconvolution application. The estimated base level reveals a nonlinear pattern that mimics the pattern of the anomaly. The Diorama anomaly is the main target alkaline intrusion to be interpreted in the study area. Our result suggests that Diorama anomaly is generated by more than one plug intrusion. We also expanded our interpretation using Euler deconvolution to other anomalies in the study area (e.g., Arenópolis, Montes Claros de Goiás and Córrego dos Bois). However, some of the results may not be reliable because the magnetic sources may not behave as single-point sources violating the concept of Euler homogeneity.

### 4.3 Methodology

Euler deconvolution is defined by Reid et al. (1990):

$$\hat{x}_o \frac{\partial h_i}{\partial x} + \hat{y}_o \frac{\partial h_i}{\partial y} + \hat{z}_o \frac{\partial h_i}{\partial z} + \eta \hat{b} = x_i \frac{\partial h_i}{\partial x} + y_i \frac{\partial h_i}{\partial y} + z_i \frac{\partial h_i}{\partial z} + \eta h_i, \quad (4.1)$$

where  $\eta$  is the SI,  $b$  is a base level or background value,  $x_o$ ,  $y_o$  and  $z_o$  are source positions,  $x$ ,  $y$  and  $z$  are the observation position,  $h = h(x, y, z)$  is the total-field anomaly and  $\frac{\partial h_i}{\partial x}$ ,  $\frac{\partial h_i}{\partial y}$  and  $\frac{\partial h_i}{\partial z}$  are the gradients of anomaly with respect to the variables  $x$ ,  $y$  and  $z$ , respectively. We use a tentative SI in equation 4.1, in a moving-data window scheme, and the estimated parameters are  $\hat{x}_o$  and  $\hat{y}_o$  (horizontal positions of the source),  $\hat{z}_o$  (vertical position of the source) and  $\hat{b}$  (base level). The caret (hat) denotes an estimated quantity. Details about Euler deconvolution are available in the Appendix A.

Here, we extend and modify the criterion of Barbosa et al. (1999) for determining the best SI for gridded data. By applying Euler deconvolution with a moving-data window scheme and the correct SI,  $\eta$ , over a region that encompass the anomaly, we obtain the estimated parameters  $\hat{x}_o^k$ ,  $\hat{y}_o^k$ ,  $\hat{z}_o^k$  and  $\hat{b}^k$  for the  $k$ th position of the moving-data window. Hence, equation 4.1 can be written as:

$$\hat{x}_o^k \frac{\partial h_i^k}{\partial x} + \hat{y}_o^k \frac{\partial h_i^k}{\partial y} + \hat{z}_o^k \frac{\partial h_i^k}{\partial z} + \eta \hat{b}^k = x_i^k \frac{\partial h_i^k}{\partial x} + y_i^k \frac{\partial h_i^k}{\partial y} + z_i^k \frac{\partial h_i^k}{\partial z} + \eta h_i^k, \quad (4.2)$$

where the subscript  $i$  is related to the  $i$ th observation position  $(x_i, y_i, z_i)$  inside the  $k$ th moving-data window.

By assuming a wrong SI,  $\mu$ , we obtain the estimates  $\hat{x}_o^k$ ,  $\hat{y}_o^k$ ,  $\hat{z}_o^k$  and  $\hat{b}^k$  and

equation 4.1 can be rewritten as:

$$\hat{x}_o^k \frac{\partial h_i^k}{\partial x} + \hat{y}_o^k \frac{\partial h_i^k}{\partial y} + \hat{z}_o^k \frac{\partial h_i^k}{\partial z} + \mu \hat{b}^k = x_o^k \frac{\partial h_i^k}{\partial x} + y_o^k \frac{\partial h_i^k}{\partial y} + z_o^k \frac{\partial h_i^k}{\partial z} + \mu h_i^k. \quad (4.3)$$

By subtracting equation 4.3 from equation 4.2 and rearranging the terms, we obtain:

$$(\hat{x}_o^k - x_o^k) \frac{\partial h_i^k}{\partial x} + (\hat{y}_o^k - y_o^k) \frac{\partial h_i^k}{\partial y} + (\hat{z}_o^k - z_o^k) \frac{\partial h_i^k}{\partial z} + \mu \hat{b}^k - \eta b^k = (\mu - \eta) h_i^k. \quad (4.4)$$

Let's assume that additive random noises  $\varepsilon_1$ ,  $\varepsilon_2$ ,  $\varepsilon_3$  and  $\varepsilon_4$  contaminate, respectively, the terms  $\frac{\partial h_i^k}{\partial x}$ ,  $\frac{\partial h_i^k}{\partial y}$ ,  $\frac{\partial h_i^k}{\partial z}$  and  $h_i^k$ . Accordingly equation 4.4 can be rewritten as:

$$(\hat{x}_o^k - x_o^k) \left[ \frac{\partial h_i^k}{\partial x} + \varepsilon_1 \right] + (\hat{y}_o^k - y_o^k) \left[ \frac{\partial h_i^k}{\partial y} + \varepsilon_2 \right] + (\hat{z}_o^k - z_o^k) \left[ \frac{\partial h_i^k}{\partial z} + \varepsilon_3 \right] + \mu \hat{b}^k - \eta b^k = (\mu - \eta) [h_i^k + \varepsilon_4]. \quad (4.5)$$

As shown by Silva and Barbosa (2003), the estimates of the horizontal source positions are not affected by the choice of the SI, because these estimates do not depend on the SI. Hence, even assuming a wrong structural index,  $\mu$ , we have that  $\hat{x}_o^k = x_o^k$  and  $\hat{y}_o^k = y_o^k$ . As result, the first and second terms on the left-hand side of equation 4.5 are very close to zero. Thus, rearranging equation 4.5, we have:

$$\hat{b}^k = \frac{\eta b^k}{\mu} + \frac{(\hat{z}_o^k - z_o^k)}{\mu} \left[ \frac{\partial h_i^k}{\partial z} + \varepsilon_3 \right] + \left( 1 - \frac{\eta}{\mu} \right) [h_i^k + \varepsilon_4]. \quad (4.6)$$

Notice that the second and third terms on the right-hand side of equation 4.6 are corrupted with random variables ( $\varepsilon_3$  and  $\varepsilon_4$ ). Hence, estimates of base level can be affected by uncertainties in the total field data  $h_i^k$  and its vertical gradient  $\frac{\partial h_i^k}{\partial z}$ . However, random variables do not affect base-level estimates if, and only if, we assume the correct structural index (i.e., if  $\mu = \eta$ ). Only in this case, we have  $\hat{z}_o^k = z_o^k$  and the second and third terms on the right-hand side of equation 4.6 are negligible. Therefore, equation 4.6 shows that the presence of random noise will affect the base-level estimates if we do not correctly assume the structural index (i.e., if  $\mu \neq \eta$ ). In this case, the terms  $\frac{(\hat{z}_o^k - z_o^k)}{\mu} \left[ \frac{\partial h_i^k}{\partial z} + \varepsilon_3 \right]$  and  $\left( 1 - \frac{\eta}{\mu} \right) [h_i^k + \varepsilon_4]$  in equation 4.6 will be non-negligible.

Let us assume a set of  $L$  moving-data windows and thus a set of  $L$  base-level estimates using either a wrong SI ( $\hat{b}^1, \dots, \hat{b}^L$ ) or the correct SI ( $b^1, \dots, b^L$ ). Thus, the standard deviation of base-level estimates obtained over the anomaly will be minimum only if the SI is correctly assumed (i.e.,  $\mu = \eta$ ).

In our approach we provisionally assigned a tentative SI. For each SI, we estimate

four parameters  $\hat{x}_o$ ,  $\hat{y}_o$ ,  $\hat{z}_o$  and  $\hat{b}$  which are plotted against the central position of the moving-data window forming maps as proposed by Silva and Barbosa (2003). The maps of  $\hat{x}_o$  and  $\hat{y}_o$  form plateaus over the anomaly (Melo et al., 2013; Silva and Barbosa, 2003); however plateaus may not be clearly formed for depth ( $\hat{z}_o$ ) and base level ( $\hat{b}$ ) estimates in the presence of interfering anomalies. By assuming any tentative SI, we propose to evaluate the standard deviation of base-level estimates over an area delineated by depth estimates that lie over the anomaly. In the presence of interfering anomalies, we delineate this area using the approach of Melo et al. (2013) which is defined through the intersection of mapped plateaus on horizontal estimates ( $\hat{x}_o$  and  $\hat{y}_o$ ). The minimum standard deviation of a set of estimated base levels will define the correct SI. With the knowledge of the correct structural index the average of depth estimates in the area previously selected can give one solution per anomaly (Melo et al., 2013). Figure 4.1 is a flow chart that shows the steps of our methodology

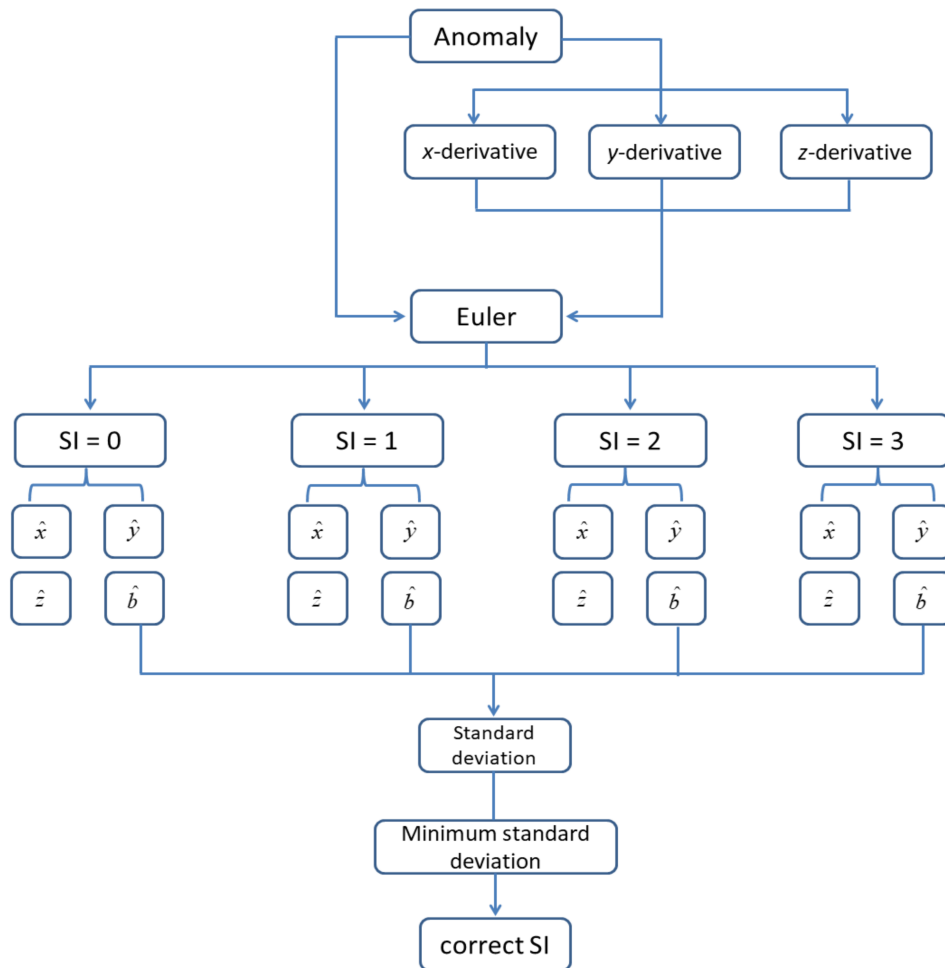


Figure 4.1: Flow chart of the methodology to define the correct structural index (SI) in Euler deconvolution via base-level estimates.

All the software developed and used in this chapter is open source and was

made available in 2019. The algorithm was developed in Python language and it is compatible with both Python 2.7 and Python 3.7. The package with instructions is available at <https://github.com/ffigura/Euler-deconvolution-plateau>.

## 4.4 Synthetic tests

We applied our methodology to different geological scenarios where the magnetic sources are approximated by simple geometry (Hinze et al., 2013). However, these simple geometries represent real geological bodies such as: a semi-infinite prism simulating a fault (SI = 0), a line of poles simulating a vertical sheet or thin dike (SI=1), a point pole simulating a vertical cylinder or a plug/pipe (SI=2) and a dipole simulating a sphere or a magmatic chamber/Unexploded Ordnance (UXO) (SI=3).

In the first test, we assume a null background value and an isolated anomaly. In the second test, we assume a constant background value, simulating the magnetic field on a region. In the third test, we simulate a nonlinear background; this background can be generated by a strong magnetic source or poor definition of the IGRF. Finally, in the last test, we simulate both constant and nonlinear backgrounds and approximate the sources distance, generating strongly interfering anomalies more close to real-world scenario.

In all tests, except in the first where SI 0 is not used, we run Euler deconvolution using tentative SIs of 0, 1, 2 and 3. The moving-data window size is  $9 \times 9$  grid points, following the recommendation of Reid et al. (2014) about window size, grid space and depth of investigation. Throughout these tests, values of declination, inclination and total-field intensity were based on Chulliat et al. (2014), and derivatives were calculated in Fourier domain (Blakely, 1996). All anomalies were corrupted with pseudorandom Gaussian noise with zero mean and standard deviation of 0.01 nT. We assume a coordinate system with  $x$ -axis increasing north,  $y$ -axis increasing east and  $z$ -axis increasing down, in all tests the surveys were simulated on plane  $z = 0$  km. In the first test, the survey was simulated in a grid of  $240 \times 200$  observation points in the north and east directions, with a regular equal space of 0.1 km in both north and east directions. In this test we simulate the the values of declination and inclination of the geomagnetic field at the city of Dakar - Senegal (Chulliat et al., 2014). In all other tests, values of declination, inclination and total-field intensity simulated the field in the city of Phoenix - USA (Chulliat et al., 2014). Also, the surveys were simulated in a grid of  $325 \times 300$  observation points in the north and east directions, with a regular equal space of 0.2 km in both north and east directions.

#### 4.4.1 Test 1 - Null background

Figure 4.2 shows the synthetic noise-corrupted total-field anomaly produced by a single pole ( $SI = 2$ ). The simulated geomagnetic field has inclination of  $7^\circ$  and declination of  $-7^\circ$ , with null intensity. The single pole is located at  $x_o = 12$  km,  $y_o = 10$  km,  $z_o = 0.5$  km and has magnetization intensity of 1 A/m.

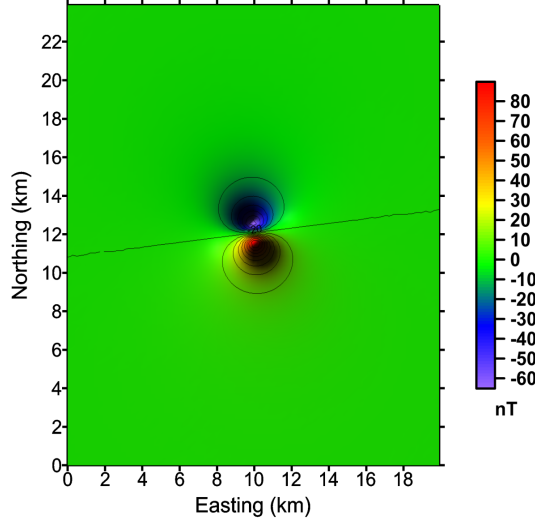


Figure 4.2: total-field anomaly generated by a single pole ( $SI = 2$ ). The simulated magnetic field has inclination of  $7^\circ$  and declination of  $-7^\circ$ .

Figure 4.3a-c shows depth estimates from Euler deconvolution assuming SIs 1, 2 and 3, respectively. For depth estimates, plateaus of solutions appear only when the correct SI is used (Figure 4.3b). When the wrong SI is used, depth estimates do not define a plateau; rather they form a cavity (Figure 4.3a) or a prominence (Figure 4.3c).

Figure 4.3d-f shows base-level estimates from Euler deconvolution assuming SIs 1, 2 and 3, respectively. Base-level estimates exhibit the same behavior of depth estimates, for isolated sources. Plateaus of solutions appear only when the correct SI is used (Figure 4.3e). When the wrong SI is used, base-level estimates do not define a plateau; rather they form a cavity (Figure 4.3d) or a prominence (Figure 4.3f). Besides that, notice that base-level estimates mimics the total-field anomaly shape (Figure 4.2).

Based on the identified plateau in the plot of depth estimates shown in Figure 4.3b, we selected we selected all the depth and base-level estimates that fall in this area. With these estimates, we calculated the standard deviation in order to define the correct SI. Table 4.1 confirms that the minima standard deviations either of the depth or base-level estimates define the correct SI, highlighted in boldface, for the case of isolated sources.

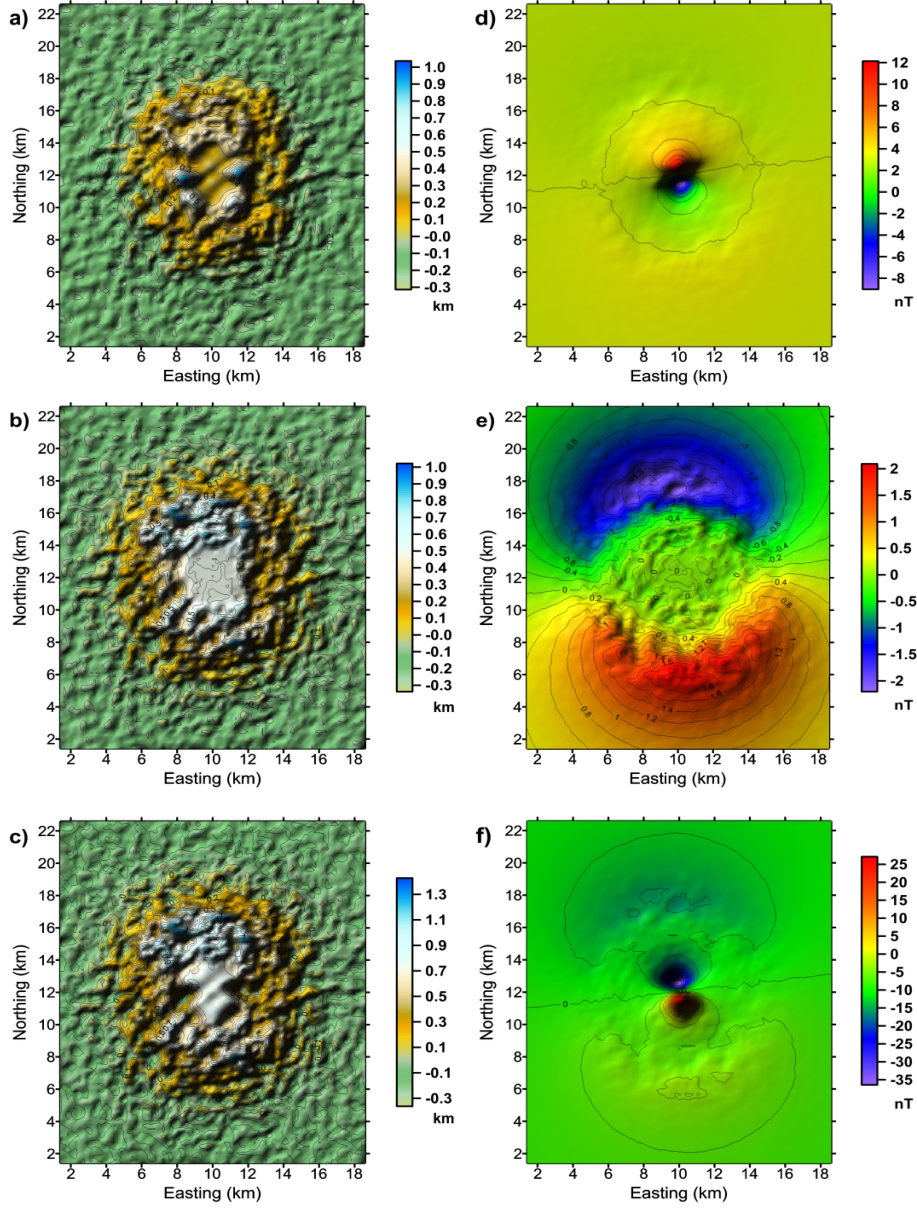


Figure 4.3: Euler deconvolution estimates for the single pole with null base level. Depth estimates (a) - (c) and base-level estimates (d) - (f) assuming SI: 1, 2 and 3, respectively. Estimates assuming the correct SI generates a plateau of correct values, while cavities or buldges appear when the wrong SI is used.

Table 4.1: Standard deviation of depth and base-level estimates for the null background. Minimum standard deviation for each source is highlighted in boldface.

	$\hat{z}_o$	$\hat{b}$
SI = 1	0.121	15.706
SI = 2	<b>0.006</b>	<b>0.031</b>
SI = 3	0.124	5.239

### 4.4.2 Test 2 - Constant background

Figure 4.4 shows the synthetic noise-corrupted total-field anomaly produced by semi-infinite prism (SI = 0), a line of 1220 poles (SI = 1) separated by grid distance, a single pole (SI = 2) and a sphere (SI = 3) of radius 0.5 km. The simulated geomagnetic field has inclination of  $59^\circ$  and declination of  $10^\circ$  with constant intensity of 47500 nT. The prism with magnetization intensity of 1 A/m extends from infinitely along the  $x$ -direction, from 10 km to the infinite along the  $y$ -direction and in depth from 0.5 km to infinite. The line of poles is located at  $y_o = 45$  km and  $z_o = 1.8$  km and extends from  $x_o = 15$  to infinite, each pole has magnetization intensity of 0.5 A/m. The single pole is located at  $x_o = 45$  km,  $y_o = 25$  km and  $z_o = 2$  km, with magnetization intensity of 5 A/m. Finally, the sphere is magnetized uniformly, with magnetization intensity of 5 A/m, magnetization inclination of  $9^\circ$  and declination of  $-32^\circ$ . The sphere is located at  $x_o = 25$  km,  $y_o = 25$  km and  $z_o = 1.5$  km. Although applied to a constant base level, the results show in this test was also applied to a null base level (not shown), i.e., magnetic anomaly corrected for IGRF. By inspecting Figure 4.4 qualitatively, we can note a subtle distortion of the data isovalue curves that indicates weakly interfering anomalies due to the proximity between the simulated sources.

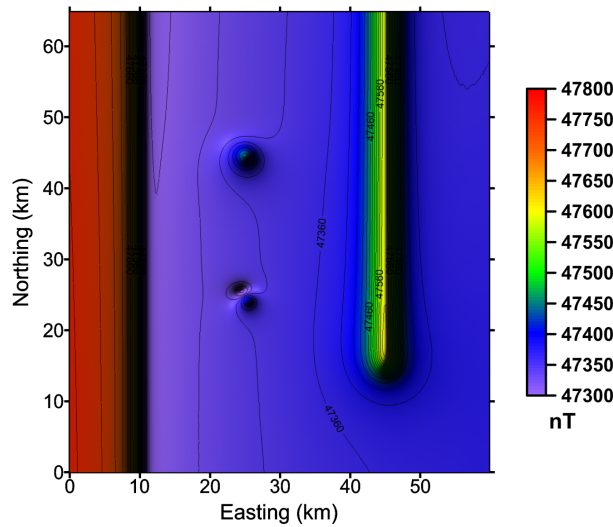


Figure 4.4: (a) Noise-corrupted total-field anomaly generated by a semi-infinite prism (SI = 0), a line of poles (SI = 1), a single pole (SI = 2) and a sphere (SI = 3). The simulated geomagnetic field with intensity of 47500 nT has inclination of  $59^\circ$  and declination of  $10^\circ$ . The dipole is magnetized uniformly, with magnetization intensity of 5 A/m, magnetization inclination of  $9^\circ$  and declination of  $-32^\circ$ , while the other sources are magnetized by induction only.

Figure 4.5a-d shows depth estimates from Euler deconvolution assuming SIs of 0, 1, 2 and 3, respectively. For depth estimates, plateaus of solutions appear only when the correct SI is used, for non or weakly interfering anomalies. When the

wrong SI is used, depth estimates do not define a plateau; rather they form a cavity or a bulge. A plateau of depth estimates is clearly evident in Figure 4.5a over the edge of the prism because the correct  $SI = 0$  is used; whereas in Figure 4.5b-d we can see buldges for the depth estimates of this source. The same occurs for the line of poles, single pole and dipole, with respect to their correct structural indices.

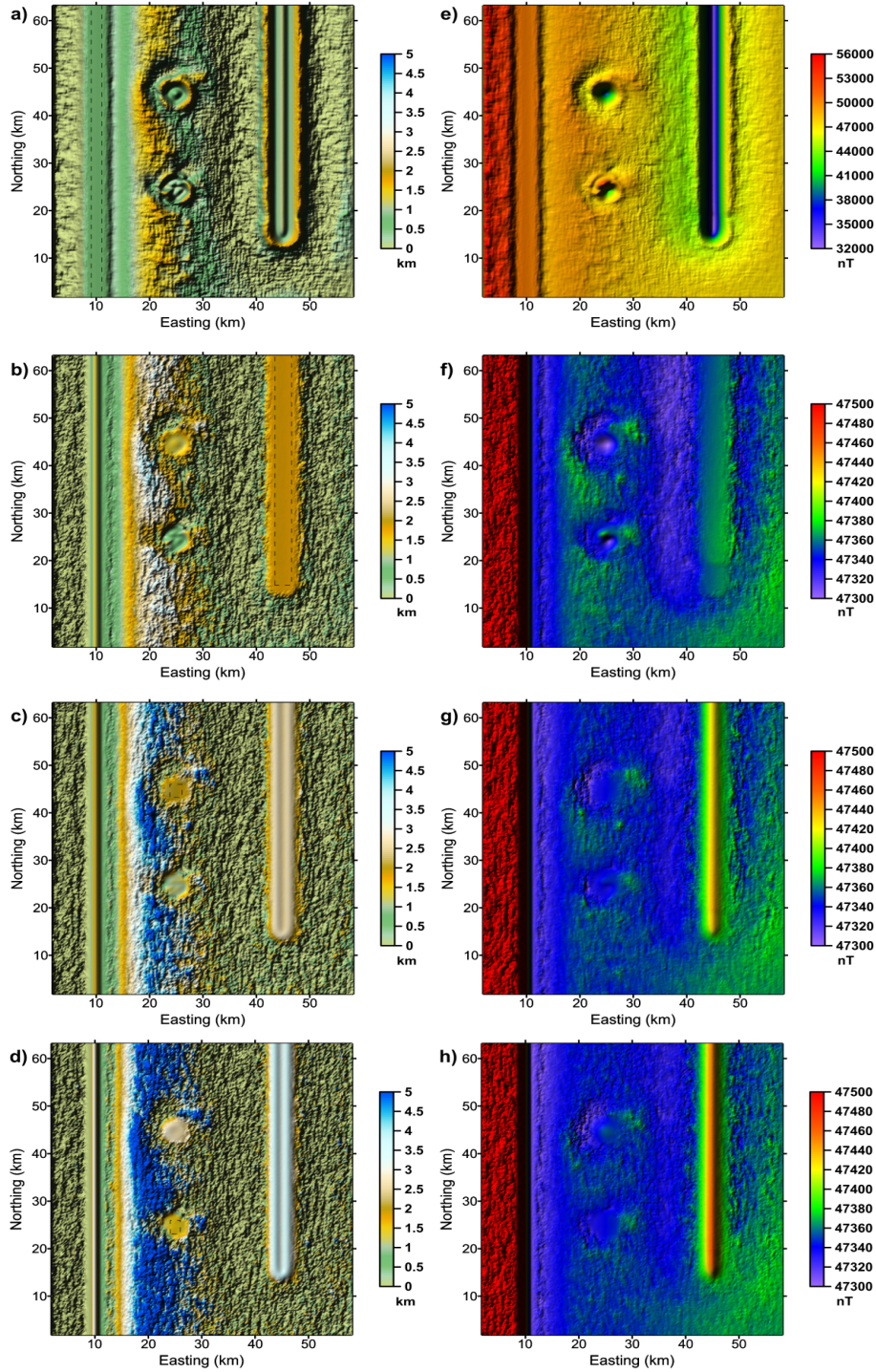


Figure 4.5: Euler deconvolution estimates for anomaly with constant background (Figure 4.4). Depth (a) – (d) and base-level (e) – (h) estimates assuming SIs of 0, 1, 2 and 3, respectively. Depth estimates assuming the correct SI form a plateau of correct values, whereas estimates using the wrong SI do not form a plateau and have wrong values. Base-level estimates using the correct SI has minimum values compared to the ones estimates using the wrong SI. For each source, the plateau areas, where the methodology is applied, are outlined by dashed rectangles. These areas were defined by the plateaus on the depth estimates shown in a – d.

Table 4.2 shows standard deviations of depth estimates using four different SI values for each source and considering this test with a constant background. The minimum standard deviation for each source (highlighted in boldface) occurs if the correct SI is used.

Table 4.2: Standard deviation of depth estimates for the constant background. Minimum standard deviation for each source is highlighted boldface.

Source	SI = 0	SI = 1	SI = 2	SI = 3
<b>Prism</b>	<b>0.002</b>	0.277	0.555	0.8334
<b>Line of poles</b>	0.109	<b>0.017</b>	0.113	0.222
<b>Monopole</b>	0.095	0.057	<b>0.051</b>	0.086
<b>Dipole</b>	0.102	0.068	0.041	<b>0.037</b>

Figure 4.5e-h shows base-level estimates from Euler deconvolution assuming SIs of 0, 1, 2 and 3. These estimates fall at the same positions as depth estimates (Figure 4.5a-d) and exhibit the same pattern when the correct SI is used. Specifically, a plateau of constant base-level estimates is exhibited when the correct SI is used while cavities or bulges appear when the wrong SI is used. Thus, comparing at the same source position using different SI is easy to identify that the smallest variation of the base-level estimates at source location indicates the correct SI. Additionally, notice that the base-level estimates mimic the magnetic anomaly (Figure 4.4).

Table 4.3 shows standard deviations of base-level estimates using four different SI values for each simulated source. The minimum standard deviation for each source is in boldface. As expected, for each source, the standard deviation is minimum using the correct SI. Once the correct SI is defined, the mean depth calculated in the same area gives the correct depth of the sources.

Table 4.3: Standard deviation of base-level estimates for the constant background. Minimum standard deviation for each source is highlighted boldface.

Source	SI = 0	SI = 1	SI = 2	SI = 3
<b>Prism</b>	<b>86.436</b>	124.742	124.949	125.040
<b>Line of poles</b>	2959.662	<b>4.451</b>	15.550	20.226
<b>Monopole</b>	1869.891	9.835	<b>2.989</b>	4.169
<b>Dipole</b>	3244.212	21.072	5.074	<b>1.970</b>

This test shows that the minima standard deviations calculated either from base-level estimates (Table 4.3) or from depth estimates (Table 4.2) are able to correctly define SI in the presence of constant background. Also, this test shows that a constant background does not interfere in Euler deconvolution estimates. Therefore, the

magnetic data does not need to be previously corrected for IGRF to the application of Euler deconvolution.

### 4.4.3 Test 3 - Nonlinear background

Here, we generated a synthetic total-field anomaly (Figure 4.6a) produced by the same sources and magnetization direction of the previous test. In this test, a simulated nonlinear background (Figure 4.6b) is added to the original data (Figure 4.6a) by:

$$b(x_i, y_i) = \frac{(x_i + 10) \times (y_i + 10)}{30}, \quad (4.7)$$

giving rise the noise-corrupted magnetic anomaly (Figure 4.6c) to be used in Euler deconvolution. In equation 4.7, the subscript  $i$  is related to the  $i$ th position of the observation  $(x_i, y_i)$ . This polynomial can simulate a regional field, a strongly interfering anomaly or a poor definition of the IGRF. Notice that the nonlinear background (Figure 4.6b) has high values of the same order of magnitude as the original data (Figure 4.6a) producing strongly interfering anomalies, as displayed in Figure 4.6c.

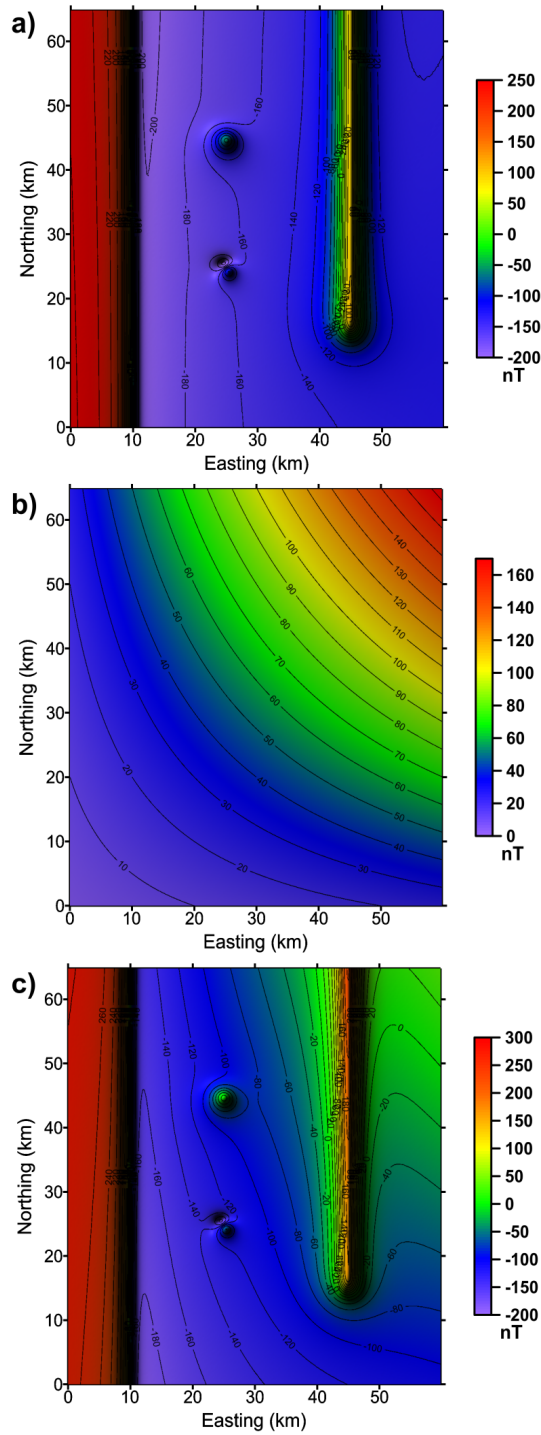


Figure 4.6: Nonlinear background anomaly. (a) Noise-corrupted total-field anomaly generated by a prism ( $SI = 0$ ), a line of poles ( $SI = 1$ ), a single pole ( $SI = 2$ ) and a dipole ( $SI = 3$ ). The simulated geomagnetic field with intensity of 47500 nT has inclination of  $59^\circ$  and declination of  $10^\circ$ . The dipole is magnetized uniformly, with magnetization intensity of 5 A/m, magnetization inclination of  $9^\circ$  and declination of  $-32^\circ$ , while the other sources are magnetized by induction only. (b) Nonlinear polynomial to simulate a regional field. (c) Noise-corrupted magnetic anomaly obtained by adding the total-field anomaly shown in a to the nonlinear polynomial shown in b.

In Figure 4.7a-d we can see depth estimates from Euler deconvolution assuming SIs of 0, 1, 2 and 3, respectively. Figure 4.7b shows the plateau on the depth estimates over the line of poles with a too slight difference compared with Figure 4.5b. In contrast, by comparing Figure 4.7c-d with Figure 4.5c-d, we notice that depth estimates of the correct sources for SIs 2 and 3 do not form plateaus and show different shapes. This means that the depth estimates are affected by the presence of a nonlinear background. In a case like this, where the plateaus are not clearly defined on depth estimates (Figure 4.7c-d) we use the procedure of (Melo et al., 2013) which delineates the plateau areas, in order to determine in our work the best SI, through the intersections of the plateaus formed on the horizontal estimates ( $\hat{x}_o$  and  $\hat{y}_o$ ).

Figure 4.8 shows the horizontal estimates using Euler deconvolution applied to noise-corrupted magnetic anomaly 4.6c in the presence of nonlinear background. Figure 4.8a-d shows the estimates  $\hat{x}_o$  and Figure 4.8e-h shows the estimates  $\hat{y}_o$  assuming SIs of 0, 1, 2 and 3, respectively. Because, these horizontal estimates ( $\hat{x}_o$  and  $\hat{y}_o$ ) are less sensitive to interfering anomalies than estimates  $\hat{z}_o$ , the intersections of the plateaus of  $\hat{x}_o$  (Figure 4.8a-d) and (Figure 4.8e-h) are used in this test to delineate the areas (shown in dashed rectangles in Figure 4.7a-d), which are used to determine the best SI.

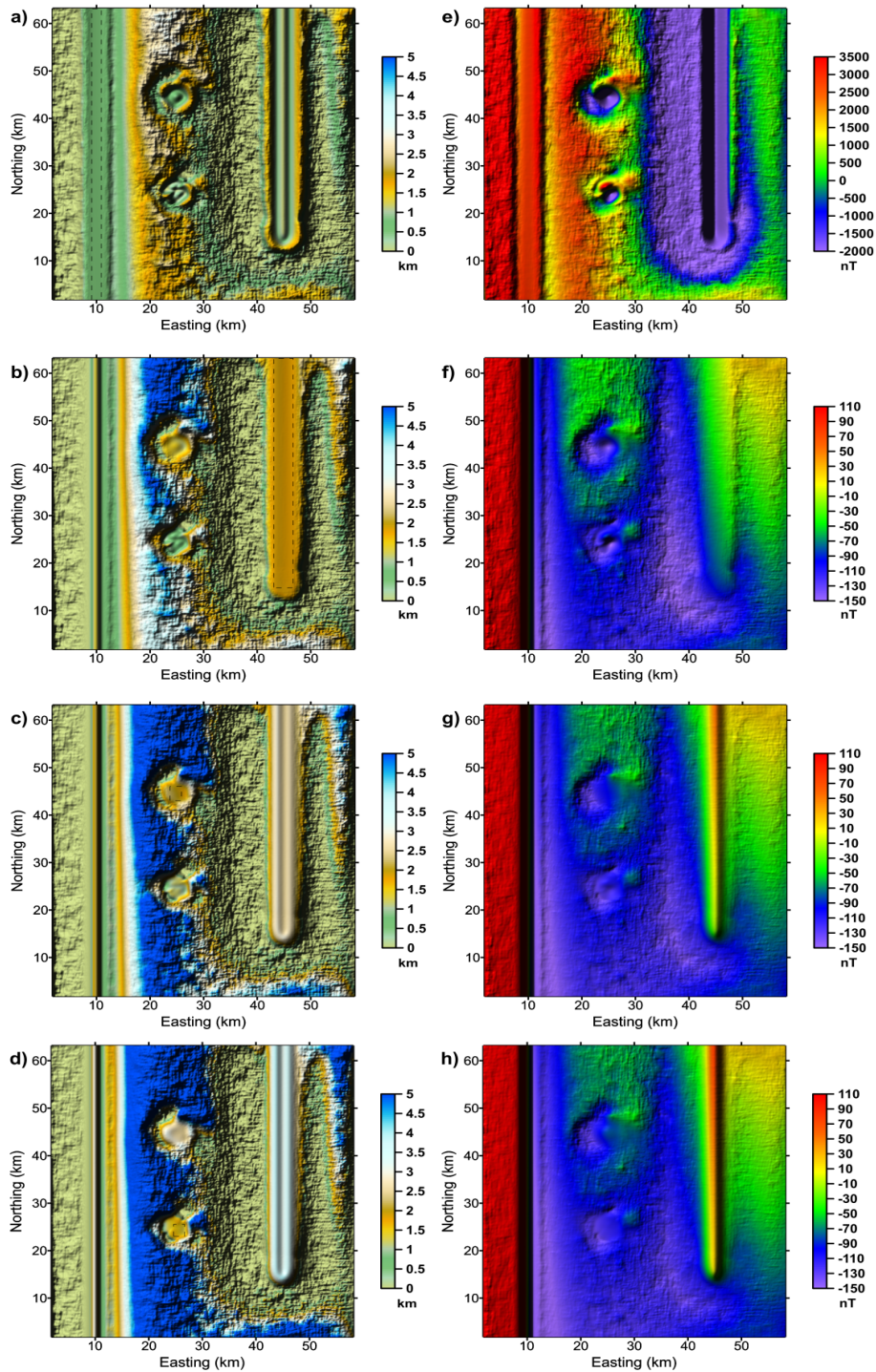


Figure 4.7: Euler deconvolution estimates for anomaly with nonlinear background. Depth (a) – (d) and base-level (e) – (h) estimates assuming SIs of 0, 1, 2 and 3, respectively. For each source, the plateau areas, where the methodology is applied, are outlined by dashed rectangles. These areas were defined by the intersection of mapped plateaus on horizontal estimates.

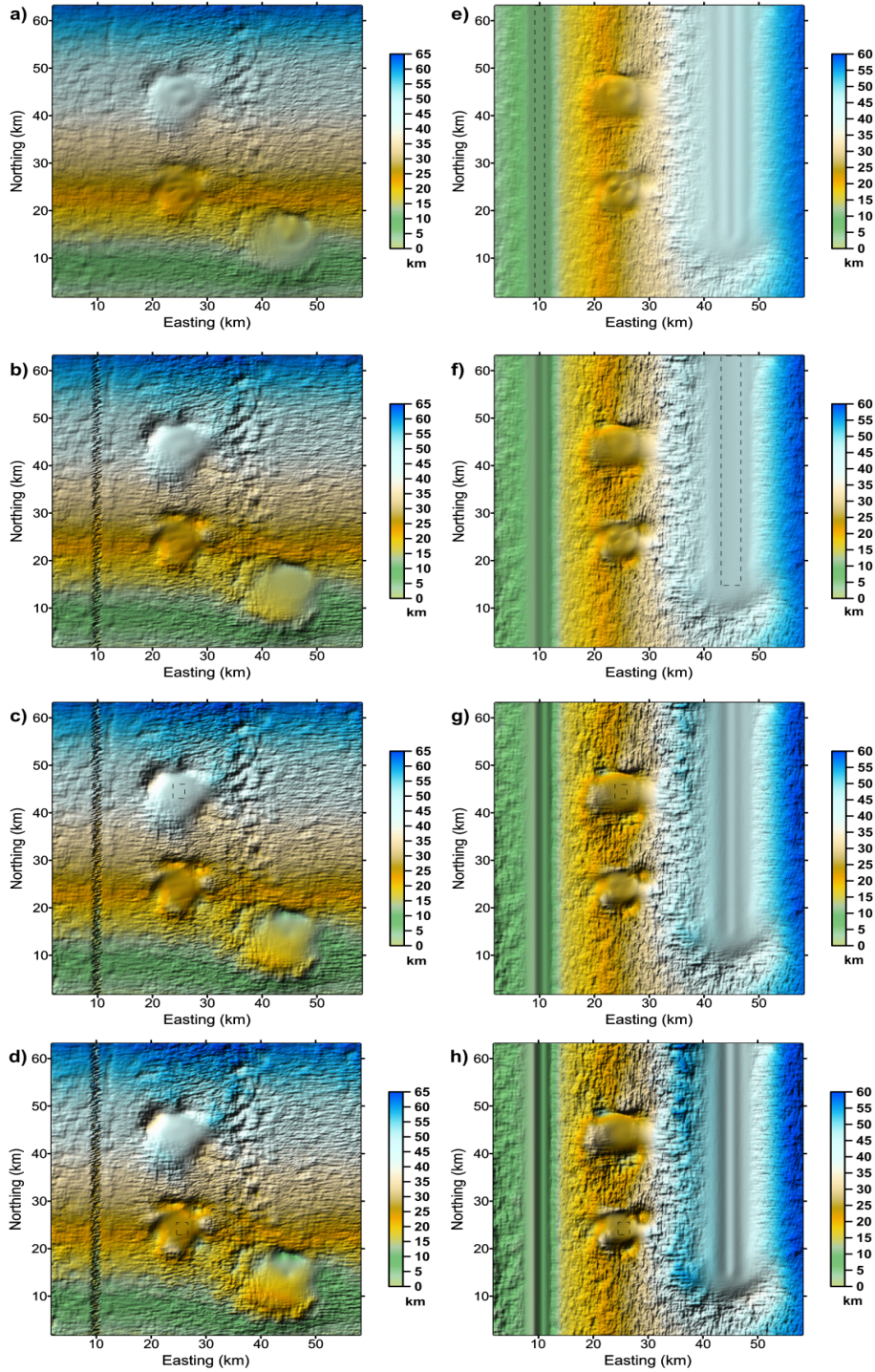


Figure 4.8: Euler deconvolution estimates for anomaly with nonlinear background.  $\hat{x}_o$ (a) – (d) and  $\hat{y}_o$  (e) – (h) estimates assuming SIs of 0, 1, 2 and 3, respectively. For each source, the plateau areas, where the methodology is applied, are outlined by dashed rectangles.

Table 4.4 shows the standard deviations for depth estimates in the presence of nonlinear background, the minimum standard deviation for each source is in boldface. For both prism and the line of poles, the minima standard deviations of depth estimates indicate the correct sources. However, in contrast with the previous

test, the minimum standard deviation for the pole indicates  $SI = 1$  and for the dipole indicates  $SI = 2$ , which are the wrong SIs for these sources. Let us recall that the correct SI to a pole-like source is  $SI = 2$  and a dipole-like source is  $SI = 3$ . Thus, the presence of a nonlinear background gives rise some interference in depth estimates.

Table 4.4: Standard deviation of depth estimates for the non-linear background. Minimum standard deviation for each source is highlighted boldface.

Source	SI = 0	SI = 1	SI = 2	SI = 3
<b>Prism</b>	<b>0.003</b>	0.232	0.468	0.703
<b>Line of poles</b>	0.109	<b>0.047</b>	0.113	0.223
<b>Monopole</b>	0.099	<b>0.078</b>	0.098	0.143
<b>Dipole</b>	0.120	0.092	<b>0.081</b>	0.099

Figure 4.7e-h shows the base-level estimates from Euler deconvolution assuming SIs of 0, 1, 2 and 3, respectively. The presence of a nonlinear background yields interfering anomalies (Figure 4.6c) that lead to strongly deformed base-level estimates (Figure 4.7e-h). Thus, this presence makes it much harder to "see" in Figure 4.7e-h the plateaus which were clearly viewed in the previous test with a constant background (Figure 4.5e-h). Table 4.5 shows the standard deviations of base-level estimates for the nonlinear background test. The minima standard deviations of base-level estimates, in boldface, confirm the correct SI of each source.

Table 4.5: Standard deviation of base-level estimates for the null background. Minimum standard deviation for each source is highlighted boldface.

Source	SI = 0	SI = 1	SI = 2	SI = 3
<b>Prism</b>	<b>98.227</b>	115.501	116.438	116.752
<b>Line of monopoles</b>	3129.689	<b>21.849</b>	27.660	31.178
<b>Monopole</b>	1862.679	11.252	<b>5.748</b>	6.383
<b>Dipole</b>	2161.655	15.889	5.532	<b>2.974</b>

This test shows that the minimum standard deviation of base-level estimates (Table 4.5) is more robust than the minimum standard deviation of depth estimates (Table 4.4) to define the correct SI when a nonlinear background exists. The minimum standard deviation of depth estimates does not give the correct SI for all sources; it fails for the monopole and for the dipole cases. In addition, the nonlinear background does not need to be previously removed to perform the Euler deconvolution when base-level estimates are used to define the correct SI.

#### 4.4.4 Test 4 - Strongly interfering anomalies with constant and nonlinear background

Here, we moved the position of the single pole to  $x_o = 25$  km and  $y_o = 38$  km and the dipole to  $x_o = 20$  km and  $y_o = 38$  km in order to give rise strongly interfering anomalies; the other sources were kept at the same position. Also, we added a nonlinear background (Figure 4.6b) to the original data (not shown) and a constant background of 47500 nT (as in test 2, Figure 4.4). Figure 4.9 shows the simulated interfering magnetic data, where we note how hard is to distinguish and locate correctly the pole-like and the dipole-like sources.

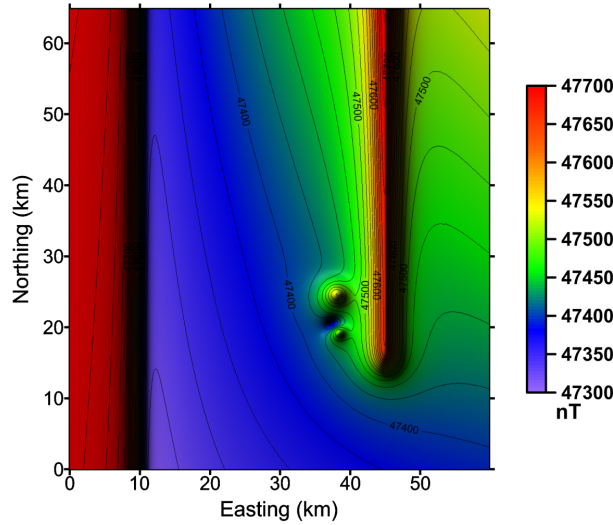


Figure 4.9: Strongly interfering anomalies with constant and nonlinear background. Noise-corrupted total-field anomaly generated by a prism (SI = 0), a line of poles (SI = 1), a single pole (SI = 2) and a dipole (SI = 3). The simulated geomagnetic field with intensity of 47500 nT has inclination of  $59^\circ$  and declination of  $10^\circ$ . The dipole is magnetized uniformly, with magnetization intensity of 5 A/m, magnetization inclination of  $9^\circ$  and declination of  $-32^\circ$ , while the other sources are magnetized by induction only. The same nonlinear background generated in Figure 4.6b was added to the anomaly.

Figure 4.10a-d shows depth estimates from Euler deconvolution assuming SIs of 0, 1, 2 and 3, respectively. Like the previous test plateaus on depth estimates are not clearly defined for the single pole 4.10c and dipole 4.10d. The poorly disclosed plateaus in Figure 4.10c-d exhibit a smoothing oscillation being bounded by abrupt variations of the depth estimates. These results differ from the plateaus shown in Figure 4.5c (single pole) and Figure 4.5d (dipole) in the case of synthetic test simulating weakly interfering anomalies (Figure 4.4). The plateaus for the application of the methodology are outlined by dashed rectangles and are defined through the intersection of horizontal estimates (Figure 4.11).

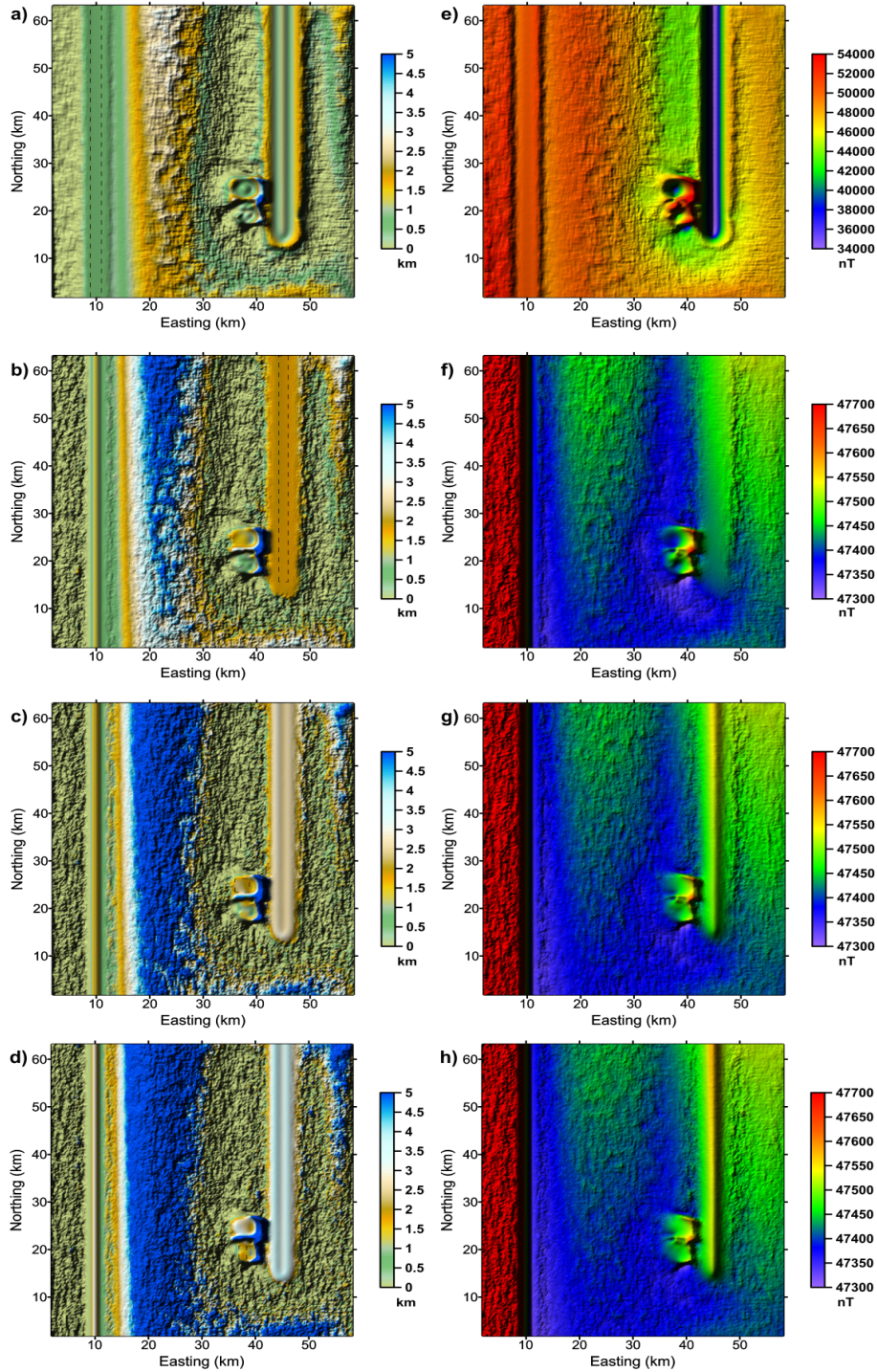


Figure 4.10: Euler deconvolution estimates for strongly interfering anomalies with constant and nonlinear background. Depth (a) – (d) and base-level (e) – (h) estimates assuming SIs of 0, 1, 2 and 3, respectively. For each source, the plateau areas, where the methodology is applied, are outlined by dashed rectangles. These areas were defined by the intersection of mapped plateaus on horizontal estimates.

Again, this test shows that the depth estimates are influenced by interfering anomalies, generated either by close sources or by nonlinear background. As in the previous test, we use the intersection of mapped plateaus on horizontal estimates

to delineate the areas to compute the standard deviations. Figure 4.11a-d shows  $\hat{x}_o$  estimates and Figure 4.11e-h shows  $\hat{y}_o$  estimates of Euler deconvolution assuming SIs of 0, 1, 2 e 3, respectively. The intersection of these estimates define the areas for the application of our methodology, these areas are defined by dashed rectangles.

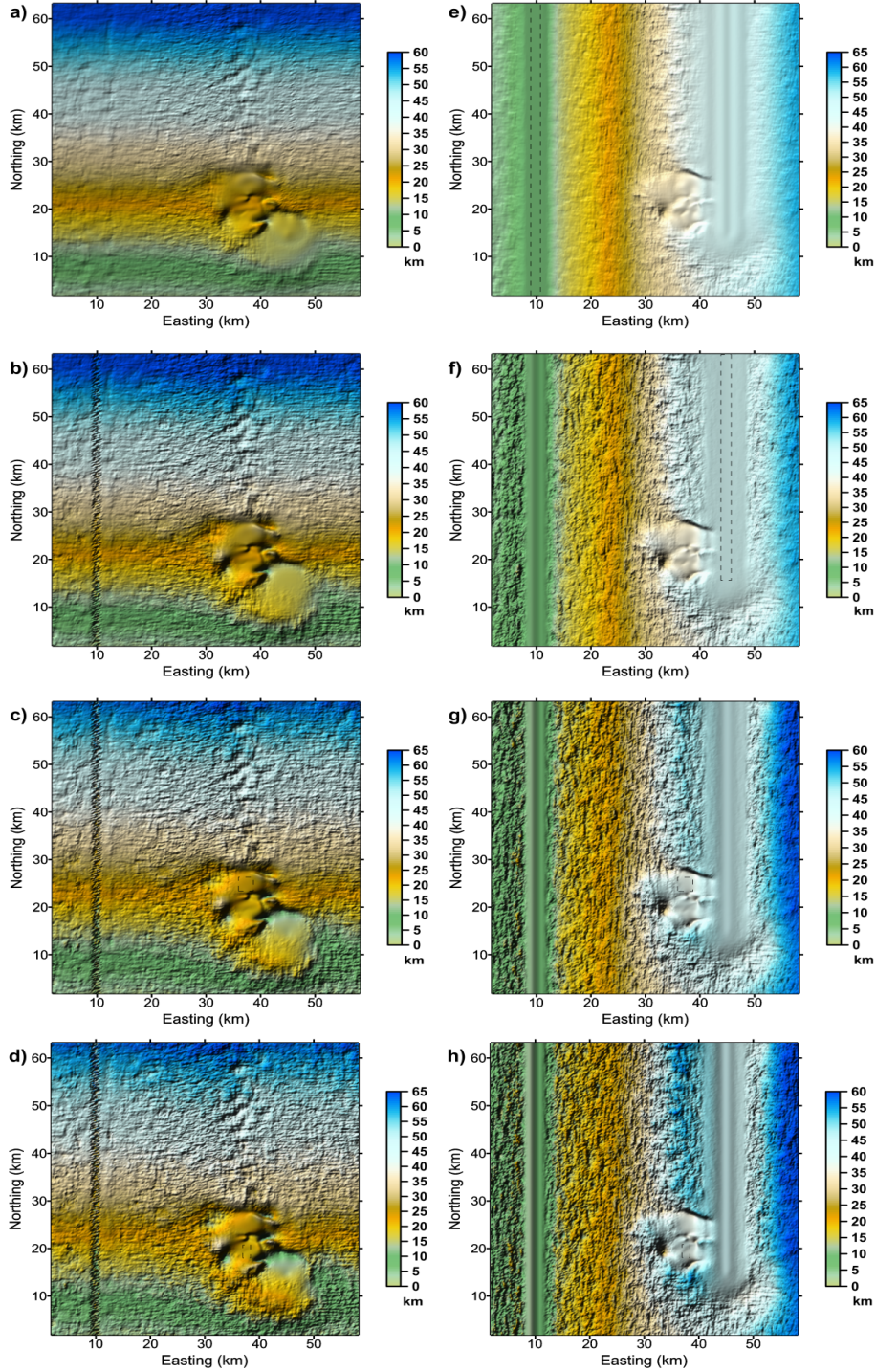


Figure 4.11: Euler deconvolution estimates for strongly interfering anomalies with constant and nonlinear background.  $\hat{x}_o$  (a) – (d) and  $\hat{y}_o$  (e) – (h) estimates assuming SIs of 0, 1, 2 and 3, respectively. For each source, the plateau areas, where the methodology is applied, are outlined by dashed rectangles.

Here, the minima standard deviations of depth estimates (Table 4.6) of the prism and the line of poles are able to correctly determine the SIs equal to 0 and 1. However, the minima standard deviations for depth estimates (Table 4.6) of the single pole and the dipole indicate a wrong SI = 1, since the true ones are SI = 2

(in the case of a pole-like source) and  $SI = 3$  (in the case of a dipole-like source).

Table 4.6: Standard deviation of depth estimates for the constant and non-linear background. Minimum standard deviation for each source is highlighted boldface.

Source	SI = 0	SI = 1	SI = 2	SI = 3
<b>Prism</b>	<b>0.003</b>	0.291	0.587	0.883
<b>Line of monopoles</b>	0.100	<b>0.038</b>	0.115	0.213
<b>Monopole</b>	0.169	<b>0.136</b>	0.188	0.301
<b>Dipole</b>	0.149	<b>0.134</b>	0.155	0.201

Figure 4.10e-h shows the base-level estimates from Euler deconvolution by assuming SIs of 0, 1, 2 and 3, respectively. As in the previous test, the locations of the pole-like and dipole-like sources are not clearly defined through the base-level estimates. Notice that these estimates have the same pattern of the anomaly (Figure 4.9).

Table 4.7 confirms that the minima standard deviations of base-level estimates are able to correctly determine the SIs, even if the anomalies strongly interfere (Figure 4.9). Although the minima standard deviations of base-level estimates indicate the correct sources (marked in boldface in Table 4.7), the differences in the standard deviations for different SIs are quite small. This happens because Euler deconvolution is applied to strongly interfering anomalies (Figure 4.9). Contrary to the results shown in Table 4.3, where the minima standard deviations are very distinguishable because the Euler deconvolution is applied to weakly interfering anomalies (Figure 4.4).

Table 4.7: Standard deviation of base-level estimates for the constant and non-linear background. Minimum standard deviation for each source is highlighted boldface.

Source	SI = 0	SI = 1	SI = 2	SI = 3
<b>Prism</b>	<b>56.307</b>	77.423	77.994	78.188
<b>Line of monopoles</b>	1534.905	<b>1958</b>	20.280	21.493
<b>Monopole</b>	2477.599	15.632	<b>13.560</b>	15.741
<b>Dipole</b>	3076.670	24.874	11.760	<b>9.125</b>

In this test, we also show that base-level estimates are more robust than depth estimates to define the correct SI when strongly interfering anomalies are generated either by nearby sources or by a nonlinear background. The smallest scattering of depth estimates failed in determining the correct SI (e.g., pole and dipole cases, see Table 4.6). Finally, we stress that there is no theoretical restriction in applying the Euler deconvolution to total-field measurements without removing either any constant or nonlinear backgrounds.

## 4.5 Application to real data set

The Goiás Alkaline Province (GAP) is a region in the central part of Brazil subject to mafic-alkaline magmatism (Marangoni and Mantovani, 2013). The region is characterized by mafic-ultramafic alkaline complexes (plutonic intrusions) in the northern portion, subvolcanic alkaline intrusions (diatremes) in the central part and volcanic products (kamafugite lava flows) in the south with several dikes throughout the area (Dutra and Marangoni, 2009; Dutra et al., 2012; Junqueira-Brod et al., 2005). Thirteen anomalies are notable in the total-field magnetic map of GAP (Dutra et al., 2012; Marangoni and Mantovani, 2013) and these intrusions have remanent magnetization (Dutra et al., 2014; Marangoni et al., 2016).

The real aeromagnetic data were acquired between June and November of 2004 with financial support from the government of the state of Goiás, Brazil (LASA and S.A., 2004). The flight lines in direction north-south were acquired every 500 m and tie lines in east-west direction every 5 km. The flight height was approximately constant at 100 m and the interval between the measurements was 0.1 s, this interval resulted in one measurement at each 8.2 m, approximately. The dataset is gridded with the same size in the  $x$  and  $y$  directions, 125 m, as originally done by the data-acquisition company (LASA and S.A., 2004). Figure 4.12a shows the total-field anomaly Figure 4.12b shows the IGRF and Figure 4.12c shows total-field measurements in the northern portion of the GAP (Junqueira-Brod et al., 2002), and the inset shows the location of the GAP. In Figure 4.12a - c, the numbers indicate the main alkaline intrusions in this region: 1 – Montes Claros de Goiás complex; 2 – Diorama; 3 – Córrego dos Bois complex; 4 – Fazenda Buriti complex; and 5 – Arenópolis. The main study area is Diorama and it is delineated by a dashed line. Note by Figure 4.12b that the IGRF variation is approximately of 100 nT in the whole area, these values are small and almost linear when compared to the total-field anomaly of the main anomalies in the area (Figure 4.12a).

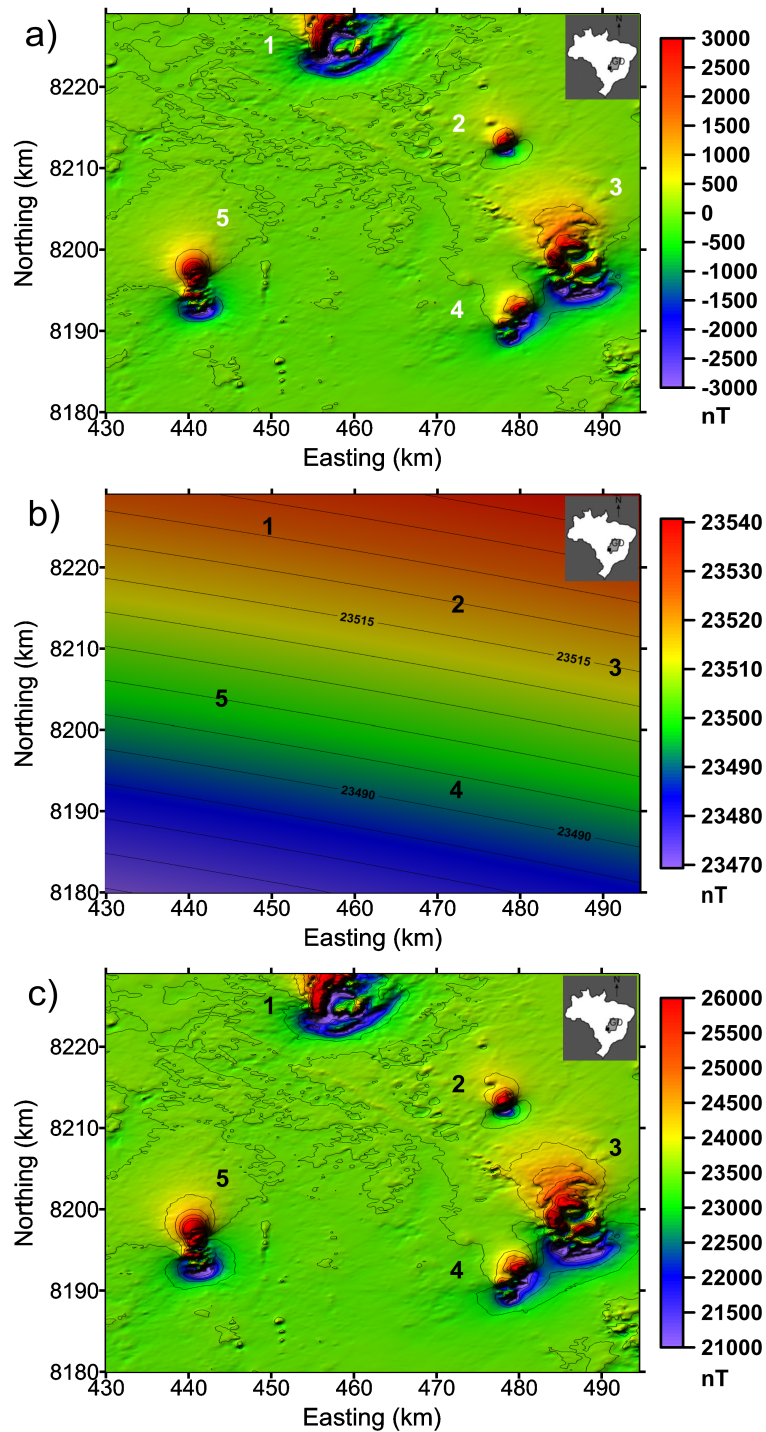


Figure 4.12: Real data set application. The numbers indicate the main alkaline intrusions in this study area: 1 – Montes Claros de Goiás complex; 2 – Diorama; 3 – Córrego dos Bois complex; 4 – Fazenda Buriti complex; and 5 - Arenópolis. The main objective of the study is Diorama, delineated with a dashed line. The inset shows the location of GAP. (a) Total-field anomaly, (b) IGRF and (c) Total-field measurements.

Junqueira-Brod et al. (2002) presented a detailed geological study of this area. According to these authors, the Montes Claros de Goiás complex is an outcrop with  $28 \text{ km}^2$  of superficial area formed by dunes, peridotites, pyroxenites, gabbros and

syenites. The ultramafic rocks form two nuclei that rise to the southwest and north, separated by a central syenitic intrusion. The Arenópolis intrusion is an elongated body generated by three distinct lithologic types: pyroxenite, melteigites and syenite, the latter outcrops. The Córrego dos Bois complex consist of two domes, mainly of dunites, covering an area of 33 km<sup>2</sup>. The structure is surrounded by a narrow and discontinuous intrusion of syenite and being intruded by dykes. The Fazenda Buriti complex covers an area of 35 km<sup>2</sup> and consists of olivine clinopyroxenite, melagabbro, syenogabbro and syenite (Dutra et al., 2012). Finally, in Diorama area are common subvolcanic intrusions, dikes, plugs and sills of picrite (Marangoni et al., 2016).

Here, we apply Euler deconvolution to the whole area, but focus our interpretation on the magnetic anomaly over the Diorama alkaline intrusion (Dutra et al., 2014; Marangoni et al., 2016; Oliveira Jr et al., 2015). The Diorama is our target anomaly because its shape resembles a weakly interfering anomalies produced by isolated sources. However, we interpret the main alkaline intrusions that yield the strongest magnetic anomalies (labeled 1-5 in Figure 4.12a-c) in our study area. Although, we interpret the strongest magnetic anomalies, we stress that there are many other weak anomalies that can generate interferences. We run Euler deconvolution with a moving-data window size of  $9 \times 9$  grid points. Figure 4.13 shows horizontal estimates,  $\hat{x}_o$  and  $\hat{y}_o$  respectively, of the study area, grid lines are plotted every 1.5 km. The plateaus in Figure 4.13 delineate the the main anomalies in the area.

Figure 4.14 shows depth estimates,  $\hat{z}_o$ , assuming SIs 2 and 3, respectively. Depth estimates assuming other indices will not be shown because there are no large plateaus identified either in horizontal (Figure 4.13) or depth estimates maps. Figure 4.14 shows many forms that seem plateaus on depth estimates. The selected plateau areas are indicated by the first letter of the name of the anomalies and delineated by rectangles in Figure 4.14. Notice that over the Diorama anomaly we identified three plateaus (D1– D3 in Figure 4.14), we also could identify these plateaus using Euler deconvolution with a window size of  $15 \times 15$  points (not shown). On the other hand, we could not clearly identify any plateau over the anomaly Fazenda Buriti (labeled 4 in Figure 4.14).

Figure 4.15a-b shows base-level estimates for the total-field anomaly (Figure reffig:real-1a) and Figure 4.15c-d shows base-level estimates for the total field measurements (Figure 4.12c) assuming SI 2 and 3, respectively. In both figures, the estimates follow the same pattern of the anomalies shown in Figure 4.12a and 4.12c and exhibit nonlinear patterns of the strong and the weak anomalies. Besides, a possible poor definition of IGRF in South America can also contribute to this nonlinear pattern (Marangoni et al., 2016).

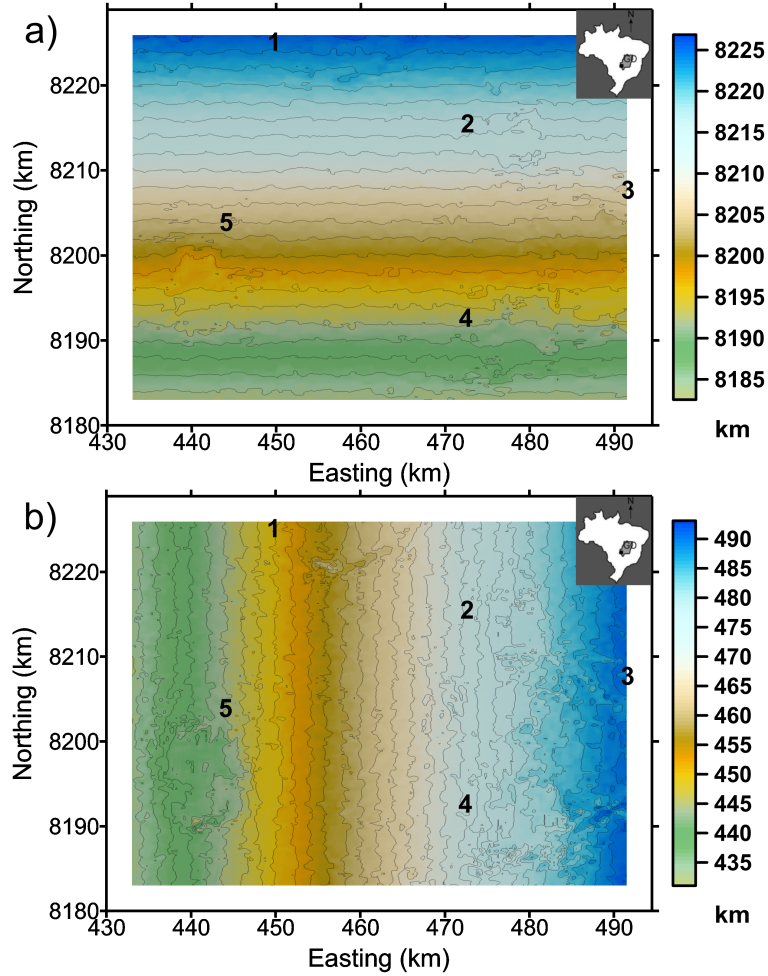


Figure 4.13: Horizontal estimates (a)  $\hat{x}_o$  and (b)  $\hat{y}_o$  of GAP, contour lines are plotted each 1.5 km.

We applied our methodology and calculated the standard deviations of base-level estimates from total-field anomaly (Table 4.8) and total-field measurements (Table 4.9) assuming SIs of 0, 1, 2 and 3. As expected, the results from both Tables are the same and the minima standard deviations of base-level estimates highlighted in boldface. Based on this analysis, we may infer that the alkaline intrusion of Diorama is generated by three plug intrusions (D1– D3 in Figure 4.14). Also, the results point that Arenópolis (A1) and Montes Claros de Goiás (CM1) are dipole-like sources and Córrego dos Bois (C1) is generated by line of poles. The unrealistic result about Córrego dos Bois complex (labeled 3 in Figure 4.12) is expected because this anomaly does not resemble to be produced by an ideal single-point source and thus the Euler’s solutions are not reliable. In fact, it seems that it is generated by complex source or multiple sources (non-ideal source). Let us recall that Euler deconvolution is grounded on Euler theorem equation for homogeneous functions; hence it should only be applied to limited situations where it can be expected to work and under the premises previously discussed. As pointed out by Barbosa and Silva (2011),

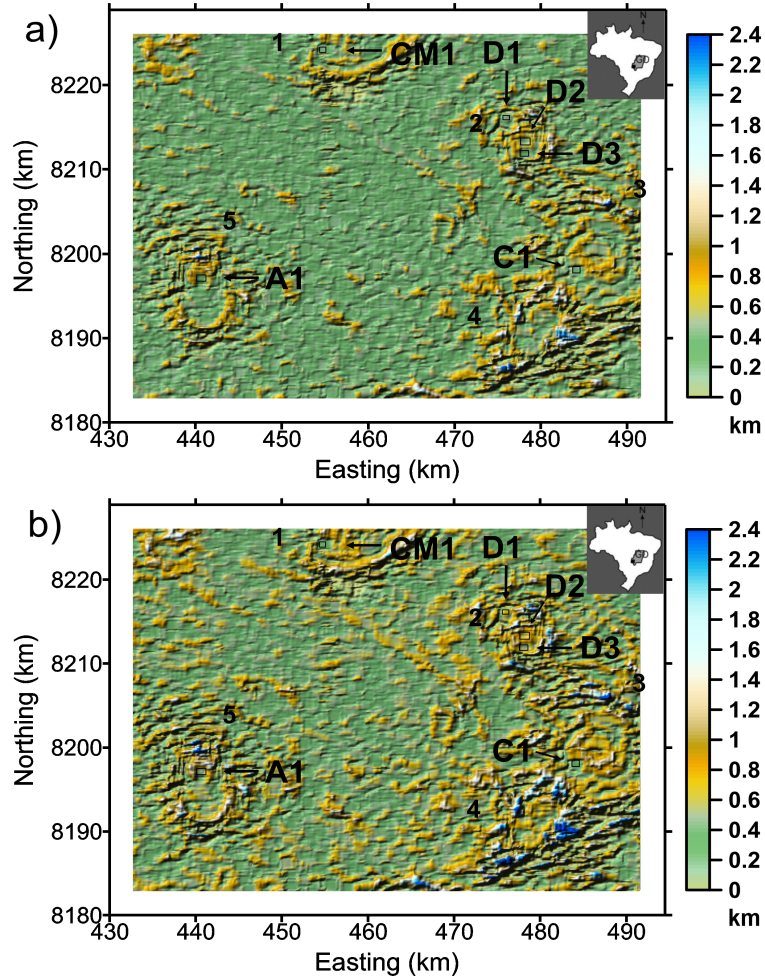


Figure 4.14: Depth estimates assuming (a)  $SI = 2$  and (b)  $SI = 3$ . The plateau areas, where the methodology is applied, are outlined in rectangles with the first letters of the name of the anomalies.

there is still more to be done to improve Euler deconvolution in order to reduce its disadvantages (e.g., its poor performance in interpreting anomalies produced by non-ideal sources) but without losing its advantage (e.g., computational efficiency).

Table 4.8: Standard deviation of base-level estimates for the total-field anomaly of GAP. Minimum standard deviation for each source is highlighted boldface.

Source	SI=0	SI=1	SI=2	SI=3
D1	5737.862	32.958	<b>19.833</b>	23.129
D2	36391.828	397.293	<b>367.469</b>	378.203
D3	18222.783	157.004	<b>152.233</b>	162.431
CB1	48968.695	<b>735.151</b>	895.069	958.207
A1	61613.215	466.475	238.997	<b>216.590</b>
MC1	45359.930	780.363	663.217	<b>643.712</b>

The most striking feature of Tables 4.8 and 4.9 is the small differences in the standard deviations for different SIs. Like the synthetic test using strongly inter-

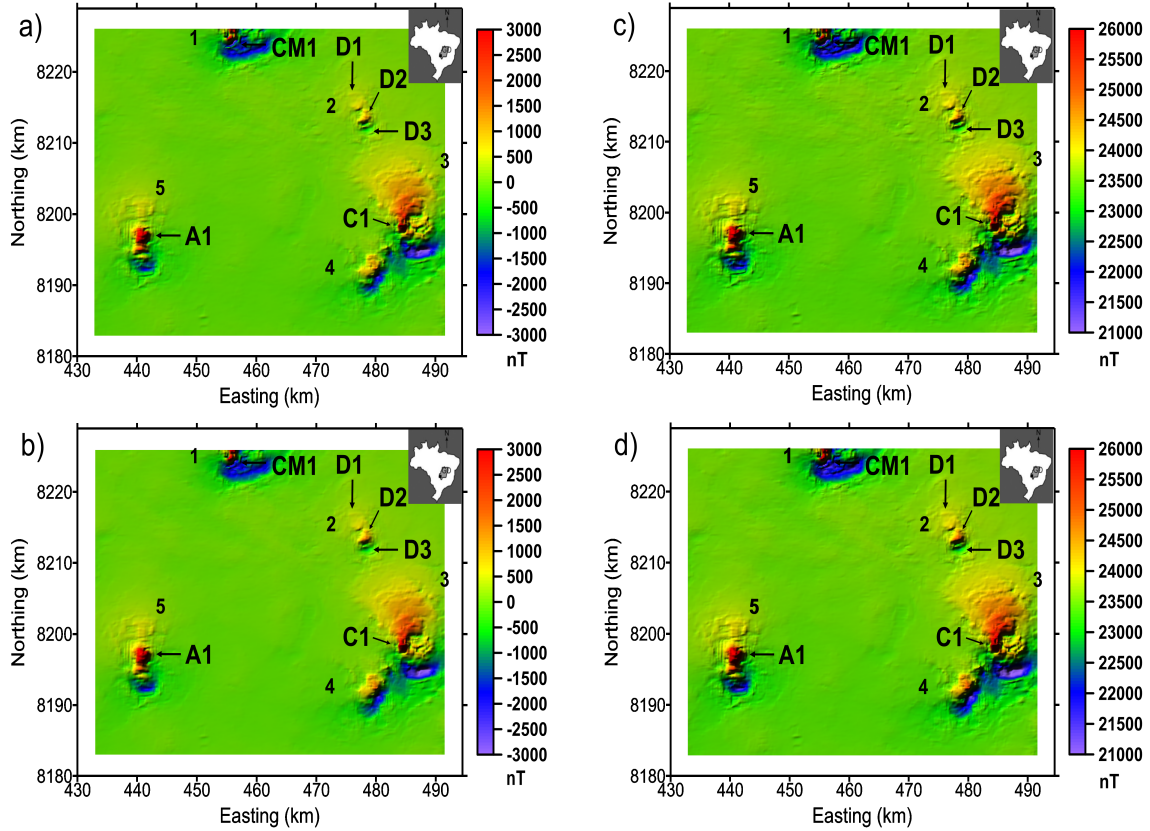


Figure 4.15: Base level estimates of total-field anomaly assuming (a)  $SI = 2$  and (b)  $SI = 3$  and base level estimates of total-field measurements assuming (c)  $SI = 2$  and (d)  $SI = 3$ . The areas where the methodology are applied are indicated with the first letters of the name of the anomalies and outlined in rectangles in Figure 4.14.

Table 4.9: Standard deviation of base-level estimates for the total field measurements of GAP. Minimum standard deviation for each source is highlighted boldface.

Source	SI=0	SI=1	SI=2	SI=3
D1	5704.204	32.492	<b>19.851</b>	23.163
D2	36571.570	393.546	<b>367.408</b>	377.060
D3	17892.637	156.249	<b>151.961</b>	162.679
CB1	49128.473	<b>735.896</b>	893,910	959.535
A1	61534.789	462.392	237.158	<b>215.245</b>
MC1	45298.429	777.376	665.279	<b>646.095</b>

fering anomalies (Figure 4.9 and Table 4.7), in the real dataset (e.g., the Diorama anomaly in Figure 4.12) the differences in the standard deviations for different SIs are small (Tables 4.8 and 4.9). Likewise, the real data (Figure 4.12) exhibit strongly interfering anomalies.

## 4.6 Final Considerations

By analyzing the Euler's equation, we show that realizations of random variables contaminating the potential-field measurements and its gradients affect the base-level estimates if, and only if, the structural index (SI) is not assumed correctly. We proposed a methodology to define the correct SI based on the minimum standard deviation of base-level estimates. For each tentative SI, we calculate the standard deviation of base-level estimates over the geological source which, in turn, is defined by the areas depicted as plateau-shaped depth estimates or plateau-shaped horizontal estimates. We tested our methodology with different sources, related to different the structural indices and achieved the correct SI even in the case of strongly interfering anomalies. We show that base-level estimates have a non-linear pattern that mimics the anomaly shape, even when the background field is null. We also show that Euler deconvolution does not require that the observed total field be corrected either from constant or nonlinear backgrounds like IGRF or regional tendency. Actually, the presence of backgrounds and nearby sources affects depth estimates, but they do not affect base-level estimates. Consequently, the determination of the correct SI based on any criterion grounded on the depth estimates can fail. Rather, the proposed criterion for determining the correct SI based on the minimum standard deviation of base-level estimates is sound. Application to a real dataset followed the expected theoretical behavior and we infer that the alkaline intrusion over Diorama (Goiás, Brazil) is generated by three plugs, based on  $SI = 2$  defined from our methodology. We applied our methodology in total-field measurements and total-field anomaly (corrected for IGRF) and the numerical results are basically the same. Both results indicate the same SI for the Diorama alkaline intrusion and show that the magnetic data does not need to be corrected for IGRF previously to the application of Euler deconvolution. Applications in areas where the anomalies do not even resemble to be generated by single-point source (ideal source) have impracticable and unpredictable results. Euler deconvolution is grounded on Euler theorem equation for homogeneous functions; hence, theoretically, it should only be applied to geological situations where it can be expected to work and under the premises it was developed for working. However, complex geological scenarios should not be ignored; ergo, there is still room for improvement in order to modify and adapt Euler deconvolution equation to non-ideal sources.

# Chapter 5

## Conclusions

This thesis contributes to the qualitative and the quantitative interpretations of magnetic data. In the qualitative interpretation, we proposed the use of the amplitude of the magnetic anomaly vector in the interpretation of total-field anomaly data at low magnetic latitudes in large areas. In the quantitative interpretation of magnetic data we deal with Euler deconvolution and proposed a reduction of the spray of the Euler estimates and a new criteria to define the correct structural index. The developments on this thesis were made using the python language and we made available the open source codes in the methodology sections of each chapter.

Some previous papers published in the literature have been used the amplitude of the magnetic anomaly vector for interpreting (or estimating) isolated magnetic sources in small areas. Differently, we used the amplitude data to produce a fast qualitative interpretation of interfering anomalies produced by multiple, complex, and closely separated 3D geologic sources over a large area at low magnetic latitudes. In this thesis, the amplitude data are used to assist a geologist in producing (or improving) an apparent-geologic map. The main advantage of the amplitude data is its weakly dependence on the magnetization direction. This aspect turns the amplitude data attractive to interpret areas at low latitudes with remanent magnetized bodies. Therefore, in this thesis, we propose the use of the amplitude data as an initial attempt to yield an apparent-geologic map either in large-scale areas at low latitudes with remanent magnetized bodies or in areas where the conventional geologic mapping are not feasible to be accomplished due to the features of the terrain (e.g., rugged topography, dense forests, poor rock exposures). Important anomalies that are not clearly seen in either total-field anomaly map or in filtered map (such as reduced-to-pole or total gradient maps) may show up in the amplitude data map. The interpretation of the amplitude data computed in a large region of the Amazonian Craton, at low latitudes in northern Brazil, matches the behavior described in the synthetic tests which includes centered anomalies present in the total-field anomaly map and correlated with the known outcropping rocks in the

geological map of the region. More than that, the amplitude data provide a plausible geophysical interpretation of the unmapped geology suggesting multiple buried geologic bodies following a trend of the known outcropping geologic units.

In the quantitative interpretation of magnetic data, we propose two new methodologies in the classic Euler deconvolution method that contribute to solve two well-known drawbacks: the spray of Euler solutions and the definition of the correct structural index. In our first quantitative interpretation, we propose a methodology to reduce the spray of Euler solutions by selecting the reliable solutions as those estimated from the moving-data windows with the greatest standard deviations of the vertical derivatives of the total-field anomaly. Our methodology to select the reliable Euler solutions can be combined with other methods to reduce the spray of Euler solutions and it can be used in other Euler extensions as the extended Euler method. We show that this methodology is able to distinguish the four possible structural indices and works in a scenario with interfering anomalies. Real data application makes it possible to infer the nature of the Anitápolis anomaly, southern Brazil, as a plug-like intrusion, which represents a geologically meaningful hypothesis.

In our second quantitative interpretation, the base-level estimates were used to define the correct structural index in Euler deconvolution. Grounded on Euler's equation - which indicates that random variables contaminating the magnetic anomaly and its gradients affect the base-level estimates if, and only if, the structural index is assumed wrongly - our methodology proposed the minimum standard deviation of base-level estimates for determining the correct structural index in Euler deconvolution. We also show that a magnetic background anomaly does not interfere in the definition of the structural index and on the depth estimates. On the application of our methodology in the Goiás Alkaline Province, central Brazil, we infer that the Diorama anomaly was generated by three plug intrusions and the Arenópolis and Montes Claros de Goiás anomalies were generated by dipole-like sources, these anomalies seem to be generated by ideal single-point sources. Moreover, we call attention that the Euler deconvolution always generates solutions, however these solutions may be unrealistic if it is applied to anomalies produced by sources that do not behave as single-point geologic source.

The qualitative and quantitative methods presented in this thesis can be used together in a future study. A possible scenario is the computing of the amplitude of the magnetic anomaly vector and the Euler deconvolution from the total-field anomaly with the overlaying of the results.

# Bibliography

- Adriano, L. B., Menezes, P. T., Adriano, M. S., Cunha, A. S., Cabrera, M. H., Silva, D. S., Moura, L. P., 2018. Jequitinhonha basin: Structural aspects, relationship with igneous activity, and hydrocarbon exudations. *Interpretation* 6 (1), T51–T60.
- Agarwal, B., Srivastava, S., 2009. Analyses of self-potential anomalies by conventional and extended euler deconvolution techniques. *Computers & Geosciences* 35 (11), 2231–2238.
- Airo, M.-L., Loukola-Ruskeeniemi, K., 2004. Characterization of sulfide deposits by airborne magnetic and gamma-ray responses in eastern finland. *Ore Geology Reviews* 24 (1), 67 – 84, ores and organic matter.
- Almeida, F., Hasui, Y., Brito Neves, B., R.A., F., 1981. Brazilian structural provinces: an introduction. *Earth-Science Reviews* 17, 1–29.
- Baranov, V., 1957. A new method for interpretation of aeromagnetic maps: Pseudo-gravimetric anomalies. *Geophysics* 22, 359–383.
- Barbosa, V. C., Silva, J. B., 2006. Interactive 2d magnetic inversion: A tool for aiding forward modeling and testing geologic hypotheses. *Geophysics* 71 (5), L43–L50.
- Barbosa, V. C., Silva, J. B., 2011. Reconstruction of geologic bodies in depth associated with a sedimentary basin using gravity and magnetic data. *Geophysical Prospecting* 59 (6), 1021–1034.
- Barbosa, V. C., Silva, J. B., Medeiros, W. E., 1999. Stability analysis and improvement of structural index estimation in euler deconvolution. *Geophysics* 64 (1), 48–60.
- Barbosa, V. C., Silva, J. B., Medeiros, W. E., 2000. Making euler deconvolution applicable to small ground magnetic surveys. *Journal of Applied Geophysics* 43 (1), 55–68.

- Beiki, M., Pedersen, L. B., 2010. Eigenvector analysis of gravity gradient tensor to locate geologic bodies. *Geophysics* 75 (6), I37–I49.
- Biondi, J., 2005. Brazilian mineral deposits associated with alkaline and alkaline-carbonatite complexes. In: P., C.-C., C.B., G. (Eds.), *Mesozoic to Cenozoic Alkaline Magmatism in the Brazilian Platform*. Vol. 1. Edusp/Fapesp, São Paulo, pp. 707 – 750.
- Blakely, R. J., 1996. *Potential theory in gravity and magnetic applications*. Cambridge University Press.
- Busby, J., Peart, R., Green, C., Ogilvy, R., Williamson, J., 1991. A search for direct hydrocarbon indicators in the formby area. *Geophysical Prospecting* 39 (5), 691–710.
- Cella, F., Fedi, M., 2012. Inversion of potential field data using the structural index as weighting function rate decay. *Geophysical Prospecting* 60 (2), 313–336.
- Chulliat, A., Macmillan, S., Alken, P., Beggan, C., Nair, M., Hamilton, B., Woods, A., Ridley, V., Maus, S., Thomson, A., 2014. The us/uk world magnetic model for 2015-2020. NOAA National Geophysical Data Center, Boulder, CO.
- Comin-Chiaramonti, P., Gomes, C., Censi, P., Speziale, S., 2005. Carbonatites from southeastern brazil: a model for the carbon and oxygen isotope. In: P., C.-C., C.B., G. (Eds.), *Mesozoic to Cenozoic Alkaline Magmatism in the Brazilian Platform*. Vol. 1. Edusp/Fapesp, São Paulo, pp. 629 – 656.
- Cooper, G., 2006. Obtaining dip and susceptibility information from euler deconvolution using the hough transform. *Computers & geosciences* 32 (10), 1592–1599.
- CPRM, 2011. Project: Aerogeophysical survey paraná-santa catarina: Survey and data processing: Final report, rio de janeiro, brazil, vol. 22 and maps [in portuguese]. Tech. Rep. 1.
- CPRM, 2015. Project: Aerogeophysical survey of carajás: Survey and data processing: Final report, rio de janeiro, brazil, vol. 22 and maps [in portuguese]. Tech. Rep. 1.
- Curto, J. B., Pires, A. C., Silva, A. M., Crósta, Á. P., 2012. The role of airborne geophysics for detecting hydrocarbon microseepages and related structural features: The case of remanso do fogo, brazil. *Geophysics* 77 (2), B35–B41.

- Dampney, C., 1969. The equivalent source technique. *Geophysics* 34 (1), 39–53.
- Davis, K., Li, Y., 2011. Fast solution of geophysical inversion using adaptive mesh, space-filling curves and wavelet compression. *Geophysical Journal International* 185, 157–166.
- Dewangan, P., Ramprasad, T., Ramana, M., Desa, M., Shailaja, B., 2007. Automatic interpretation of magnetic data using euler deconvolution with nonlinear background. *Pure and Applied Geophysics* 164 (11), 2359–2372.
- Donovan, T. J., Hendricks, J. D., Roberts, A. A., Eliason, P. T., 1984. Low-altitude aeromagnetic reconnaissance for petroleum in the arctic national wildlife refuge, alaska. *Geophysics* 49 (8), 1338–1353.
- Durrheim, R., Cooper, G., 1998. Euldep: a program for the euler deconvolution of magnetic and gravity data. *Computers & geosciences* 24 (6), 545–550.
- Dutra, A. C., Marangoni, Y. R., 2009. Gravity and magnetic 3d inversion of morro do engenho complex, central brazil. *Journal of South American Earth Sciences* 28 (2), 193–203.
- Dutra, A. C., Marangoni, Y. R., Junqueira-Brod, T. C., 2012. Investigation of the goiás alkaline province, central brazil: Application of gravity and magnetic methods. *Journal of South American Earth Sciences* 33 (1), 43–55.
- Dutra, A. C., Marangoni, Y. R., Trindade, R. I., 2014. Aeromagnetic and physical-chemical properties of some complexes from goiás alkaline province. *Brazilian Journal of Geology* 44 (3), 361–373.
- Fairhead, J., Bennett, K., Gordon, D., Huang, D., et al., 1994. Euler: Beyond the “black box”. In: 1994 SEG Annual Meeting. Society of Exploration Geophysicists.
- Fedi, M., Florio, G., Paoletti, V., 2015. Mhode: a local-homogeneity theory for improved source-parameter estimation of potential fields. *Geophysical Journal International* 202 (2), 887–900.
- Fedi, M., Florio, G., Quarta, T. A., 2009. Multiridge analysis of potential fields: Geometric method and reduced euler deconvolution. *Geophysics* 74 (4), L53–L65.
- Filina, I., 2019. Crustal architecture of the northwestern and central gulf of mexico from integrated geophysical analysis. *Interpretation* 7 (4), T899–T910.

- FitzGerald, D., Reid, A., McInerney, P., 2004. New discrimination techniques for euler deconvolution. *Computers & Geosciences* 30 (5), 461–469.
- Florio, G., Fedi, M., 2014. Multiridge euler deconvolution. *Geophysical Prospecting* 62 (2), 333–351.
- Florio, G., Fedi, M., Pašteka, R., 2014. On the estimation of the structural index from low-pass filtered magnetic data. *Geophysics* 79 (6), J67–J80.
- Fregoso, E., Gallardo, L. A., García-Abdeslem, J., 2015. Structural joint inversion coupled with euler deconvolution of isolated gravity and magnetic anomalies. *Geophysics* 80 (2), G67–G79.
- Gallardo, L., Fontes, S., Meju, M., Buonora, M., De Lugao, P., 2012. Robust geophysical integration through structure-coupled joint inversion and multi-spectral fusion of seismic reflection, magnetotelluric, magnetic, and gravity images: Example from santos basin, offshore brazil. *Geophysics* 77 (5), B237–B251.
- Gamey, T. J., 2008. Magnetic response of clustered uxo targets. *Journal of Environmental & Engineering Geophysics* 13 (3), 211–221.
- Gerovska, D., Araúzo-Bravo, M. J., 2003. Automatic interpretation of magnetic data based on euler deconvolution with unprescribed structural index. *Computers & Geosciences* 29 (8), 949–960.
- Gerovska, D., Stavrev, P., 2006. Magnetic data analysis at low latitudes using magnitude transforms. *Geophysical Prospecting* 54 (1), 89–98.
- Glicken, M., 1955. Uses and limitations of the airborne magnetic gradiometer. *Mining Engineering* 7 (pt 2), 1054–1056.
- Gonçalves, B. F., Sampaio, E. E., 2013. Interpretation of airborne and ground magnetic and gamma-ray spectrometry data in prospecting for base metals in the central-north part of the itabuna-salvador-curaçá block, bahia, brazilinterpretation of mag-gama data. *Interpretation* 1 (1), T85–T100.
- Grainger, C. J., Groves, D., Tallarico, F., I.R, F., 2008. Metallogenesis of the carajás mineral province, southern amazon craton, brazil: Varying styles of archean through paleoproterozoic to neoproterozoic base-and precious-metal mineralisation. *Ore Geology Reviews* 33, 451–489.
- Gubbins, D., 2004. Time series analysis and inverse theory for geophysicists. Cambridge University Press.

- Gunn, P., 1975. Linear transformations of gravity and magnetic fields. *Geophysical prospecting* 23 (2), 300–312.
- Gunn, P., Dentith, M., 1997. Magnetic responses associated with mineral deposits. *AGSO Journal of Australian Geology and Geophysics* 17, 145–158.
- Haldar, S., 2017. Chapter 10 - exploration guide. In: Haldar, S. (Ed.), *Platinum-Nickel-Chromium Deposits*. Elsevier, pp. 247 – 266.
- Hansen, P. C., 1992. Analysis of discrete ill-posed problems by means of the l-curve. *SIAM review* 34 (4), 561–580.
- Hansen, R., Pawlowski, R., 1989. Reduction to the pole at low latitude by wiener filtering. *Geophysics* 54, 1607–1613.
- Hansen, R., Suci, L., 2002. Multiple-source euler deconvolution. *Geophysics* 67 (2), 525–535.
- Hartman, R. R., Teskey, D. J., Friedberg, J. L., 1971. A system for rapid digital aeromagnetic interpretation. *Geophysics* 36 (5), 891–918.
- Henderson, R. G., Zietz, I., 1948. Analysis of total magnetic-intensity anomalies produced by point and line sources. *Geophysics* 13 (3), 428–436.
- Henderson, R. G., Zietz, I., 1949a. The computation of second vertical derivatives of geomagnetic fields. *Geophysics* 14 (4), 508–516.
- Henderson, R. G., Zietz, I., 1949b. The upward continuation of anomalies in total magnetic intensity fields. *Geophysics* 14 (4), 517–534.
- Hidalgo-Gato, M., Barbosa, V., Jul. 2015. Edge detection of potential-field sources using scale-space monogenic signal: Fundamental principles. *GEOPHYSICS* 80 (5), J27–J36.
- Hidalgo-Gato, M. C., Barbosa, V. C., 2019. Fast 3d magnetic inversion of a surface relief in the space domain. *Geophysics* 84 (5), J57–J67.
- Hinze, W. J., Von Frese, R. R., Saad, A. H., 2013. *Gravity and magnetic exploration: Principles, practices, and applications*. Cambridge University Press.
- Hood, P., 1965. Gradient measurements in aeromagnetic surveying. *Geophysics* 30 (5), 891–902.
- Hsu, S.-K., 2002. Imaging magnetic sources using euler’s equation. *Geophysical Prospecting* 50 (1), 15–25.

- Irving, J., Mullineux, N., 1959. Mathematics in physics and engineering. Academic Press, New York.
- Junqueira-Brod, T. C., Gaspar, J. C., Brod, J. A., Jost, H., Barbosa, E. S. R., Kafino, C. V., 2005. Emplacement of kamafugite lavas from the goiás alkaline province, brazil: constraints from whole-rock simulations. *Journal of South American Earth Sciences* 18 (3-4), 323–335.
- Junqueira-Brod, T. C., Roig, H. L., Gaspar, J. C., Brod, J. A., Meneses, P. R., 2002. A província alcalina de goiás e a extensão do seu vulcanismo kamafugítico. *Revista Brasileira de Geociências* 32 (4), 559–566.
- Keating, P., Pilkington, M., 2004. Euler deconvolution of the analytic signal and its application to magnetic interpretation. *Geophysical Prospecting* 52 (3), 165–182.
- Klein, E. L., Rodrigues, J. B., Queiroz, J. D., Oliveira, R. G., Guimarães, S. B., Chaves, C. L., 2017. Deposition and tectonic setting of the palaeoproterozoic castelo dos sonhos metasedimentary formation, tapajós gold province, amazonian craton, brazil: age and isotopic constraints. *International Geology Review* 59 (7), 864–883.
- Krahenbuhl, R. A., Li, Y., 2017. Investigation of magnetic inversion methods in highly magnetic environments under strong self-demagnetization effect. *Geophysics* 82 (6), J83–J97.
- Ku, C. C., Sharp, J. A., 1983. Werner deconvolution for automated magnetic interpretation and its refinement using marquardt’s inverse modeling. *Geophysics* 48 (6), 754–774.
- LaFehr, T. R., Nabighian, M. N., 2012. Fundamentals of gravity exploration. Society of Exploration Geophysicists.
- LASA, P., S.A., E., 2004. Project: Aerogeophysical survey of goiás state, first phase. survey and data processing final report. rio de janeiro, sgm/mme/cprm and sic/sgm/funmineral/goiás state, brazil, vol. 22 and maps (in portuguese). Tech. Rep. 1.
- Leao, J. W., Silva, J. B., 1989. Discrete linear transformations of potential field data. *Geophysics* 54 (4), 497–507.
- Leão-Santos, M., Li, Y., R., M., 2015. Application of 3d magnetic amplitude inversion to iron oxide-copper- gold deposits at low magnetic latitudes:

- A case study from carajás mineral province, brazil. *Geophysics* 80 (2), B13–B22.
- Li, S., Li, Y., 2014. Inversion of magnetic anomaly on rugged observation surface in the presence of strong remanent magnetization. *Geophysics* 79 (2), J11–J19.
- Li, X., 2003. On the use of different methods for estimating magnetic depth. *The Leading Edge* 22 (11), 1090–1099.
- Li, X., 2006. Understanding 3d analytic signal amplitude. *Geophysics* 71 (2), L13–L16.
- Li, X., Pilkington, M., 2016. Attributes of the magnetic field, analytic signal, and monogenic signal for gravity and magnetic interpretation. *Geophysics* 81 (6), J79–J86.
- Li, Y., M., N., D.W., O., 2014. Using an equivalent source with positivity for low-latitude reduction to the pole without striation. *Geophysics* 79 (6), J81–J90.
- Li, Y., Oldenburg, D., 2001. Stable reduction to the pole at the magnetic equator. *Geophysics* 66 (2), 571–578.
- Li, Y., Oldenburg, D., 2010. Rapid construction of equivalent sources using wavelets. *Geophysics* 75 (3), L51–L59.
- Li, Y., Oldenburg, D. W., 1996. 3-d inversion of magnetic data. *Geophysics* 61 (2), 394–408.
- Li, Y., Shearer, S. E., Haney, M. M., Dannemiller, N., 2010. Comprehensive approaches to 3d inversion of magnetic data affected by remanent magnetization. *Geophysics* 75 (1), L1–L11.
- Li, Y., Zhanxiang, H., L., Y., 2012. Application of magnetic amplitude inversion in exploration for volcanic units in a basin environment. *Geophysics* 77 (5), B219–B225.
- Liu, S., Hu, X., Liu, T., Feng, J., Gao, W., L., Q., 2013. Magnetization vector imaging for borehole magnetic data based on magnitude magnetic anomaly. *Geophysics* 78 (6), D429–D444.
- Liu, S., Hu, X., Xi, Y., Liu, T., S., X., 2015. 2d sequential inversion of total magnitude and total magnetic anomaly data affected by remanent magnetization. *Geophysics* 80 (3), K1–K12.

- Liu, S., Hu, X., Zhang, H., Geng, M., B., Z., 2017. 3d magnetization vector inversion of magnetic data: Improving and comparing methods. *Pure and Applied Geophysics* 174 (12), 4421–4444.
- Lourenço, J., Menezes, P. T., Barbosa, V. C., 2014. Connecting onshore-offshore campos basin structures: Interpretation of high-resolution airborne magnetic data. *Interpretation* 2 (4), SJ35–SJ45.
- Louro, V. H. A., Mantovani, M. S. M., Ribeiro, V. B., 2014. Magnetic field analysis of morro do leme nickel deposit. *Geophysics* 79 (6), K1–K9.
- MacLeod, I. N., Jones, K., T.F., D., 1993. 3-d analytic signal in the interpretation of total magnetic field data at low magnetic latitudes. *Exploration Geophysics* 24, 678–688.
- Marangoni, Y. R., Mantovani, M. S., 2013. Geophysical signatures of the alkaline intrusions bordering the paraná basin. *Journal of South American Earth Sciences* 41, 83–98.
- Marangoni, Y. R., Zhang, H., Ferreira, H. J., 2016. Gravity and magnetic integrated data interpretation of the corrêgo dos bois complex, goiás alkaline province, central brazil. *Revista Brasileira de Geofísica* 33 (4).
- Marson, I., Klingele, E., 1993. Advantages of using the vertical gradient of gravity for 3-d interpretation. *Geophysics* 58 (11), 1588–1595.
- Mas-Colell, A., Whinston, M., Green, J. R., 1995. *Microeconomic Theory*. Oxford University Press.
- Medeiros, W. E., Silva, J. B., 1996. Geophysical inversion using approximate equality constraints. *Geophysics* 61 (6), 1678–1688.
- Melo, F. F., Barbosa, V. C., 2018. Correct structural index in euler deconvolution via base-level estimates. *Geophysics* 83 (6), J87–J98.
- Melo, F. F., Barbosa, V. C., Uieda, L., Oliveira Jr, V. C., Silva, J. B., 2013. Estimating the nature and the horizontal and vertical positions of 3d magnetic sources using euler deconvolution. *Geophysics* 78 (6), J87–J98.
- Mendonça, C. A., Silva, J. B. C., 1993. A stable truncated series approximation of the reduction-to-the pole operator. *Geophysics* 58, 1084–1090.
- Mikhailov, V., Galdeano, A., Diament, M., Gvishiani, A., Agayan, S., Bogoutdinov, S., Graeva, E., Sailhac, P., 2003. Application of artificial intelligence for euler solutions clustering. *Geophysics* 68 (1), 168–180.

- Miller, H. G., Singh, V., 1994. Potential field tilt—a new concept for location of potential field sources. *Journal of Applied Geophysics* 32 (2-3), 213–217.
- Mushayandebvu, M. F., Van Driel, P., Reid, A. B., Fairhead, J. D., 2001. Magnetic source parameters of two-dimensional structures using extended euler deconvolution. *Geophysics* 66 (3), 814–823.
- Nabighian, M. N., Grauch, V., Hansen, R., LaFehr, T., Li, Y., Peirce, J., Phillips, J., Ruder, M., 2005. The historical development of the magnetic method in exploration. *Geophysics* 70 (6), 33ND–61ND.
- Nabighian, M. N., Hansen, R., 2001. Unification of euler and werner deconvolution in three dimensions via the generalized hilbert transform. *Geophysics* 66 (6), 1805–1810.
- Naudy, H., 1971. Automatic determination of depth on aeromagnetic profiles. *Geophysics* 36 (4), 717–722.
- Nunes, T. M., Barbosa, V. C. F., Silva, J. B. C., 2008. Magnetic basement depth inversion in the space domain. *Pure and applied geophysics* 165 (9-10), 1891–1911.
- Oliveira Jr, V., Sales, D., Barbosa, V., Uieda, L., 2015. Estimation of the total magnetization direction of approximately spherical bodies. *Nonlinear Processes in Geophysics* 22 (2), 215–232.
- Oliveira Jr, V. C., Barbosa, V. C., Uieda, L., 2013. Polynomial equivalent layer. *Geophysics* 78 (1), G1–G13.
- Paoletti, V., Ialongo, S., Florio, G., Fedi, M., Cella, F., 2013. Self-constrained inversion of potential fields. *Geophysical Journal International* 195 (2), 854–869.
- Parker, R. L., Shure, L., Hildebrand, J. A., 1987. The application of inverse theory to seamount magnetism. *Reviews of Geophysics* 25 (1), 17–40.
- Pasteka, R., 2006. The role of the interference polynomial in the euler deconvolution algorithm. *Bollettino di Geofisica Teorica ed Applicata* 47 (1-2), 171–180.
- Pilkington, M., Beiki, M., 2013. Mitigating remanent magnetization effects in magnetic data using the normalized source strength. *Geophysics* 78 (3), J25–J32.

- Pilkington, M., Keating, P., 2009. The utility of potential field enhancements for remote predictive mapping. *Canadian Journal of Remote Sensing* 35 (sup1), S1–S11.
- Pilkington, M., Tschirhart, V., 2017. Practical considerations in the use of edge detectors for geologic mapping using magnetic data. *Geophysics* 82 (3), J1–J8.
- Portniaguine, O., Zhdanov, M. S., 2002. 3-d magnetic inversion with data compression and image focusing. *Geophysics* 67 (5), 1532–1541.
- Ravat, D., 1996. Analysis of the euler method and its applicability in environmental magnetic investigations. *Journal of Environmental and Engineering Geophysics* 1 (3), 229–238.
- Ravat, D., Wang, B., Wildermuth, E., Taylor, P. T., 2002. Gradients in the interpretation of satellite-altitude magnetic data: an example from central africa. *Journal of Geodynamics* 33 (1-2), 131–142.
- Reford, M., Sumner, J., 1964. Aeromagnetism. *Geophysics* 29 (4), 482–516.
- Reid, A., FitzGerald, D., McInerney, P., et al., 2003. Euler deconvolution of gravity data. In: 2003 SEG Annual Meeting. Society of Exploration Geophysicists.
- Reid, A. B., Allsop, J., Granser, H., Millett, A. t., Somerton, I., 1990. Magnetic interpretation in three dimensions using euler deconvolution. *Geophysics* 55 (1), 80–91.
- Reid, A. B., Ebbing, J., Webb, S. J., 2014. Avoidable euler errors—the use and abuse of euler deconvolution applied to potential fields. *Geophysical Prospecting* 62 (5), 1162–1168.
- Reid, A. B., Thurston, J. B., 2014. The structural index in gravity and magnetic interpretation: Errors, uses, and abuses. *Geophysics* 79 (4), J61–J66.
- Roest, W. R., Verhoef, J., M., P., 1992. Magnetic interpretation using 3-d analytic signal. *Geophysics* 57, 116–125.
- Salem, A., Ushijima, K., Gamey, T. J., Ravat, D., 2001. Automatic detection of uxo from airborne magnetic data using a neural network. *Subsurface sensing technologies and applications* 2 (3), 191–213.
- Santos, J. O. S., Hartmann, L., Gaudette, H. E., Groves, D. I., McNaughton, N. J., Fletcher, I. R., 2000. A new understanding of the provinces of the

- amazon craton based on integration of field mapping and u-pb and sm-nd geochronology. *Gondwana Research* 3, 453–488.
- Scheibe, L., Furtado, S., Comin-Chiaramonti, P., Gomes, C., 2005. Cretaceous alkaline magmatism from santa catarina state, southern brazil. In: P., C.-C., C.B., G. (Eds.), *Mesozoic to Cenozoic Alkaline Magmatism in the Brazilian Platform*. Vol. 1. Edusp/Fapesp, São Paulo, pp. 523 – 571.
- Schmidt, P., Clark, D., Leslie, K., Bick, M., Tilbrook, D., Foley, C., 2004. Getmag—a squid magnetic tensor gradiometer for mineral and oil exploration. *Exploration Geophysics* 35 (4), 297–305.
- Silva, J., 1986. Reduction to the pole as an inverse problem and its application to low-latitude anomalies. *Geophysics* 51, 369–382.
- Silva, J., Barbosa, V., Medeiros, W., 2001. Scattering, symmetry, and bias analysis of source-position estimates in euler deconvolution and its practical implications. *Geophysics* 66 (4), 1149–1156.
- Silva, J. B., Barbosa, V. C., 2003. 3d euler deconvolution: Theoretical basis for automatically selecting good solutions. *Geophysics* 68 (6), 1962–1968.
- Silva, J. B., Hohmann, G. W., 1984. Airborne magnetic susceptibility mapping. *Exploration Geophysics* 15 (1), 1–13.
- Silva, J. B., Vasconcelos, S. S., Barbosa, V. C., 2010. Apparent-magnetization mapping using entropic regularization. *Geophysics* 75 (2), L39–L50.
- Siqueira, F. C., Oliveira Jr., V. C., Barbosa, V. C., 2017. Fast iterative equivalent-layer technique for gravity data processing: A method grounded on excess mass constraint. *Geophysics* 82 (4), G57–G69.
- Slack, H. A., Lynch, V. M., Langan, L., 1967. The geomagnetic gradiometer. *Geophysics* 32 (5), 877–892.
- Smellie, D., 1956. Elementary approximations in aeromagnetic interpretation. *Geophysics* 21 (4), 1021–1040.
- Sokolnikoff, I. S., Redheffer, R. M., Avents, J., 1966. *Mathematics of physics and modern engineering*. Mcgraw-Hill College, New York.
- Stavrev, P., Gerovska, D., 2000. Magnetic field transforms with low sensitivity to the direction of source magnetization and high centricity. *Geophysical Prospecting* 48 (2), 317–340.

- Stavrev, P., Reid, A., 2007. Degrees of homogeneity of potential fields and structural indices of euler deconvolution. *Geophysics* 72 (1), L1–L12.
- Stavrev, P., Reid, A., 2010. Euler deconvolution of gravity anomalies from thick contact/fault structures with extended negative structural index. *Geophysics* 75 (6), I51–I58.
- Stavrev, P. Y., 1997. Euler deconvolution using differential similarity transformations of gravity or magnetic anomalies. *Geophysical Prospecting* 45 (2), 207–246.
- Swain, C. J., 2000. Reduction-to-the-pole of regional magnetic data with variable field direction, and its stabilisation at low inclinations. *Exploration Geophysics* 31, 78–83.
- Teskey, D., Hood, P., Morley, L., Gibb, R., Sawatzky, P., Bower, M., Ready, E., 1993. The aeromagnetic survey program of the geological survey of canada: contribution to regional geological mapping and mineral exploration. *Canadian Journal of Earth Sciences* 30 (2), 243–260.
- Thompson, D., 1982. Eulph: A new technique for making computer-assisted depth estimates from magnetic data. *Geophysics* 47 (1), 31–37.
- Thurston, J., 2010. Euler deconvolution in the presence of sheets with finite widths. *Geophysics* 75 (3), L71–L78.
- Tikhonov, A. N., Arsenin, V. I., 1977. *Solutions of ill-posed problems*. Vol. 14. Winston, Washington, DC.
- Tontini, F. C., de Ronde, C., Scott, B., Soengkono, S., Stagpoole, V., Timm, C., Tivey, M., 2016. Interpretation of gravity and magnetic anomalies at lake rotomahana: Geological and hydrothermal implications. *Journal of Volcanology and Geothermal Research* 314, 84 – 94.
- Ugalde, H., Morris, W. A., 2010. Cluster analysis of euler deconvolution solutions: New filtering techniques and geologic strike determination. *Geophysics* 75 (3), L61–L70.
- Uieda, L., Oliveira Jr, V. C., Barbosa, V. C., 2013. Modeling the earth with *fatiando a terra*. In: *Proceedings of the 12th Python in Science Conference (SciPy 2013)*. pp. 96–103.
- Uieda, L., Oliveira Jr, V. C., Barbosa, V. C., 2014. Geophysical tutorial: Euler deconvolution of potential-field data. *The Leading Edge* 33 (4), 448–450.

- Vasquez, M., Sousa, C., Carvalho, J., 2008. Mapa geológico e de recursos minerais do estado do Pará, escala 1: 1.000. 000. Programa Geologia do Brasil, Belém, CPRM.
- Werner, S., 1953. Interpretation of magnetic anomalies at sheet-like bodies. *Norstedt*.
- Whitham, K., 1960. Measurement of the geomagnetic elements. *Methods and Techniques in Geophysics* 1, 104–167.
- Wijns, C., Perez, C., Kowalczyk, P., 2005. Theta map: Edge detection in magnetic data. *Geophysics* 70 (4), L39–L43.
- Zeyen, H., Pous, J., 1991. A new 3-d inversion algorithm for magnetic total field anomalies. *Geophysical Journal International* 104 (3), 583–591.
- Zhang, C., Mushayandebvu, M. F., Reid, A. B., Fairhead, J. D., Odegard, M. E., 2000. Euler deconvolution of gravity tensor gradient data. *Geophysics* 65 (2), 512–520.
- Zuo, B., Hu, X., Cai, Y., Liu, S., 2019. 3d magnetic amplitude inversion in the presence of self-demagnetization and remanent magnetization. *Geophysics* 84 (5), 1–84.

# Appendices

# Appendix A

## Theory of Euler deconvolution

### A.1 Euler's theorem for homogeneous functions

Euler deconvolution (Reid et al., 1990) is based on Euler's homogeneous function. By definition (Mas-Colell et al., 1995), if the function  $f(x_1, \dots, x_k)$  is homogeneous of degree  $N$  if  $\forall t > 0$ , we have:

$$f(tx_1, \dots, tx_k) = t^N f(x_1, \dots, x_k), N = \dots, -1, 0, 1, \dots \quad (\text{A.1})$$

If  $f(x_1, \dots, x_k)$  is homogeneous of degree  $N$  and has continuous first order partial derivatives (Sokolnikoff et al., 1966), then Euler's theorem for homogeneous functions (Irving and Mullineux, 1959) is:

$$\left(x_1 \frac{\partial}{\partial x_1} + x_2 \frac{\partial}{\partial x_2} + \dots + x_k \frac{\partial}{\partial x_k}\right) f(x_1, \dots, x_k) = N f(x_1, \dots, x_k). \quad (\text{A.2})$$

One way to achieve Euler's theorem for homogeneous functions (equation A.2) is deriving equation A.1. Assuming  $f(x_1, \dots, x_k) = f(x, y, z)$ , we will take the derivatives of equation A.1 with respect to  $t$ :

$$\frac{d}{dt} f(tx, ty, tz) = \frac{d}{dt} t^N f(x, y, z). \quad (\text{A.3})$$

Developing the left side of equation A.3:

$$\frac{d}{dt} f(tx, ty, tz) = \frac{\partial}{\partial x} f(tx, ty, tz) \frac{d}{dt}(tx) + \frac{\partial}{\partial y} f(tx, ty, tz) \frac{d}{dt}(ty) + \frac{\partial}{\partial z} f(tx, ty, tz) \frac{d}{dt}(tz). \quad (\text{A.4})$$

Going ahead with the derivation of A.4:

$$\frac{d}{dt} f(tx, ty, tz) = x \frac{\partial}{\partial x} f(tx, ty, tz) + y \frac{\partial}{\partial y} f(tx, ty, tz) + z \frac{\partial}{\partial z} f(tx, ty, tz). \quad (\text{A.5})$$

Now, taking the derivative of the right hand side of equation A.3:

$$\frac{d}{dt}t^N f(x, y, z) = Nt^{N-1}f(x, y, z). \quad (\text{A.6})$$

Replacing equations A.5 and A.6 in equation A.3:

$$x \frac{\partial}{\partial x} f(tx, ty, tz) + y \frac{\partial}{\partial y} f(tx, ty, tz) + z \frac{\partial}{\partial z} f(tx, ty, tz) = Nt^{N-1}f(x, y, z). \quad (\text{A.7})$$

For convenience, let's assume  $t = 1$  in equation A.7:

$$x \frac{\partial}{\partial x} f(x, y, z) + y \frac{\partial}{\partial y} f(x, y, z) + z \frac{\partial}{\partial z} f(x, y, z) = Nf(x, y, z). \quad (\text{A.8})$$

Equation A.8 is exactly equation A.2, which in turn is the Euler homogeneous equation.

## A.2 Euler's theorem applied to single-point sources

Henderson and Zietz (1948) used the equation that describes the field generated by magnetic single pole and the line of poles in order to perform interpretation. Smellie (1956), extended the work of Henderson and Zietz (1948) to a dipole and a line of dipoles. These authors have shown how single-point sources can represent simple geological bodies. Magnetic single-point sources generate fields that have the form:

$$f(x, y, z) = \frac{G}{\sqrt{(x - x_o)^2 + (y - y_o)^2 + (z - z_o)^2}^n}, \quad (\text{A.9})$$

where  $(x_o, y_o, z_o)$  are source coordinates,  $(x, y, z)$  are observation coordinates,  $G$  is a constant that depends on the source geometry and magnetic susceptibility contrast but does not depend on the position  $(x, y, z)$  and  $n$  is the constant related to the decay rate of the anomaly and depends on the geometry of each body.

Single-point sources generate fields that can be described by equation A.9 and respect Euler's homogeneous equation. This fact can be proven by using the Euler's homogeneous function theorem (equation A.1) and multiplying a constant  $t$  to the source and to the observation coordinates in equation A.9:

$$f(tx, ty, tz) = \frac{G}{\sqrt{(tx - tx_o)^2 + (ty - ty_o)^2 + (tz - tz_o)^2}^n}. \quad (\text{A.10})$$

Developing equation A.10:

$$f(tx, ty, tz) = \frac{G}{\sqrt{t^2 [(x - x_o)^2 + (y - y_o)^2 + (z - z_o)^2]}^n}, \quad (\text{A.11})$$

finally:

$$f(tx, ty, tz) = \frac{G}{t^n \sqrt{(x - x_o)^2 + (y - y_o)^2 + (z - z_o)^2}^n}. \quad (\text{A.12})$$

Replacing equation A.9 in the right hand side of equation A.12:

$$f(tx, ty, tz) = t^{-n} f(x, y, z). \quad (\text{A.13})$$

Equation A.13 shows that single-point sources generate a field that are homogeneous functions of degree  $-n$ .

Hood (1965) and Slack et al. (1967) showed that fields generated by magnetic point-sources are described by homogeneous functions. These authors were the first to use the Euler homogeneous equation for geological interpretation. By assuming the knowledge of  $\eta$ , Hood (1965) estimated the depth of bodies. On the other hand, Slack et al. (1967) estimated the depth and nature of the body simultaneously.

Assuming that the anomalous magnetic field is defined by:

$$H(x, y, z) = f(x, y, z), \quad (\text{A.14})$$

these authors used Euler homogeneous equation as:

$$x \frac{\partial}{\partial x} H(x, y, z) + y \frac{\partial}{\partial y} H(x, y, z) + z \frac{\partial}{\partial z} H(x, y, z) = -\eta H(x, y, z), \quad (\text{A.15})$$

where  $-\eta = N$  is the constant that describes the rate of decay of the field.

### A.3 Euler deconvolution

Thompson (1982) proposed a method called "Euldph" that is based on Euler's homogeneous function and applied it in profile data (2D case). Thompson (1982) called the decay rate constant (Hood, 1965; Slack et al., 1967) of structural index (SI -  $\eta$ ) and used the method to 2D profile data assuming an acquisition at ground level  $z = 0$ . This author proposed that a moving-data window scheme should be used, where at each moving-data window position the system of equations A.8 is solved, assuming a tentative SI. Moreover, Thompson (1982) noticed that the magnetic anomaly by itself was rarely recorded due to regional fields or interfering anomalies. Therefore, he proposed that the anomalous field is disturbed by a constant value in each window:

$$h(x, y, z) = H(x, y, z) + b, \quad (\text{A.16})$$

where  $h(x, y, z)$  is the total-field anomaly and  $b$  is the base level or background, which represents a constant value (in nT). Therefore the system of equations proposed and

solved by Thompson (1982) is:

$$x_o \frac{\partial h}{\partial x} + z_o \frac{\partial h}{\partial z} + \eta b = x \frac{\partial h}{\partial x} + \eta h. \quad (\text{A.17})$$

The system of equations A.17 can be solved for each moving-data window position using least squares. For each moving-data window position the parameters estimated are: the horizontal and vertical positions of the source and the base level, assuming a tentative SI. Thompson (1982), noticed that using tentative SI the correct depth estimates are close to each other, generating the tightest cluster of Euler solutions, if the correct SI is used. With this knowledge, he proposed a statistical criterion to determine the correct SI based on the grouping of the depth estimates.

Reid et al. (1990) expanded the work of Thompson (1982) to gridded data and called the method, popularly known, as Euler deconvolution. In addition, these authors deduced mathematically the SI for magnetic anomalies generated by dike and geological contact and gravimetric anomaly generated by a finite step. Euler deconvolution has the following formulation:

$$\hat{x}_o \frac{\partial h_i}{\partial x} + \hat{y}_o \frac{\partial h_i}{\partial y} + \hat{z}_o \frac{\partial h_i}{\partial z} + \eta \hat{b} = x_i \frac{\partial h_i}{\partial x} + y_i \frac{\partial h_i}{\partial y} + z_i \frac{\partial h_i}{\partial z} + \eta h_i, \quad (\text{A.18})$$

where  $h_i = h(x_i, y_i, z_i)$  is the  $i$ th observation of the total-field anomaly in coordinates  $(x_i, y_i, z_i)$ .  $\frac{\partial h_i}{\partial x}$ ,  $\frac{\partial h_i}{\partial y}$ , and  $\frac{\partial h_i}{\partial z}$  are the field derivatives with respect to the coordinates  $x$ ,  $y$  and  $z$  and  $\eta$  is the SI related to the nature or geometry of the source. The estimated parameters are  $\hat{x}_o, \hat{y}_o$  and  $\hat{z}_o$  related to the horizontal and vertical coordinates of the source, and  $\hat{b}$  is a base level (i.e., a background value). Therefore, solving this linear system of equations provides four parameters, assuming a tentative SI. Euler deconvolution works over the entire data set using a moving-data window scheme. At each moving-data window position, this system solves the system and estimates four parameters. The moving-data window is shifted along the whole data set, one grid position per time, thus overlapping the observations in the moving-data window.

Table A.1 shows the SIs used in Euler deconvolution and its relation with: magnetic sources, geometric and geological forms. Barbosa et al. (1999) showed that SI values close to zero can be used and they do not generate instability in the system of equations. However, they stressed that if SI is zero, the base level cannot be determined.

Figure A.1 shows some magnetic single-point sources and its geometric relationship (Table A.1) used in Euler deconvolution.

Euler deconvolution was initially proposed for processing aeromagnetic data (Reid et al., 1990), however it was extended to process ground data (Barbosa et al., 2000), gravimetric data (Marson and Klingele, 1993; Reid et al., 2003; Stavrev,

Table A.1: SIs used in Euler deconvolution and its relation to magnetic sources, geometric and geological forms. Source: Cella and Fedi (2012); Hinze et al. (2013); Reid et al. (1990); Reid and Thurston (2014); Stavrev (1997); Thompson (1982).

Structural index ( $\eta$ )	Magnetic source	Geometric source	Geologic source	Estimated depth
0	Sheet of poles / Vertical prism	Sheet in "L" / Infinity vertical prism	Infinity contact / fault	Top
1	Line of poles	Finite sheet / Horizontal prism	Vertical dike	Top
2	Horizontal line of dipoles	Horizontal cylinder	Horizontal pipe	Center
2	Pole / Vertical line of dipoles	Vertical cylinder	Plug / Vertical pipe	Top
3	Dipole	sphere	Magmatic chamber / UXO	Center

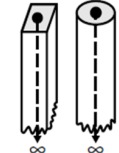
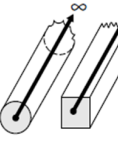
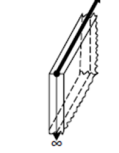
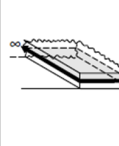
Single-point source	Dipole	Pole	Line of dipoles	Line of poles	Sheet of dipoles	Sheet of poles
Model						
Magnetic SI	3	2	2	1	1	0

Figure A.1: SIs of magnetic single-point sources. Modified from Hinze et al. (2013).

1997), gradiometric data (Zhang et al., 2000), satellite data (Ravat et al., 2002) and spontaneous potential data (Agarwal and Srivastava, 2009).

## A.4 Plot of the solutions

The plot of the Euler estimates plays a crucial role in the Euler deconvolution because the correct SI is determined from it. There are two ways to plot Euler estimates: i) the classic plot, where for each SI, the horizontal coordinates estimates obtained for each position of a moving-data window are plotted in the plan view of the study area and the depth estimates are represented by different color, and ii) the plateau plot, where for each SI, every Euler estimate is displayed against the central position of the moving-data window. Therefore, an explanation and differentiation between the classic plot of Euler deconvolution estimates (Reid et al., 1990) and the plateau plot (Barbosa et al., 1999; Melo and Barbosa, 2018; Melo et al., 2013) is necessary.

For a visual convenience, let us consider the  $k$ th and  $(k + 1)$ th moving-data

windows located over a geologic source. Figure A.2a shows a schematic pictorial representation of the classic plot of Euler estimates from a total-field anomaly with vertical magnetization assuming the correct SI, where the red rectangle outlines the horizontal projections of the source. In this plot, the  $k$ th and  $(k + 1)$ th estimates are shown such as displayed in Reid et al. (1990). In this classic plot, the estimates of the horizontal coordinates  $\hat{x}_o$  and  $\hat{y}_o$  are plotted on the  $x - y$  plane (north-east plane), and the depth estimate  $\hat{z}_o$  is plotted using color depth scale. Specifically, we are using colored circles to locate the estimates. Over the source and assuming the correct SI the horizontal and vertical estimates have values that are very close to the true source coordinates producing therefore the tightest cluster of source-position estimates. Usually the estimates  $\hat{b}$  are neglected, although they are calculated in equation 3.3. Here, the base-level estimates are plotted in the same way as depth estimates (Figure A.2a). Figure A.2b shows the base-level estimates  $\hat{b}$  for the correct SI in the same estimates of horizontal coordinates (shown Figure A.2a) and using a color scale in nanotesla.

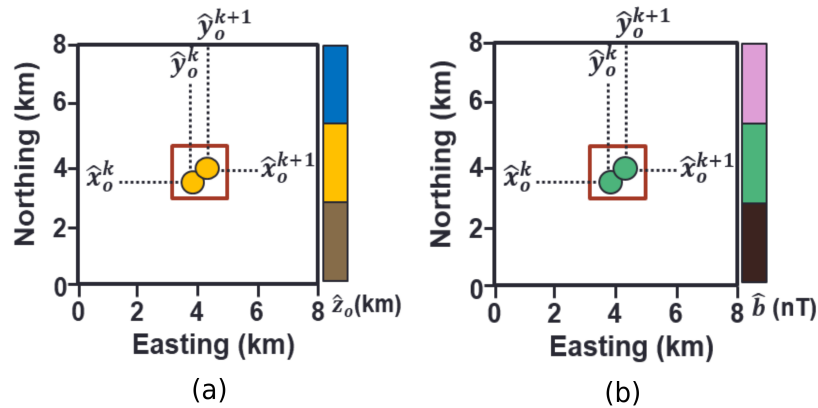


Figure A.2: Schematic pictorial representation of the classic plot of Euler deconvolution estimates for the correct SI over a source, outlined by a red rectangle. The  $k$ th and  $(k + 1)$ th horizontal coordinate estimates show  $\hat{x}_o^k$  and  $\hat{y}_o^k$  plotted at its plan  $(x, y)$  position, (a)  $\hat{z}_o$  and (b)  $\hat{b}$  are plotted using colored circles according to their color bars.

Figure A.3a-d shows a schematic pictorial representation of the plateau plot of the Euler deconvolution estimates assuming the correct SI, such as in Melo and Barbosa (2018); Silva and Barbosa (2003). These data windows are located over a geologic source outlined by the red rectangle in Figure A.3a-d. For each position of the moving-data window and assuming a tentative SI, the estimates  $\hat{x}_o^k$  (Figure A.3a),  $\hat{y}_o^k$  (Figure A.3b),  $\hat{z}_o^k$  (Figure A.3c) and  $\hat{b}^k$  (Figure A.3d) are plotted against the  $x_j$ - and  $y_j$ -coordinates of the center of the moving-data window producing four maps (Figure A.3a-d). Each map displays one of the four Euler estimates (each element of the parameter vector in equation A.18). Notice that the

plateau plot of the Euler estimates does not select or filter any estimate; this plot displays all estimates. For a graphical convenience, we highlight two estimates, with black dots, located at the central positions  $(x_j, y_j)$  and  $(x_{j+1}, y_{j+1})$  of the  $k$ th and  $(k + 1)$ th moving-data windows. If the correct SI is used, these estimates, over the source, form plateaus because the estimates from different moving-data windows are very close to each other. The minimum standard deviation of depth estimates, for the case of isolated or weakly interfering anomalies, defines the correct SI. For the case of mid or strongly interfering anomalies, the minimum standard deviation of base-level estimates defines the correct SI (Melo and Barbosa, 2018). The intersection of the plateaus on the horizontal coordinate estimates (shown in Figure A.3a and b) defines the region to compute the standard deviation of depth (or base level) estimates.

## A.5 Traditional definition of the correct SI

A practical impediment to the application of Euler deconvolution is the need to presume a tentative SI. Because the Euler deconvolution is grounded on homogeneous functions the SI can only be integer (Mas-Colell et al., 1995; Ravat, 1996; Reid et al., 2014; Reid and Thurston, 2014; Thurston, 2010); otherwise, the index changes under the variation of the source-observation vector (Ravat, 1996; Reid and Thurston, 2014). Assuming integer SIs, Thompson (1982) noticed the relationship between the correct SI and depth estimates. This author noticed that the correct SI produces the lowest scattering of solutions and thus proposed a method to determine the correct SI. Therefore, Thompson (1982) proposed the acceptance of solutions satisfying the inequality:

$$\frac{\hat{z}_o}{\eta\sigma_{z_o}} > 20, \quad (\text{A.19})$$

where  $\hat{z}_o$  is the estimated depth,  $\eta$  is the SI and  $\sigma_{z_o}$  is the standard deviation of  $z_o$  estimates. Silva et al. (2001) showed that the criterion for determining the SI as the tentative value that produces the minimum scattering of the solutions, which includes the depth estimates, is theoretically solid, but may fail in practice because of the noise in the data.

Reid et al. (1990) followed the approach of the clustering of solutions and proposed their widely accepted and used methodology to define the correct SI with a variation of the methodology of Thompson (1982). Reid et al. (1990) proposed the acceptance of solutions satisfying the inequality:

$$\frac{\sigma_{z_o}}{\hat{z}_o} < 0.15. \quad (\text{A.20})$$

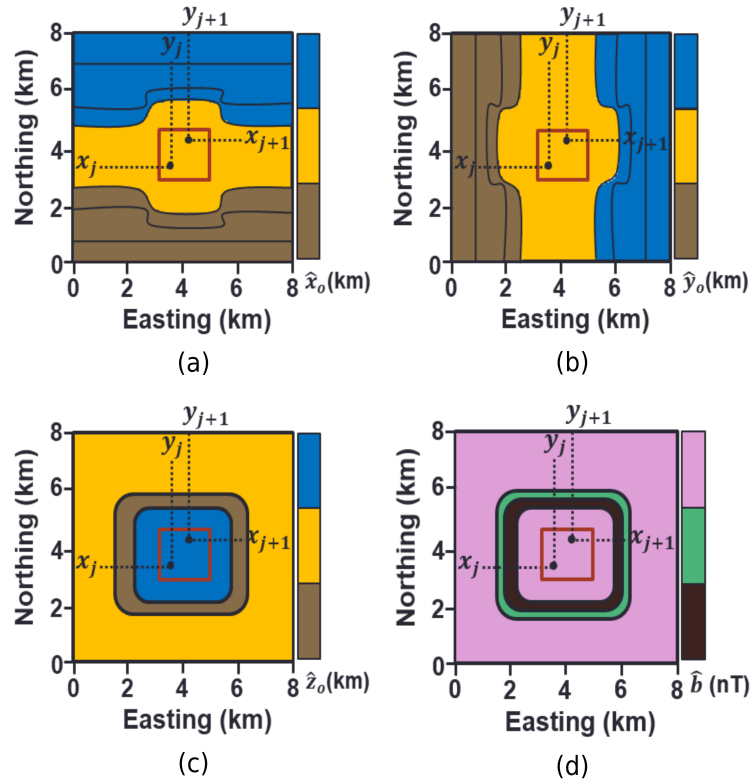


Figure A.3: Schematic pictorial representation of the plateau plot of Euler deconvolution estimates for the correct SI over a source, outlined by a red rectangle. The estimates (a)  $\hat{x}_o^k$ , (b)  $\hat{y}_o^k$ , (c)  $\hat{z}_o^k$  and (d)  $\hat{b}^k$  are plotted against the central position of the moving-data window. We highlight two estimates, with black dots, located at the central positions  $(x_j, y_j)$  and  $(x_{j+1}, y_{j+1})$  of two moving-data windows.